

Mari Hognestad

The Effect of Tortuosity and Porosity Graded Graphite Electrodes in Lithium-Ion-Batteries During Fast Charging

Master's thesis in Chemical Engineering and Biotechnology

Supervisor: Nils Peter Wagner

Co-supervisor: Ann Mari Svensson

June 2022

Mari Hognestad

The Effect of Tortuosity and Porosity Graded Graphite Electrodes in Lithium- Ion-Batteries During Fast Charging

Master's thesis in Chemical Engineering and Biotechnology
Supervisor: Nils Peter Wagner
Co-supervisor: Ann Mari Svensson
June 2022

Norwegian University of Science and Technology
Faculty of Natural Sciences
Department of Materials Science and Engineering

Preface

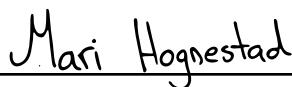
This master project was carried out as a part of the course "TMT4900 Materials Chemistry and Energy Technology, Master's Thesis" at NTNU Trondheim, and is in collaboration with Vianode. The project covers the effect of tortuosity and porosity graded graphite electrodes during fast charging.

The graphite powders used for the experiments was provided by Vianode while the additional materials were provided by the Department of Material Science and Engineering at NTNU Trondheim and SINTEF. The experiments have been performed at the Department of Material Science and Engineering at NTNU Trondheim.

During this project I have received great guidance and support. Specially, I want to thank my main supervisor Nils Peter Wagner, for excellent guidance during the experiments, and valuable feedback and support throughout the project. Additionally, my gratitude to my co-supervisor Ann Mari Svensson for excellent guidance and valuable discussions. I also want to thank Vianode represented by Navaneethan Muthuswamy for good support.

During this period, I have also received training of different instruments. I want to thank Eva Rise for training on the Horiba Partica LA-960 instrument. Additionally, I want to thank Elin Harboe Albertsen for training of measuring the BET surface area. Also, my gratitude to SINTEF for allowing me to use their instruments. Specially I would like to thank Kaushik Jayasayee for training on the Autolab equipment, and Francis Kinyanjui and Agnes Digranes for valuable discussions and guides in the lab. Also, I want to thank SINTEF Industry by Mathias Schrade how generated cross sections of the electrodes by using an argon ion beam mil. Lastly, my gratitude to FACET, the battery group and classmates for good discussions and enthusiasm throughout the semester.

Trondheim, June 10, 2022



Mari Hognestad

Abstract

In this project the effect of tortuosity and porosity graded graphite electrodes were studied during fast charging. Two graphite powders, named S48 and S93, with different morphology were used to make electrodes, in which the tortuosity of these electrodes was measured with electrochemical impedance spectroscopy. Symmetrical cells having graphite as both the working- and counter- electrode were used for the measurements. To verify the choice of using the simplified transmission line model to evaluate the impedance data, the tortuosity was measured with two different electrolytes. These consisted of 0.01M and 0.1M Bu_4NPF_6 in 1:1 wt% EC and DMC. The result gave tortuosity of 3.01 ± 0.07 and 3.79 ± 0.36 for electrodes made by the S93-powder for the 0.01M and 0.1M electrolyte respectively. A higher tortuosity was measured for the S48-powder with 5.20 ± 0.10 and 5.61 ± 0.35 for the 0.01M and 0.1M electrolytes respectively.

Further, the fast charge ability of electrodes made by the two powders were evaluated with charging rates from $C/2$ to $5C$. For these experiments an anode controlled 3-electrode cell was used having graphite, oversized lithium iron phosphate and lithium metal as the counter-, working- and reference- electrode respectively. The cell with graphite electrode of the lowest tortuosity (S93-cell) gave the best rate performance. This cell had the highest state of charge at $C/2$ equal 93.7%, compared to 90.4% for the cell having graphite electrode with the highest tortuosity(S48-cell). Furthermore, the capacity fade was lower for the S93-cell. Additionally, from electrochemical impedance results, a lower total resistance was measured for the S93-cell. These observations were likely to be caused by a reduced intercalation rate for the high tortuosity graphite electrodes, as these electrodes have longer and more complex pathways for lithium ions.

Furthermore, the effect of porosity graded graphite electrodes was studied by fabricating double layer electrodes having a bottom layer with geometrical density equal 1.45 g/cm^3 and a top layer with geometrical density of 1.25 g/cm^3 . This electrode was compared to a single layer electrode with uniform geometrical density corresponding to the theoretical average geometrical density of the double layer electrode equal 1.35 g/cm^3 . The double-and single-layer electrodes were made by the S93-powder. The manufacturing of the double layer electrodes was challenging and resulted in an uneven loading distribution.

The fast charge ability of the double- and single- layer electrodes were studied by using the same set-up and test program as described for the S48-and S93-cell. The result showed a higher stat of charge for the single layer electrode compared to the double layer electrode with corresponding values of 89.4% and 82.4% at $C/2$. Furthermore, the capacity fade was larger for the double layer electrode equal 46.44 % by increasing the charging rate from $C/2$ to $1C$. For the same increase in charging rate, a capacity fade of 21.7% was observed for the single layer

electrode. The reduced performance of the double layer electrode was assumed to be caused by an uneven loading distribution, and the dense bottom layer which inhibits the electrolyte's ability to penetrate into the electrode. Consequently, the intercalation rate of lithium ions is reduced in this region. Additionally, the electrical contact between the bottom layer and the current collector was not optimal which also reduced the performance of this cell. Lastly, from the electrochemical impedance results, the total resistance was highest for the cell with the double layer electrode.

Sammendrag

I dette prosjektet ble effekten av tortuositet og elektroder med porøsitetens gradient studert under hurtiglading. To grafitt pulvere med ulik morfologi ble brukt til å lage elektroder. Disse pulverne er kalt S48 og S93. Tortuositeten til disse elektrodene ble målt med elektrokjemisk impedans målinger ved bruk av symmetriske celler som hadde grafitt som både arbeid- og mot- elektrode. For å verifisere valget om å bruke den forenklete transmittans modellen, ble tortuositeten målt for to ulike elektrolytter. Disse elektrolyttene bestod av 0.01M and 0.1M Bu_4NPF_6 i 1:1 vt% forhold av EC og DMC. Resultatene gav tortuositet på 3.01 ± 0.07 og 3.79 ± 0.36 for elektroder laget av S93-pulveret med henholdsvis 0.01M og 0.1M elektrolytt. Elektrodene laget av S48-pulveret hadde en høyere tortuositet lik 5.20 ± 0.10 og 5.61 ± 0.35 for elektrolytter med konsentrasjon på henholdsvis 0.01M og 0.1M.

Videre ble hurtigladnings evnen til de to ulike elektrodene testet ved å lade fra C/2 til 5C. For disse målingene ble en anode kontrollert 3-elektrode celle bruk. Den bestod av grafitt som mot-elektrode, en overdimensjonert litium jernfosfat katode som arbeids-elektrode og litium metal som referanse- elektrode. Resultatene viste en høy ladningstilstand lik 93.7% ved C/2 for cellen bestående av grafitt med lavest tortuositet. En lavere ladningstilstand lik 90.4% var imidlertid observert for cellen bestående av grafitt elektrode med høyest tortuositet. I tillegg, ble en lavere motstand målt for S93- cellen ved bruk av elektrokjemiske impedans målinger av de to cellene. Disse observasjonene skyldes trolig en lengre og mer kompleks transport vei for litium ioner gjennom elektroden med høy tortuositet.

Videre ble effekten av elektroder med porøsitetens gradient undersøkt. Disse elektrodene bestod av et nedre lag med geometrisk tetthet på 1.45 g/cm^3 , og et topp lag med geometrisk tetthet lik 1.25 g/cm^3 . Denne elektroden ble sammenlignet med en et-lags elektrode, med geometrisk tetthet som korresponderte til den gjennomsnittlige tettheten til to-lags elektroden lik 1.35 g/cm^3 . Både to- og et-lags elektrodene ble laget av S93-pulveret. Fabrikkeringen av tolags elektrodene var utfordrerne og gav en ujevn fordeling av det aktive materialet.

Hurtigladnings egenskapene for de to elektrodene ble sammenlignet med tilsvarende prosedyre som beskrevet for S48- og S93-cellen. Resultatene viste at et-lags elektroden oppnådde en høyere ladningstilstand med 89.4% ved ladning på C/2, sammenlignet med 82.4% for to-lags elektroden. I tillegg ble et betydelig større kapasitets tap observert

for to-lags elektroden, da kapasiteten falt med 46.44% ved å øke ladehastigheten fra C/2 til 1C. Dette var betydelig høyere sammenlignet med et-lags elektroden som hadde et kapasitets fall på 21.7% for samme økning i landingshastighet. Hovedteorien for disse observasjonene var relatert til en ujevn fordeling av det aktive materialet på tolags elektroden. Videre ble transporten av litium ioner i det nederste laget på to-lags elektroden vurdert som dårlig. Dette skyldes at elektrolytten trolig ikke evnet å diffunder langt inn i dette laget. Dårlig kontakt mellom det nederste laget og kopper folien var også vurdert som en kilde til de dårligere egenskapene for tolags elektroden. Til slutt ble motstanden i de to cellene målt med elektrokjemisk impedans målinger. Fra disse resultatene ble en høyere total motstand observert for cellen med to-lags elektrode.

Contents

1 Introduction	1
1.1 Background and motivation	1
1.2 Aim of the project	3
2 Theory	5
2.1 Working principle of a lithium ion battery	5
2.2 Definitions	7
2.3 Electrolyte	9
2.4 Solid electrolyte interphase	10
2.5 Electrode materials	12
2.5.1 Cathodes	13
2.5.2 Anodes	14
2.6 Graphite as anode material	15
2.6.1 Intercalation of lithium ions	17
2.7 Degradation of LIB	19
2.7.1 Lithium plating	19
2.7.2 Factors influencing lithium plating	20
2.7.3 Investigation of lithium plating	22
2.8 The effect of electrode morphology	23
2.8.1 The effect of porosity	23
2.8.2 The effect of tortuosity	25
2.8.3 Effect of particle size and shape	26
2.9 Electrochemical characterization	27
2.9.1 Galvanostatic cycling with potential limitations	27
2.9.2 Electrochemical impedance spectroscopy	28
2.9.3 Ionic conductivity measurement with electrochemical impedance spectroscopy	31
2.10 Physicochemical characterisation techniques	31
2.10.1 Scanning electron microscopy	31
2.10.2 BET surface area measurement by BET- theory	32
2.10.3 Laser diffraction	32
3 Experimental	33
3.1 Materials	33

3.2 Powder characterization	33
3.2.1 Morphology	34
3.2.2 Particle size distribution	34
3.2.3 BET-surface area	34
3.3 Slurry production and tape casting	34
3.4 Cell assembly	37
3.4.1 Coin cell	37
3.4.2 3-electrode cell	38
3.5 Determination of the specific capacity	39
3.6 Slurry optimization	39
3.7 Formation of 3-electrode cells	40
3.8 Tortuosity measurements	40
3.8.1 Electrolytes	41
3.8.2 Symmetric cell assembly	42
3.8.3 Test program: ionic resistance	42
3.9 Fast charge ability of S48- and S93-electrodes	43
3.9.1 Test program: charge acceptance test	43
3.9.2 Postmortem characterization of cycled electrodes	44
3.10 Porosity graded electrodes	44
3.10.1 Manufacturing	44
3.10.2 Fast charge ability of porosity graded electrodes	46
3.10.3 Cross section characterization	46
4 Results	47
4.1 Powder characterization	47
4.2 Slurry optimization and manufacturing of anode laminates	49
4.2.1 Determination of the specific capacity	49
4.2.2 Processing parameters	49
4.2.3 Manufacturing of porosity graded electrodes	51
4.3 Tortuosity measurement: comparing S48- and S93- electrodes	55
4.3.1 Ionic conductivity measurements	55
4.3.2 Symmetrical cell impedance	56
4.4 Evaluation of the fast charge ability of S48- and S93-electrodes	60
4.4.1 Postmortem characterisation of cycled electrodes	65
4.5 Porosity graded electrodes	67

4.5.1	Cross section characterization of the single- and double- layer electrode	67
4.5.2	Evaluation of fast charge ability of single- and double-layer electrode	69
5	Discussion	75
5.1	Comparison of the S48- and S93- powder	75
5.1.1	Tortuosity measurement	75
5.1.2	Fast charge ability	77
5.2	Porosity graded electrodes	81
5.2.1	Manufacturing	81
5.2.2	Fast charge ability of porosity graded electrodes	83
6	Conclusion	87
7	Further work	89
A	Acronyms	103
B	Calculations for experimental procedure	105
B.1	Slurry production	105
B.1.1	CMC-solution	105
B.1.2	Calculations of slurry components	105
B.2	Loading and C-rates	106
B.3	Calendering	107
B.4	Porosity	107
B.5	Electrolyte	108
C	Cycling programs	111
C.1	Determination of the specific capacity	111
C.2	Formation of 3-electrode cells	112
C.3	Charge acceptance test for 3-electrode cell	114
D	Results	117
D.1	Obtainable capacity from first formation cycle	117
D.2	Ionic conductivity measurements	118
D.2.1	Cell constant	118
D.2.2	Conductivity of electrolytes	119

D.2.3 Ionic resistance	119
D.3 Electrochemical impedance data for S48- and S93- cells	120
D.4 Electrochemical impedance data for the double- and single- layer electrode cells	121

Table of abbreviations

Table 0.1: Abbreviations used in the report.

Abbreviations	Explanation
AFM	Atomic force Microscopy
BEV	Battery electrical vehicles
BET	Brunauer Emmett Teller
CEI	Cathode electrolyte interphase
DVA	Differential Voltage Analysis
DMC	Dimethyl carbonate
EIS	Electrochemical impedance spectroscopy
EC	Ethylene carbonate
EMC	Ethyl methyl carbonate
GCPL	Galvanostatic cycling with potential limitations
GEIS	Galvanostatic electrochemical impedance spectroscopy
HOMO	Highest occupied molecular orbital
LCO	Lithium cobalt oxide(LiCO_2)
LIB	Lithium ion battery
LFP	Lithium iron phosphate
LUMO	Lowest unoccupied molecular orbital
NMC	Lithium manganese nickel cobalt oxide $\text{Li}(\text{Ni}_x\text{Mn}_y\text{Co}_z)\text{O}_2$
OCV	Open circuit voltage
PEIS	Potentiostatic electrochemical impedance spectroscopy
SEM	Scanning electron microscope
SEI	Solid electrolyte interphase
SOC	State of charge
TEM	Transmission Electron Microscope
TLM	Transmission line model

List of Tables

0.1 Abbreviations	xi
2.1 Impedance for circuit elements	29
3.1 Materials used in the project	33
3.2 Aimed slurry composition	35
3.3 Mixing program for CMC-solution	35
3.4 Mixing program for slurry production	36
3.5 Experimental for slurry optimization	39
4.1 BET surface area	47
4.2 Slurry optimization of the S48-powder	50
4.3 Slurry optimization of the S93-powder	50
4.4 Loading of double layer electrodes made with gap-size of 50 μm and 100 μm .	53
4.5 Conductivity of electrolytes used in tortuosity measurements	56
4.6 Physical properties of electrodes in the symmetrical cells	57
4.7 Tortuosity values of S48- and S93-electrodes	59
4.8 Physical properties of S48- and S93- electrodes for charge acceptance test	60
4.9 Physical properties of double- and single-layer electrodes	69
A.1 Acronyms	103
B.1 Theoretical density of slurry components	108
B.2 Composition of the electrolytes used for tortuosity measurements	108
C.1 Cycling program: determination of the specific capacity	112
C.2 Cycling program: formation of 3-electrode cells.	113
C.3 Cycling program: charge acceptance test of 3-electrode cells.	115
D.1 Fitted EIS parameters for 0.1 KCl-solution	118
D.2 Fitted EIS parameters for the conductivity measurements	119
D.3 Fitted EIS parameters for ionic resistance measurements	119
D.4 Fitted EIS parameters for S48-and S93-cells	120
D.5 Fitted EIS parameters for the double layered electrode cell	121
D.6 Fitted EIS parameters for the single layered electrode cell	122

List of Figures

2.1 Working principle of lithium ion battery	6
2.2 Stability window of electrolyte	10
2.3 SEI-layer on graphite electrode	12
2.4 Electrode materials	13
2.5 Graphite structure	16
2.6 Characteristic voltage plateaus for lithium intercalation	17
2.7 Intercalation pathways of lithium ions in graphite	18
2.8 Diffusion of lithium ions in porous electrode	21
2.9 Effect of thickness on graphite electrodes	24
2.10 Circuit: Simplified transition line model	30
3.1 Experimental procedure of tape-casting	36
3.2 Coin cell assembly	37
3.3 PAT-cell components	39
3.4 Circuit: Electrolyte conductivity	41
3.5 Circuit: Tortuosity measurement	42
3.6 Circuit: impedance of 3-electrode cells	44
3.7 Experimental setup of a double layered electrode	45
4.1 PSD-analysis	47
4.2 SEM micrographs of the S48- and S93- powder	48
4.3 Specific capacity of the S48- and S93- powder	49
4.4 Bottom layer of a double layer anode laminate after calendering	51
4.5 Bottom layer of a double layer anode laminate after pressing	52
4.6 Double layered anode laminate	53
4.7 Nyquist plot from conductivity measurements	56
4.9 Nyquist plot from the symmetrical cells	58
4.11 Potential as a function of time for two cycles in charge acceptance test	61
4.12 Charge acceptance test comparing the S48- and S93-cell	62
4.13 Potential curves for the S48- and S93-cell	63
4.14 Nyquist plot for the S48- and S93- cell	64
4.15 SEM micrographs of cycled and uncycled S48- and S93- electrodes	66
4.17 Cross section SEM micrographs of single- and double- layer electrodes	68
4.18 Charge acceptance test comparing double- and single- layer electrode cell	70
4.19 Potential curves for double- and single- layer electrode cell	71

4.20 Nyquist plot for double- layered electrode cell	73
4.21 Nyquist plot for single- layered electrode cell	73
C.1 Potential vs. time capacity test of coin cells	111
C.2 Potential vs. time 3-electrode cell formation	112
C.3 Potential vs. time rate-test	114
D.1 Obtainable capacity during formation at C/30	117
D.3 Nyquist plot of KCl-solution	118

1 Introduction

1.1 Background and motivation

During the next 30 years, the global energy consumption is predicted to increase by 50 %^[1]. Simultaneously aims the European commission to have a climate neutral Europe within 2050^[2]. With today's energy production, these points are contradictory, and outlines the importance of comprehensive changes within the energy sector.

As the transport sector accounted for 24 % of the global emissions in 2020^[3], major improvements have already been set into action to make it more sustainable. One of these improvements is the use of battery electrical vehicles (BEV) in which lithium ion batteries (LIBs) have been the dominating technology. However, to obtain a full transition from internal combustion engines to BEV, the new technology must compete with the combustion engine both regarding cost, energy density, charging time and driving range^[4].

Unfortunately, today's BEVs often have shorter driving range, are more expensive, and the charging time is not competitive with the combustion engines'. Most of these challenges are related to the battery performance.

LIBs are being charge when lithium ions are transferred from the cathode to the anode. In today's LIBs, graphite is the most used anode material due to its high specific capacity, high abundance and high conductivity. However, this material constitutes a problem during fast charging^[5]. Fast charging is one of the biggest challenges for LIBs, due to lithium plating that can occur at the anode surface^[6]^[7]. This phenomenon occurs when lithium metal is deposited at the anode surface instead of being intercalated into the host structure. Consequently, the capacity decreases, and the performance of the battery is reduced. Lithium plating often occurs when the charging rate exceeds the intercalation rate. Therefore, to decrease the probability of plating, one possibility is to increase the intercalation rate^[8]. One of the factors that have been studied for this purpose is the morphology of graphite electrodes.

The tortuosity of an electrode is an important parameter that affects the transport of charge carriers into the graphite electrode. High tortuosity represents long and complex pathways which increases the diffusion length, hence the intercalation rate of the charge carriers decreases. Therefore, an electrode having a low tortuosity is expected to achieve a high diffusion rate of lithium ions^[9]. Another important parameter for lithium transport is the porosity. A porous electrode has easily accessible pathways, which enables fast diffusion of lithium ions. To enable fast charging without increasing the degradation

of the battery, a porous electrode is therefore preferred^[10]. However, to maximize the energy density of the battery, the industry desire to have electrodes with high loading and low porosity. This can be achieved by having dense and thick electrodes. Therefore, to increase the rate performance of LIB without affecting the energy density, a compromise between high loading and porous electrode is needed. To obtain this, electrodes having a porosity gradient have been suggested. This technology provides a high density of active material close to the current collector, while it is more porous close to the electrode surface. This enables open pathways for lithium ions while at the same time achieving higher loading^[11]. However, this is so far limited to few and mainly computational studies and further research is therefore needed^{[12] [13]}.

With this in mind, the morphology of the graphite anode constitutes an important parameter when optimizing the battery performance. Many research groups and companies are working within this field, in which Vianode is one of them. This is a spin-of company of Elkem, which specializes on graphite powders for lithium ion batteries. Their focus is to develop synthetic graphite products suitable for fast charging.^[14]

1.2 Aim of the project

This project aims to investigate the effect of tortuosity and porosity graded graphite anodes in LIBs during fast charging. With this, the goal is to contribute to Vianode's research to develop graphite more suitable for fast charging.

The effect of tortuosity is investigated by comparing two graphite powders with different morphology, both in which are provided by Vianode. The tortuosity of the electrodes made by the two powders will be measured by electrochemical impedance spectroscopy. For this, symmetrical two-electrode cells having graphite as both working- and counter-electrode will be used. Furthermore, the fast charge ability of the two powders is investigated in an anode controlled 3-electrode cell. The cell has graphite as the anode material, an oversized lithium iron phosphate (LFP) as the cathode, and lithium metal as the reference electrode. Lastly, the effect of porosity graded electrodes is investigated by comparing a double layered electrode with a single layered electrode. The double layered electrode has a dense bottom layer and less dense top layer, while the single layered electrode has a uniform density equal the average density of the double layered electrode.

This project aims to use conditions close to the industry, by using quite high area capacities equal to $2\text{mAh}/\text{cm}^2$. The goal is to obtain results that matches the observations for commercialized batteries. This is viewed as an important factor when studying the morphology of graphite, as the effect of both porosity and tortuosity may not be as clear for thinner electrodes with lower loading. This can be explained by the fact that the lithium diffusion length is smaller for thinner electrodes. In this case, a large degree of the electrode is utilized, and the effect of porosity and tortuosity may not be as visible compared to thicker electrodes with higher loading.

2 Theory

2.1 Working principle of a lithium ion battery

There exist two types of batteries, primary- and secondary- batteries. In contrast to primary batteries, secondary batteries can transform electrical energy into chemical energy and vice versa, allowing the battery to be charged and discharged^[7]. These properties make secondary batteries an important part of today's-, and the future's- energy storage. The most used battery technology is lithium ion battery (LIB), which was first introduced by Sony in 1991^[7]. The wide usage of this type of battery is related to its long cycle life, the absence of a memory effect and high gravimetric- and volumetric- capacity^{[15] [7]}.

A secondary lithium ion battery consist of a positive- and a negative- electrode which is referred to as the cathode and anode respectively. The electrodes are wetted with an electrolyte and separated by a separator to avoid short circuit. The cathode constitutes as the lithium source, while the anode functions as the host structure that can store lithium ions^[7]. Today, transition metal oxides such as lithium cobalt oxide, LCO, and lithium manganese nickel cobalt oxide, NMC, are the most used cathode materials with a market share of 45 %^[16] and 30 %^[17] in 2017 respectively. For the anode material, graphite is the most popular material with a 96 % market share in 2016^{[18] [15]}.

During charging, lithium ions are liberated from the positive electrode in an oxidation reaction. This is accompanied by a migration of lithium ions through the separator towards the negative electrode where they are intercalated by a reduction reaction. These are topotactic reactions, meaning that the core structure does not undergo major changes. Simultaneously are electrons extracted from the positive electrode and transported towards the negative electrode in an outer circuit. The opposite reaction occurs when the battery is discharged. Figure [2.1](#) shows the working principle of a LIB having graphite as anode material, and LCO as cathode material^[7].

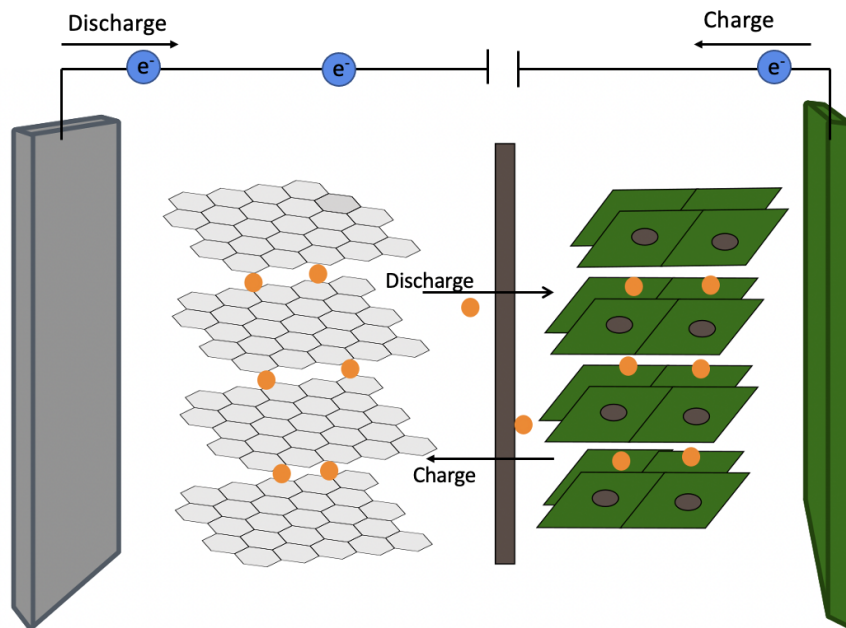


Figure 2.1: Working principle of lithium ion battery. The illustration has graphite as anode material and LCO as cathode material [19].

2.2 Definitions

- **Capacity:** The capacity of a battery is defined as the amount of charge it can deliver and is usually given in ampere-hour [Ah]. Every electrode material has a theoretical capacity which based on Faraday's law is given by Equation 2.1^[20]. This value is often presented in mAh/g, in which ampere corresponds to C/s.

$$Q_{theoretical} = \frac{F \cdot n}{M \cdot 3600} \quad (2.1)$$

Here, F is Faraday's constant and equals 96485 C/mol^[21], n is moles of electrons, M is the molar mass of the material and 3600 is the number for seconds in one hour. The capacity of a battery is affected by both the anode and cathode material^[7].

- **C-rate:** C-rate is the rate at which the battery is charged or discharged. The higher C-rate the faster is the charging/discharging. 1C referees to the current at which the battery is fully discharged in one hour^[7].
- **Cycle life:** Based on the paper "The Li-Ion Rechargeable Battery: A Perspective" written by John B. Goodenough and Kyu-Sung Park^[22], the cycle life is given by the number of cycles a battery can perform before the capacity has faded to 80 % of its initial capacity.
- **Electrochemical potential:** For a specie i , the electrochemical potential is given by Equation 2.2^[20]

$$\tilde{\mu}_i = \mu^o + RT \ln(a_i) + z_i F \phi_i \quad (2.2)$$

where T is the temperature, z_i is the valency of the specie i , R is the gas constant equal 8.314^[21], a_i is the activity of specie i , ϕ_i is the potential of specie i , and μ^o is the standard chemical potential.

- **Energy:** The amount of charge that is generated, or consumed over a given time is given as the energy of a battery^[7]. In a fully charged battery, the energy can be expressed as a function of time (t) or the charge (q) as shown in Equation 2.3^[23]

$$\text{energy} = \int_0^{\Delta t} I \cdot V(t) dt = \int_0^Q V(q) dq. \quad (2.3)$$

were I is the current, $V(t)$ is the voltage as a function of time, Δt is measured time, $V(q)$ is the voltage as a function of q , and Q is the total charge per unit weight^[22].

The energy is normally given in watt-hour[Wh].

Energy density is an important term used to describe the quality of a battery. It describes the amount of energy a fully charged battery can store per unit volume or mass^[23].

- **Faradaic charge transfer reaction:** Faradaic reactions follow Faradays law which means that the amount of charge passing through a boundary is proportional to the amount of chemical reactions that occurs in the system^[20].
- **Non-faradaic charge transfer reaction:** Non-faradaic reactions do not follow Faraday's law. This means that current can flow through a cell without any chemical reactions^[20].
- **Loading:** Loading describes the amount of active material per area and is usually given in [mg/cm²]^[20].
- **Open circuit voltage:** The open circuit voltage(OCV) is the potential when no current is flowing and is given in volt [V]. It can be expressed as the potential difference between the working-(W_{WE}) and the counter- (W_{CE}) electrode, which usually refers to the positive- and negative- electrode respectively. OCV can also be calculated based on the Gibbs free energy, ΔG , number of electrons, n , and Faraday's constant equal 96485 C/mol^[21]. Gibbs energy can further be expressed as a function of the standard Gibbs free energy ΔG° , and the activities of the reactants A and B , and the products C and D . Here a , b , c and d are the stoichiometry of each component^[20].

$$\Delta E = V_{WE} - W_{CE} = -\frac{\Delta G}{nF} = -\frac{\Delta G^\circ}{nF} + \frac{RT}{nF} \cdot \ln\left(\frac{a_C^c \cdot a_D^d}{a_A^a \cdot a_B^b}\right) \quad (2.4)$$

- **Power:** Power is given by the rate at which the energy is transported^[7] and is often given in watt [W]. The power of a battery is therefore limited by the kinetics of the charge transfer^[23].

The power density of a battery is given by amount of power being transferred per unit volume or mass^[23].

- **State of charge:** The state of charge (SOC) is given by the ratio of the accessible

capacity to the maximum capacity of the battery (often referred to as the specific capacity), which is given in Equation [2.5](#)

$$SOC = \frac{Q_{\text{access}}}{Q_{\text{specific}}} \cdot 100\% \quad (2.5)$$

At 100 % SOC, the cell has reached its maximum capacity and is therefore fully charged [24](#).

2.3 Electrolyte

The choice of electrolyte constitutes an important part of optimizing the battery performance. There are many factors to be considered when optimising an electrolyte. Firstly, to ensure fast transport of lithium ions through the electrolyte, high ionic conductivity is important [7](#). Moreover, good wettability is needed for optimal transport of the electrolyte into the porous electrode. This increases the fraction of surface area being utilized which contributes to higher energy- and power- density [25](#) [26](#). In addition, it is important that the electrolyte does not promote corrosion of any battery parts. This has especially been seen as a problem for the current collector [27](#). Factors such as abundance, non-flammability and environmentally friendliness are also preferred. Unfortunately, it is hard to produce an electrolyte with all these qualities. Therefore, to achieve the best possible electrolyte, combinations of different solvents and additives must be used [7](#).

In general, the electrolyte consists of solvents, salts, and possible additives. In LIBs the salt must contain lithium, and LiPF_6 is the most used salt in today's electrolytes [28](#). To meet the demands mentioned above, multiple solvents are needed to make as optimal performance as possible. Regarding the solvents, a low viscosity is preferred as this enables the electrolyte to penetrate deeper into the porous electrode, hence the transport of lithium ions is improved. On the other hand, to dissolve the salt, the solvent also needs to have high dielectric permittivity. Ethylene carbonate (EC) is one type of solvent that is used in most electrolytes. This solvent has a high viscosity and melting temperature and hence must be combined with other carbonates such as dimethyl carbonate (DMC), ethylmethyl carbonate (EMC) and diethyl carbonate (DEC) to improve the properties [29](#) [28](#).

One of the most important properties of an electrolyte is to have a large electrochemical stability window. This means that the electrolyte must be stable within the operating

potential range. The window is given by the band gap, E_g , of the electrolyte. For liquid electrolytes, this is defined as the potential range between the highest occupied molecular orbital (HOMO) and the lowest unoccupied molecular orbital (LUMO). The electrolyte is said to be stable if the electrode potential of the cathode, μ_c , is higher than the HOMO, and when the electrode potential of the anode, μ_a , is lower than the LUMO. If the electrode potentials are outside this stability window, degradation of the electrolyte can occur at the electrode- electrolyte interphase forming solid electrolyte interphase (SEI) and cathode electrolyte interphase (CEI) on the anode and cathode respectively. Figure 2.2 shows the two different scenarios, in which the dotted electrode potentials symbolize a stable electrolyte, while the filled boxes mark the situation in which the electrolyte is unstable^[22]. The use of HOMO and LUMO to express the electrochemical stability window of an electrolyte was however not supported by the article "Electrochemical potential window of battery electrolytes: the HOMO–LUMO misconception" written by Pekka Peljo and Hubert H. Girault^[30]. They showed that an electrolyte could be oxidized or reduced inside of the stability window defined by LUMO and HOMO, because other molecules such as reaction products affects the redox potential of the electrolyte. Instead of using HOMO and LUMO to identify the electrochemical stability window, they suggested that an electrolyte reduction- and oxidation- potential should be established^[30].

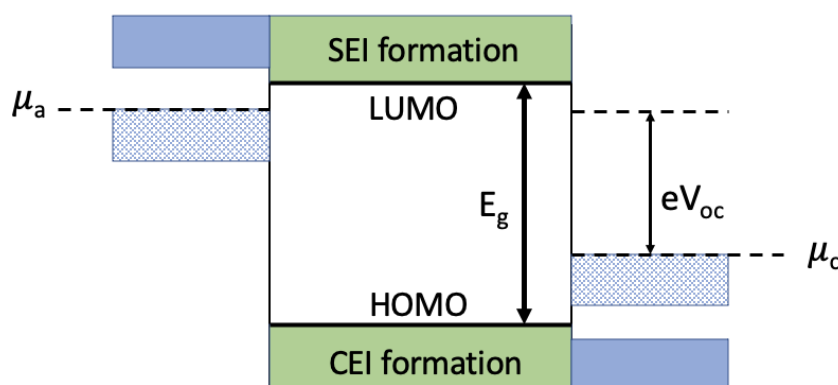


Figure 2.2: The band gap of an electrolyte together with the electrode potential of the anode and cathode material. The dotted boxes illustrate the scenario in which the electrolyte is stable, while the filled boxes show the situation where the electrolyte is unstable. Inspired by^[22].

2.4 Solid electrolyte interphase

The electrochemical potential of the anode is outside the stability window of the electrolyte before any cycles have been performed. Consequently, a solid electrolyte interface

(SEI) with a thickness of several nanometers is formed at the anode surface^{[22] [31]}.

Because the anode is outside the stability window of the electrolyte, the electron flow going from the graphite electrode reduces the electrolyte at the electrode- electrolyte interphase. The reduced species further react with lithium ions, and deposit at the surface of the negative electrode. The deposition mechanism is however yet to be fully understood. Until the publication "Near- Shore Aggregation Mechanism of Electrolyte Decomposition Product to explain the Solid Electrolyte Interphase Formation" written by Ushirogata et al. in 2015^[31] a "surface-growth mechanism" was evaluated as the most reasonable formation mechanism. However, Ushirogata et al. suggested in their article a "near- shore agglomeration" as a possible mechanism for the SEI formation. Here, the reduced species agglomerate close to the electrode surface before they are absorbed. The formation of the SEI-layer occurs during the first cycles. Because the SEI-layer has electrically insulating properties, it will function as a barrier for electrons passing. Therefore, as the layer becomes thicker, less electrons can pass through the electrode, hence the growth of the SEI-layer will eventually stop^[31].

The resulting SEI layer can be divided into two layers. Close to the anode surface, the film is dense and consists mainly of inorganic compounds, while a more porous layer containing mostly organic compounds dominates the outer layer^[32].

While the layer is electronically insulating it is however ionic conductive. This enables lithium diffusion into graphite, while simultaneously avoid further degradation of the electrolyte. In the paper "Lithium transport within the solid electrolyte interphase" by Lu and Harris^[32] they suggest that the electrolyte species only enables to penetrate the porous outer layer, while lithium ions can pass through the dense inner layer, which enables intercalation and deintercalation of the graphite electrode. Figure 2.3 gives a visual of the SEI layer at the graphite surface, in which lithium ions can pass and intercalate into the structure.

As the SEI-layer ensures no further degradation of the electrolyte, while at the same time allows for high lithium diffusion rate, the formation of SEI is essential for the battery performance^[33]. However, the layer has one major negative effect which is called the irreversible capacity loss. This loss occurs as lithium ions are consumed in the formation of the layer^[34]. The extent of this loss depends among others on the surface morphology of the negative electrode, and by the thickness and density of the SEI layer. During the first cycles, a 10 % loss can occur^[35], while for anodes made by nanosized graphite

particles the loss can be up to 50 % as the surface area of these particles are larger^[34].

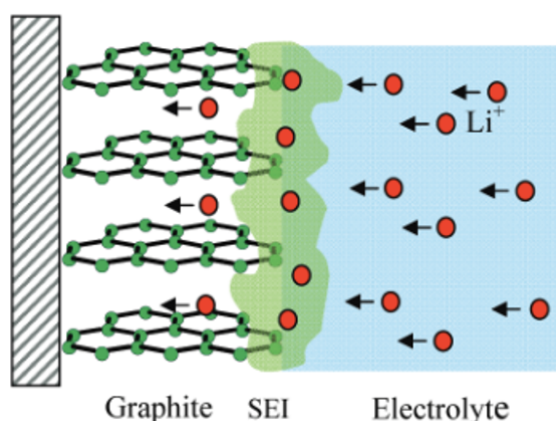


Figure 2.3: Illustration of the SEI layer at the graphite electrode surface. The figure shows how lithium ions can pass through the layer and intercalate into the graphite structure^[33].

2.5 Electrode materials

LIBs have shown good properties as they have high power- and energy- density. The good functionality can in some extent be explained by the properties of the lithium ion. Of all elements, the reduction potential of lithium is the lowest, giving LIBs a high cell potential, which according to Equation^[2.3] contributes to high energy. Additionally, its small radius and light weight makes lithium a favourable ion for charge transfer^[15].

The electrode selection is also important to obtain a good battery performance. To meet the demand from the industry, high energy- and power- density are needed. Firstly, the energy density depends on having a high cell voltage, which can be obtained by having an anode with low potential and a cathode operating at a high potential with respect to Li/Li^+ . Depending on the electrode material, LIBs normally operate at a cell potential between 3.2V and 3.85 V vs. Li/Li^+ ^[7]. Secondly, to achieve a high power density, it is essential to have fast transport of lithium ions and electrons. This is obtained by high electronic- and ionic- conductivity for both the anode- and cathode- material. In addition to high energy- and power- density, the capacity of the electrode materials is an important factor. Figure^[2.4] shows the voltage as a function of capacity for some of the most common cathode- and anode- materials. As can be seen, the capacities of the cathodes are lower compared to the anode-materials^[36]. Because the total battery capacity depends on both the cathode and anode, it is primarily limited by the cathode

material^[7]. Additionally, good anode- and cathode- materials are stable and do not react heavily with the electrolyte. From an industrial perspective, having lightweight-, cheap- and environmental friendly- materials are important factors. Unfortunately, the environmental aspect is still a challenge especially for cathode materials in conventional LIBs^[7].

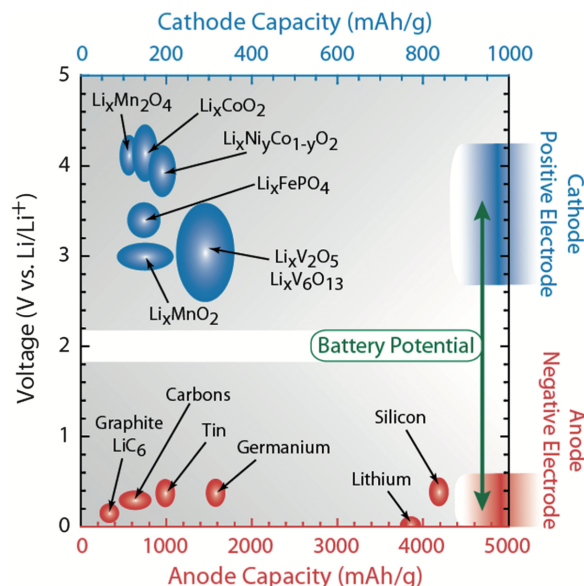


Figure 2.4: Voltage vs. capacity for multiple anode- and cathode- materials^[36]

2.5.1 Cathodes

In LIBs, it is desired to have cathode materials with high capacity, meaning that it can extract and store large amount of lithium ions without having major changes in the structure^[37].

There exist a broad variety of cathode materials for LIBs, all with different strengths and challenges. The main categories of cathode materials are intercalation- and conversion-cathodes. Intercalation cathodes can further be divided into transition metal oxides and polyanion materials^[15]. Two of the most common structures of transition metal oxides are layered and spinel.

Lithium cobalt oxide, (LiCoO_2) (LCO) is one of the most used layered transition metal oxides. This material has a relatively high practical capacity of 148 mAh/g, high average voltage of 3.8 V and good cycle stability^[15]. Unfortunately, this material has low thermal stability and high cost which is directly related to cobalt^[15]. To improve these expenses, research have been done trying to substitute cobalt with both nickel and manganese. Nickel decreases the costs and contributes to increase the capacity, while manganese im-

proves the thermal stability. This give rise to $\text{Li}(\text{Ni}_{0.5}\text{Mn}_{0.5})\text{O}_2$ (NMC). However, by removing cobalt the stability of the material is reduced. Therefore, today the most common NMC structure is $\text{Li}(\text{Ni}_x\text{Mn}_y\text{Co}_z)\text{O}_2$ [15].

Spinel is another common structure of transition metal oxides. An example of such structure is LiMn_2O_4 in which the pathway for diffusion of lithium ions is three-dimensional [38]. This material has a low cost, and is more environmentally friendly compared to LCO due to the absence of Co. However, the material has a lower experimental capacity of 120 mAh/g compared to LCO [15]. Additionally, long term cycling of this material can result in Mn dissolution which reduces the cycle stability of this electrode [15].

Polyanion is the second type of intercalation materials, in which Lithium iron phosphate, LiFePO_4 (LFP) with olivine structure is a common cathode. Compared to LCO, LFP has a better thermal stability, and a higher experimental capacity equal 165 mAh/g [15]. However, it's average voltage of about 3.4V is lower than for LCO. [15]. From a commercial perspective the material has the advantage of being simply processing and cheap. However, due to it's low conductivity the rate capability of LFP is relatively poor [39]. Consequently, LFP cathodes depend on being coated with a conductive material to be functional. As amorphous carbon shows high electrical conductivity and good chemical stability, carbon coating have been used to improve the properties of LFP cathodes [39]. Moreover, LFP has a flat voltage profile, meaning that in a LFP-graphite cell, graphite will dominate the voltage profile. This makes LFP a suitable cathode material when studying the properties of graphite [40].

In addition to intercalation cathodes, conversion cathodes have been introduced. During intercalation and deintercalation of conversion cathodes, chemical bonds are broken and recombined in redox-reactions [15]. In contrast to intercalation cathodes, the conversion cathodes do not contain lithium and hence must be combined with a lithium containing anode. Sulfur is an example of a conversion cathode which has a high theoretical capacity of 1675 mAh/g. However, due to it's low electrical conductivity and potential vs. Li/Li^+ , this cathode material is not commonly used [15].

2.5.2 Anodes

Similar as for cathode materials, an ideal anode should be able to store large amount of lithium ions, while at the same time remain a stable structure [7].

The literature distinguishes between three types of anode materials; intercalation, con-

version and alloying. The intercalation anodes are the most used materials, as they have low potential vs. Li/Li^+ , and shows long and stable cycle life^[41]. The most common intercalation material used in LIBs is graphite, which is explained in Section 2.6. During charge and discharge of these materials, lithium is intercalated and deintercalated into the structure^[5]. This mechanism is explained in Section 2.6.1. However, the intercalation materials have relative low capacity. As the demand for higher energy density increases, the industry has been forced to look for other suitable materials. Such materials are conversion anodes. In contrast to intercalation anodes, chemical reactions occur during lithiation and delithiation of these electrodes. This often results in structural changes of the core structure^[23]. Unfortunately, conversion anodes often suffer from morphology changes during cycling, resulting in degradation of the material. Furthermore, their conductivity is lower compared to the intercalation anodes^[42]. To replace intercalation anodes with conversion anodes, these challenges must be overcome^{[41] [42]}. The third group of anode materials are alloying anodes. In the literature, alloy anodes are often referred to as a type of conversion anodes due to their many similarities. Similar as the conversion anode, alloying anodes have high capacity, and suffers from low conductivity and volume expansion during charging. The main difference between these two materials are the mechanism during lithiation and delithiation, in which alloying elements forms a lithium alloy (Li-Y) instead of a chemical compound (Li_xY)^[23]. Silicon is one of the alloying anodes that have received considerable attention the last years. With a theoretical capacity of 4200 mAh/g ^[43], silicon have almost 10 times higher capacity than graphite (372 mAh/g)^[23]. Because of this, silicon is considered as a potential substitute for graphite in the future^[43].

2.6 Graphite as anode material

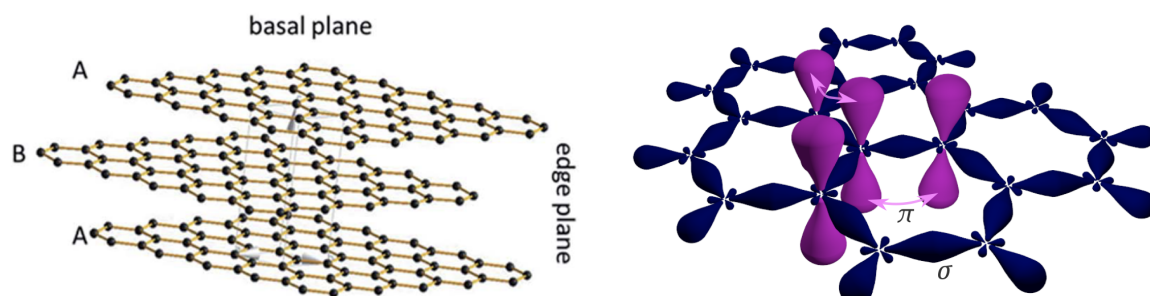
Graphite is the most used anode material in LIBs for multiple reasons. Firstly, it is highly abundant, non-toxic and in contrast to other anode materials it has a natural high conductivity. In terms of research and further improvements of graphite, it is a huge advantage that it's structure is well known and easy to study by a broad variety of techniques^{[23] [5]}.

These advantages are highly related to the structure of graphite. The material is built up by graphene layers consisting of hexagons of sp^2 - hybridized carbon atoms. The sp^2 hybridization gives three sp^2 - orbitals, and one p-orbital. The sp^2 orbitals are bonded

together with strong covalent σ - bonds. Due to the short bond-length, the electrons are localized close to the atom.

The graphene layers are kept together by weak Van der Waals bonds, in which p-orbitals constitutes the formation of π -bonds. These bonds are considerably longer compared to the σ - bonds, which make the electrons more delocalized in comparison to the electrons within the same graphene layer. This enable the layers to be easily separated, which makes graphite a good host structure for intercalation^[5]. The σ - and π - bonds for one graphene layer can be seen in Figure 2.5b. Furthermore, the material is built up by graphene layers with two main stacking sequences, namely ABCABC giving a rhombohedral symmetry and ABAB sequence giving a hexagonal graphite symmetry. Because the ABAB stacking is most thermodynamically stable, the hexagonal structure is the dominating structure of graphite^[5]. The layered stacking gives the structure two types of planes, namely the basal- and edge- plane. The basal plane is referred to the plane which is parallel to the graphene layers, while the edge planes is perpendicular to these layers. The layered structure showing the basal- and edge- plane is shown in Figure 2.5a^[5].

Because the bonds are different within and between the graphene layers, graphite have anisotropic properties, which can be seen from the conductive properties. In the basal plane, the conductivity is much larger compared to the edge plane with $2.25 \cdot 10^4 \text{ Scm}^{-1}$, compared to 5.9 Scm^{-1} in the edge plane^[5]. Moreover, as the edge plane has a higher surface energy, the surface reactivity would be higher her compared to the basal plane. As a result, intercalation of species is favoured in the edge planes^[5]. However, as lithium intercalation is favoured at the edge planes, the SEI-formation would also be largest in this region. Therefore, a combination of basal- and edge- planes are important to achieve high intercalation current while minimizing the irreversible capacity loss caused by the SEI formation^{[5] [44]}.



(a) Layered structure of graphite showing the edge- and basal- planes^[5]. (b) One graphene layer showing the σ - and π - orbitals^[45].

Figure 2.5: The graphite structure.

Although graphite delivers a capacity much higher than the conventional cathodes, improvements of graphite is needed to meet the demands for the future. One way to improve the properties of graphite is by reducing the SEI formation. In this regard carbon coated graphite particles have shown to give thinner SEI layer. Moreover, the carbon coating protects the graphite particles from direct contact with the electrolyte^[7]. In addition to coating, the morphology plays an important role for the performance of graphite anodes. More about this is described in Section [2.8](#).

2.6.1 Intercalation of lithium ions

When a battery is charged and discharged, lithium ions are intercalated and deintercalated into the graphite structure respectively. The charge- and discharge- reaction of graphite is shown in Equation [2.7](#), in which the LiC_6 configuration is the maximum stoichiometry possible. The mechanism during intercalation of lithium ions into graphite can be seen as characteristic voltage plateaus, having three main steps. The three voltage plateaus with the corresponding animation are given in Figure [2.6](#). The first step is random intercalation of lithium ions from the electrolyte into the solid electrode. This is followed by a first order phase transition from LiC_{24} to LiC_{18} . In the second step the number of intercalated graphite layers increases, giving a transformation from LiC_{18} to LiC_{12} . For the third and final step, the concentration of lithium ions in graphite increases such that the stoichiometry of LiC_6 is reached, giving graphite a theoretical capacity of 372 mAh/g^{[5] [23] [46]}.

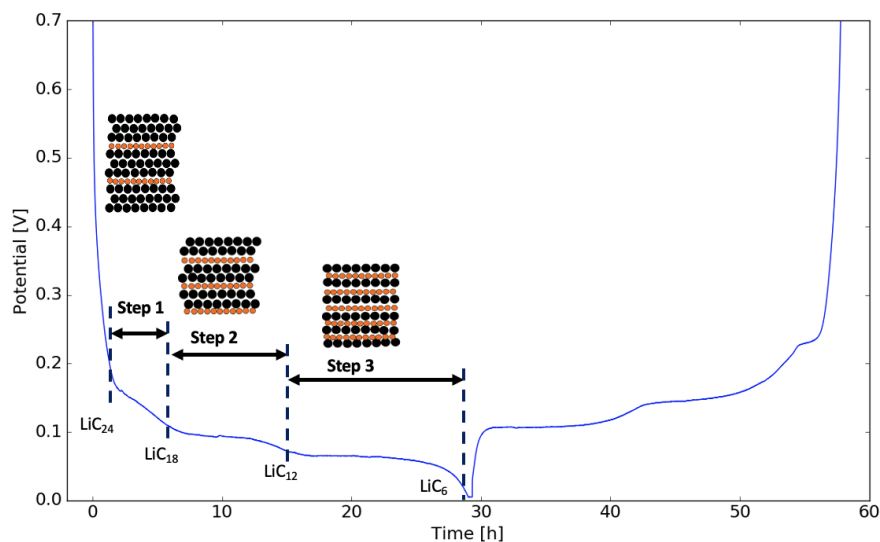


Figure 2.6: Cell potential vs. Li/Li^+ as a function of time during the intercalation and deintercalation at C-rate of C/30. The cell has graphite as the working electrode and lithium metal as the counter electrode.

As described in Section 2.6, lithiation is preferred in the edge planes. Within this plane there are two possible diffusion pathways. This concept is well described in the article "Diffusion of alkali metals in the first stage graphite intercalation compounds by vdW-DFT calculations" by Z. Wang et.al^[47]. The following explanation is based on this article. Firstly, the lithium ions can cross two carbon- carbon bonds (sigma bonds), and by this be transported into a new carbon ring. This pathway is shown as the curved red line in Figure 2.7. Here h is a parameter describing the curvature of this pathway. The second possible pathway is a straight line going over two carbon atoms, before the lithium ion reaches the new carbon ring. This pathway is shown as the blue line in Figure 2.7. Furthermore, the paper discussed the energy barriers of these two pathways. By comparing the relative energy of a vacancy defect diffusing in the two pathways, the curved pathway was found to be most energetically beneficial. Consequentially, the transport of lithium ions is faster for the curved pathway compared to the straight line, hence the longest pathway showed to be most likely.

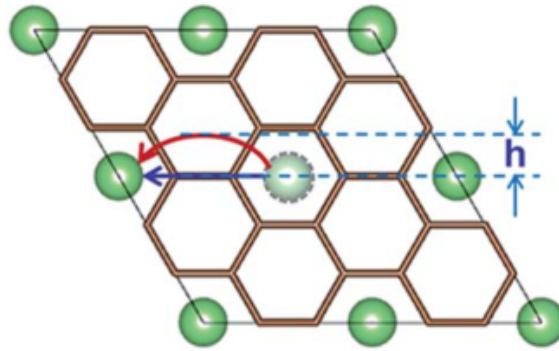


Figure 2.7: The brown lattice illustrates one graphene layer, while the green circles correspond to lithium ions. The blue and red line illustrates the two possible pathways for lithium ions to intercalate in the graphene layer^[47].

During the intercalation process, the interlayering distance between the graphene layers increases. When the capacity of graphite is fully utilized, the interlayering distance can increase up to 10.4 %^[5]. Moreover, as there naturally exists some defects in the graphite structure, the pathway available for lithium intercalation varies, giving an inhomogeneous lithiation process.

2.7 Degradation of LIB

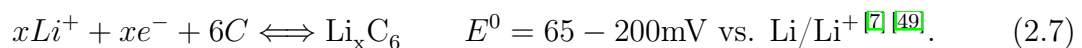
Naturally LIBs degrade over time, which causes both capacity- and power- fade, as well as safety concern such as thermal runaway, and short circuit. There are primarily two types of degradation mechanisms, namely mechanical and chemical. Mechanical degradation can for instance be caused by volume changes during intercalation and deintercalation [48]. Chemical degradation can be divided in three categories: loss of electrolyte, loss of active material and loss of lithium [8]. The formation of SEI-layer is one of the main reasons for loss of electrolyte, which also contributes to loss of lithium as explained in Section 2.4. Furthermore, the loss of electrolyte can also be caused by oxidative decomposition of solvents on the electrode. [28] [8]. Loss of active material is related to the loss of anode- and cathode- material. This can be due to electrode particle cracking, structural changes, and dissolution of the active material in the electrode. For graphite, the active material can also be reduced due to lithium metal being deposited at the surface and by this blocking the active material. This type of degradation also gives loss of lithium in a process called lithium plating [8] [28].

This degradation mechanism has received a lot of attention the last years as it is triggered by fast charging. Because the demand of fast charging increases, the need for limiting the extend of plating becomes important [8]. This requires a good understanding of the plating mechanism as well as factors contributing to it. More of this is elaborated in the following sections.

2.7.1 Lithium plating

Lithium plating is one of the worst degradation mechanisms in LIBs because it constitutes a safety concern as well as degradation of the battery.

As explained in Section 2.1, lithium ions are extracted from the positive electrode and intercalated into graphite during charging. However, in some cases lithium is deposited at the anode surface instead of being intercalated. This process is referred to as lithium plating. Because of this, there are two competing reactions during charging namely intercalation and lithium plating. These two reactions are shown in Equation 2.6 and 2.7 [49].



The intercalation of graphite occurs at a potential range of 65-200 mV vs. Li/Li^+ [49]. This means that at potential within this range, interaction is the thermodynamic favourable reaction. However due to polarization of the negative electrode, the potential can drop below 0V which allows lithium plating at the graphite surface [8].

The literature distinguish between three possibilities for lithium metal to be deposited at the electrode surface. Firstly, lithium can be deposited as part of the SEI-layer, which is explained in Section 2.4. The other possibility is plated lithium, which is divided in two categories. If the plated lithium has electrical contact with the electrode, it can be stripped of during discharge and by this once again function as active lithium ions. However, if the contact is lost, stripping would not be possible. Such lithium is often referred to as "dead"- lithium and is the worst type of lithium deposition as it contributes to a significant capacity loss and degradation of the battery [8].

Lithium plating degrades the battery performance in multiple ways. Firstly, as lithium is deposited at the surface of the electrode, the active surface area of the electrode is reduced, hence less ions can be intercalated, and the capacity is reduced. Additionally, the dead lithium blocks the pathway to the available sites, and by this creates a more tortuous pathway for the remaining active lithium [8]. Moreover, the plated lithium can form a SEI-layer which consumes more electrolyte. However, the biggest concern is related to the safety. If the deposition of lithium metal continues, the separator can be punctured, which results in short circuit of the cell [50]. It is therefore important to reduce the degree of lithium plating. To be able to do this, an understanding of factors contributing to plating is needed. This is given in Section 2.7.2.

2.7.2 Factors influencing lithium plating

The intercalation of lithium ions depends on the solid state diffusion in graphite, and the diffusion in the porous electrode. An illustration of this concept is presented in Figure 2.8. Here, the graphite particles close to the electrode surface are first being fully lithiated. The particles closer to the current collector have a lower degree of lithiation at a given time due to the longer transportation length. Please note that the degree of lithiation of the graphite particles only is illustrative.

Moreover, the concentration of lithium ions in the electrolyte decreases as it approaches the current collector. This can be explained as most of the lithium ions are being intercalated before they reach the current collector [51]. With this concept in mind, factors

contributing to lithium plating can be understood. The paper "Lithium Plating Mechanism, Detection, and Mitigation in Lithium-Ion Batteries" written by Xianke Lin et. al^[8], presents fast charging, high state of charge and low temperature as three important factors contributing to lithium plating. The following paragraphs explain how these factors promote plating and is based on this paper.

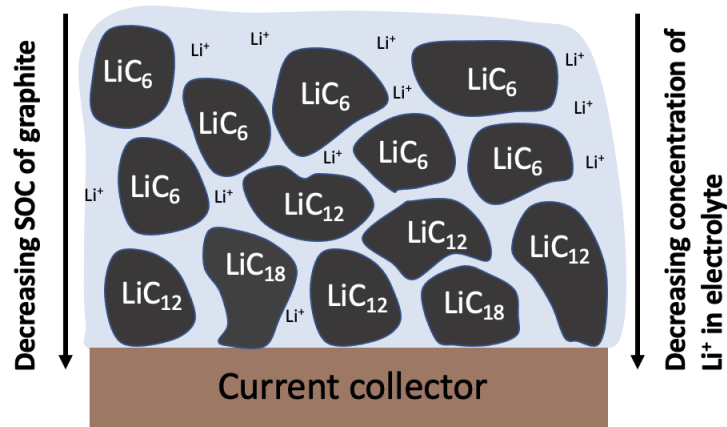


Figure 2.8: Illustration of lithiation of graphite electrode. The graphite particles close to the electrode surface reach fully lithiation faster compared to the particles close to the current collector. Also, the concentration of lithium ions in the electrolyte decreases closer to the current collector.

Fast charging is one of the biggest contributors to lithium plating. In this case, the high charging current results in a high flow of lithium ions towards the electrode. If this current exceeds the intercalation current, the concentration of lithium ions at the surface increases. This often leads to polarization of the electrode, which triggers lithium plating^{[52] [8]}.

In addition to fast charging, the state of charge plays an important role regarding lithium plating. The probability of plating increases at high SOC. At this condition most of the active sites are already being occupied. If the charging continues in this condition, the electrode would quickly be saturated, and the remaining ions will rather be deposited at the electrode surface^[8].

Low temperature is a third factor that has shown to have a huge influence on the probability of lithium plating. When the temperature is reduced, the viscosity of the electrolyte increases which inhibits its ability to penetrate the porous graphite structure. This will reduce the intercalation rate of lithium ions. Further, a low temperature results in low kinetics, which also reduces the intercalation rate. The consequence is lithium ions accumulating at the electrode surface rather than being intercalated^{[53] [8]}.

By evaluating these three factors, it becomes clear that the diffusion rate of lithium is the limiting factor for why both fast charging and low temperature often results in lithium plating. The diffusion rate of lithium is among other affected by the morphology of the graphite electrode. As both the porosity, tortuosity and particle size and shape affect the electrode structure, these factors are important to evaluate when reducing the extend of plating. Discussions of these parameters are given in Section [2.8](#)

2.7.3 Investigation of lithium plating

As lithium plating constitutes a big concern regarding the degradation and rate performance of the battery, comprehensive work has been done to reduce this effect. To determine the effect of these measures, tools allowing to detect the amount of lithium plated at the electrode surface are needed. Unfortunately, this appears to be difficult, which among other is due to the low atomic weight of lithium [\[8\]](#). In the following paragraph, some of the most common techniques are presented.

One way to detect lithium plating is by post- mortem characterization. In this technique, the cell is disassembled which sets some limitations to which state the battery can be investigated. Having opened the cell, SEM can be used to investigate the electrode surface. However, due to the low atomic weight of lithium, it is challenging to obtain strong signals. Lithium may therefore not be visible or appear as weak shadows at the electrode surface. As lithium is hard to detect by SEM, pictures of a cycled electrode should be compared to SEM micrographs of an uncycled electrode to easier detect any differences [\[54\]](#) [\[8\]](#). An example of how lithium deposition can be observed by SEM are shown in the article "Stable Li Metal Anodes via Regulating Lithium Plating/Stripping in Vertically Aligned Microchannels" written by S.H. Wang et. al [\[55\]](#). Here they present SEM micrographs of lithium deposition at Cu- current collectors with different morphology. Their results show that lithium metal deposition has a worm- like structure.

In addition to SEM, other post- mortem characterization techniques such as Transmission electron microscopy (TEM) and Atomic force microscopy (AFM) can be used [\[8\]](#).

As opening the cell risks contamination of the sample, it is preferred to have a method that does not rely on disassembling the cell. One example of such method is the Differential Voltage Analysis (DVA). By studying the OCV and the voltage plateaus described in Section [2.6.1](#), the amount of lithium being stripped off the electrode can be calculated [\[56\]](#).

2.8 The effect of electrode morphology

2.8.1 The effect of porosity

As it appears from Section 2.7.2, the diffusion of lithium in the porous electrode is an important factor to consider when limiting the extend of lithium plating. The time for lithium ions to diffuse into the electrode material is proportional to the ratio of the square of the diffusion length (l) to the diffusion coefficient (D) which can be seen in Equation 2.8

$$t \sim \frac{l^2}{D} \quad (2.8)$$

This equation shows that the diffusion time of lithium ions can be reduced by decreasing the diffusion length or increasing the diffusion coefficient. The diffusion coefficient can be increased by doping. Unfortunately, this requires chemical changes of the electrode material. Therefore, to avoid this, reduction of the diffusion length by using porous electrodes have been evaluated as one possible solution to reduce the diffusion time. As explained in Section 2.6.1, lithium ions are intercalated and deintercalated through the edge-planes of graphite^[57]. By having a porous electrode, the pathways to these intercalation sites becomes more accessible which improves the diffusion time^[10]. Moreover, in a porous electrode the electrolyte enables to penetrate deep into the structure, which improves the transport of lithium ions and hence also the intercalation rate^[10]. In this way, more of the active electrode material is being utilized.^[57] Porous electrodes also improve the stability of the battery as it limits the volume expansion that occurs during intercalation and deintercalation of lithium ions^[10].

Clearly, there are many advantages of using porous graphite electrodes. However, there are challenges associated to this. A porous electrode has a lower loading, which reduces the energy density of the battery. As the demand for high energy batteries increases it is preferred to have batteries with high loading electrodes. Such type of electrodes is thick and have a high density. Regarding the porosity, a compromise are therefore needed to increase the diffusion rate while ensure as high loading as possible^[11]. Adjusting the thickness is another way to increase the loading, however this have also caused challenges. As the thickness increases, the diffusion length of lithium ions increase which can result in a reduction of the power density of the battery. Having a thick electrode, therefore sets

even higher demand for good transport of the electrolyte in the electrode structure^{[58] [11]}. The effect of thickness on graphite anodes have been investigated in the paper "Optimizing Areal Capacities through Understanding the Limitations of Lithium-Ion Electrodes" written by Gallagher et. al^[58]. Three electrodes with thickness of 58 μm , 97 μm and 127 μm were used, which gave corresponding capacity of 2.2 mAh/cm², 3.3 mAh/cm² and 4.4 mAh/cm². The electrodes had porosity equal 39 % \pm 0.02. The result can be seen in Figure^{2.9}. This shows that the thickest electrodes had largest amount of lithium plating on the surface.



Figure 2.9: Graphite electrodes with different thicknesses and loading of 58 μm (2.2mAh/cm²), 97 μm (3.3 mAh/cm²) and 127 μm (4.4 mAh/cm²) after cycling^[58].

From this, it becomes clear that a compromise between porosity and thickness is needed to find a perfect balance between high power-and energy- density. One solution to achieve the benefits of porous electrodes, while retain high loading of the electrodes is to use graded porosity electrodes. These electrodes have highest density close to the current collector and a lower density near the electrode surface. This enable lithium ions to be quickly transported into the electrode structure at the surface, such that the amount of lithium ions accumulating at the surface decreases. The diffusion of lithium ions further into the structure would then become more challenging as the density increases which causes more tortuous pathways^{[11] [12]}.

The effect of porosity graded graphite electrode was studied by comparing it's performance to a single layered graphite electrode in the article "Graded Porosity Electrode for Fast Charging Lithium-Ion Battery" written by Jian Yang et. al.^[12]. Here, lithium metal was used as the counter electrode. The graded electrode was made by three layers in which the bottom-, middle- and top- layers had porosity of 15 %, 25% and 35 % respectively. The single layered electrode had a porosity equal 25% which corresponded to the average porosity of the graded electrode. Their result showed that both electrodes

achieved approximately similar maximum capacity, while the graded electrode obtained higher capacity when increasing the C-rate. Moreover, the cycle life of the graded electrode was better compared to the single layered electrode.

2.8.2 The effect of tortuosity

In addition to the porosity, tortuosity plays an important role to improve the transport of lithium ions. This parameter provides information about the transport pathway through the electrode, which affects the electrolyte's ability to diffuse into the porous electrode^[9]. The tortuosity can be expressed as the ratio of the actual curved length, L_c to the direct distance between the two curved ends L .

$$\tau = \frac{L_c}{L} \quad [59] \quad (2.9)$$

According to Equation [2.9](#), a straight line will give a tortuosity equal 1. In the case of τ being larger than 1, the pathway would be longer. Consequently, the transport length of the electrolyte containing lithium ions into the porous electrode is longer^[9].

In 2020 Hao Chen et. al. published the article "Tortuosity Effects in Lithium- Metal Host Anodes", where they studied three graphite structures namely vertically aligned, random reduced graphene oxide and horizontally aligned, with tortuosity of 1.25, 1.76 and 4.46 respectively^[9]. They found that the high tortuosity electrodes had an uneven transportation of lithium ions which resulted in a lower cycling performance. In comparison, the low tortuosity electrodes had better cycling performance as the transport of lithium ions were more uniform.

Their observations were explained by evaluating how the tortuosity affected the transportation length of lithium ions. From Equation [2.9](#) it is given that a high tortuosity causes a longer transportation length of lithium ions in the porous electrode. Consequently, the intercalation rate decreases, and a longer time is required to reach 100 % state of charge. The decrease in intercalation rate can also cause lithium ions piling up at the electrode surface, hence the risk of lithium plating increases.^[60]

Another aspect of tortuosity is related to local unevenness in current density. As described in Section [2.7.1](#), one of the problems with plating is the bottleneck metallic lithium constitutes. This causes uneven current distribution such that some areas receive a high current density which amplifies degradation of the battery. This effect would be lower

for electrodes having a low tortuosity, as the transport of lithium ions are more evenly distributed through the electrode^[9].

From this, it becomes clear that an electrode with low tortuosity is preferred to achieve a good cycling performance. This have specially been evaluated as a good solution to allow thicker electrodes without sacrificing the rate capability^[61].

To express the relation between the porosity and the tortuosity of an electrode MacMullin number have been introduces. This parameter gives information about the microstructure of the electrode, and is presented in Equation [2.10](#).

$$N_M = \frac{\tau}{\epsilon} = \frac{\sigma}{\sigma_{ion}} \quad [59] \quad (2.10)$$

Here, τ is the tortuosity, ϵ is the porosity, σ is the conductivity of the electrolyte, σ_{ion} is the effective ionic conductivity of an electrode or a separator^[59]. From Ohms's law the resistance R is given by

$$R = \frac{d}{\sigma \cdot A} \quad (2.11)$$

in which A is the surface area of the electrode, and d is the thickness of the electrode^[20]. By combining Equation [2.10](#) and [2.11](#), the tortuosity can be expressed as shown in Equation [2.12](#), where R_{ion} is the ionic resistance. This equation can be used when calculating the tortuosity from impedance spectroscopy results. Due to the symmetry of the cell, the factor $1/2$ is added to the equation^[59].

$$\tau = \frac{R_{ion} A \sigma_{ion} \epsilon}{2d} \quad (2.12)$$

2.8.3 Effect of particle size and shape

In addition to porosity and tortuosity, the particle size is also an important factor influencing the performance of an electrode.

The intercalation process of lithium ions can be limited by either the reaction at the graphite surface, or by the diffusion of ions in the bulk. For large particles, a larger transportation distance, hence also a larger diffusion time, is required for lithium to reach the center of the graphite particle. In this case the intercalation is said to be bulk transport limited^[60]. In the opposite case, for small particles, the distance into the center is smaller, meaning that a shorter time is required for lithium ions to reach the center.

In addition, the amount of lithium ions needed to reach a high state of charge is lower for smaller particles. For this case, the intercalation is more likely to be limited by the surface-reaction. The particle size is therefore an important parameter for the intercalation of lithium, hence also the overall electrode performance^[60].

Although small particles tend to give better performance of the electrode^[62], there are some limitations related to these particles. Small particles have a larger surface area which increases the SEI formation and hence contributes to a larger irreversible capacity loss^[44]. Moreover, the tortuosity is affected by the particle size. Smaller particles tend to increase the tortuosity, which according to the theory presented in Section 2.8.2 reduces the rate-performance^[60]. Therefore, a compromise of having small particles to quicker reach a high SOC, and larger particles to reduce the SEI-formation at the electrode surface is needed.

Moreover, the effect of particle size distribution on graphite electrodes was investigated in the paper "Simulating the Impact of Particle Size Distribution on the Performance of Graphite Electrodes in Lithium-ion Batteries" written by Fridolin Röder et. al.^[62]. Their result showed that for graphite powders having a broad size distribution, the capacity tends to be lower compared to powders with a smaller distribution. Additionally, the particle size also affects the current distribution in the electrode. As different particle sizes have different surface area to volume-ratio, inhomogeneous current densities are expected for powders with a large particle size distribution. Consequently, the degradation is also expected to be higher for these powders^[62].

In addition to the particle size, its shape and orientation does also affect the performance of the electrodes. As described in Section 2.6 intercalation of lithium is most preferred in the edge planes. Having graphite particles with a high number of available edge-planes are therefore important for the intercalation rate. However, a too high edge-to basal-plane ratio increases the SEI-formation. Therefore a compromise is needed to optimize the electrode performance^[44].

2.9 Electrochemical characterization

2.9.1 Galvanostatic cycling with potential limitations

Galvanostatic cycling with potential limitations (GCPL) is one of the most used techniques when studying the performance of batteries. When cycling, a constant current

is applied in which the charge- and discharge- rate is determined by the C-rate. One advantages with this technique is the opportunity to control the potential of both the working-, and counter- electrode vs. the reference electrode for a three-electrode cell by using a potentiostat [\[63\]](#).

2.9.2 Electrochemical impedance spectroscopy

The following explanation of electrochemical impedance spectroscopy (EIS) is based on the report "Application note, Basic of Electrochemical Impedance Spectroscopy" [\[64\]](#).

While ohms law express the resistance for an ideal resistor, the impedance can be used for a broader variety of systems. For an ideal resistor, it is assumed that the resistance is independent of the frequency, and that the system follows Ohm's law. Additionally, the voltage- and AC current- signals are assumed to be in phase with each other. However, for conventional batteries, this is not the case. Most circuits contain multiple circuit elements, which gives systems in which Ohm's law no longer is sufficient. For this reason, impedance have been introduced as a more general term for expressing the resistance in a system.

When measuring the impedance, an AC potential (PEIS) or current (GEIS) is applied while measuring the current or potential respectively. For PEIS, the applied potential is usually sinusoidal, which results in a sinusoidal response of the current. In contrast to an ideal resistor, the current would be phase- shifted. Based on Ohm's law, the impedance can be expressed by the ratio of the potential at a given time (E_t) to the current at a given time (I_t) as shown in Equation [2.13](#). Here, ϕ is a parameter representing the phase-shift, ω is the angular frequency, and E_0 and I_0 is the amplitude of the potential and the current signal respectively.

$$Z(\omega) = \frac{E_t}{I_t} = \frac{E_0 \sin(\omega t)}{I_0 \sin(\omega t + \phi)} \quad (2.13)$$

The impedance is normally given as a complex function. This is obtained by using Euler's relation which gives

$$Z(\omega) = \frac{E_0}{I_0} (\cos(\phi) + i \cdot \sin(\phi)) \quad (2.14)$$

where i is the complex number.

The impedance measurements are often presented as a Nyquist Plots, in which the imaginary part is plotted as a function of the real- part of the impedance equation. The experimental values are later fitted to an equivalent circuit model. The choice of equivalent circuit model depends on the system and requires a good understanding of the different elements. Each model has its own unique expression for the impedance which is based on the impedance for each circuit element. The impedance for the elements used in this work are presented in Table 2.1. Where R_{ion} is the ionic resistance, ω is the angular frequency, τ is the local tortuosity, and Q and α are parameters both related to the constant phase element [63].

Table 2.1: Circuit elements used in this work with corresponding impedance.

Element	Impedance
Resistor	R [64]
Capacitor	$\frac{1}{iC\omega}$
Constant phase element	$\frac{1}{Q(i\omega)^\alpha}$ [64]
Warburg (finite-open)	$\frac{Z_w}{(i\omega\tau_w)^{\alpha_w}} \coth((i\omega\tau_w)^{\alpha_w})$ [65]
Transmission line model (simplified)	$\sqrt{\frac{R_{ion}}{Q \cdot (i\omega)^\alpha}} \cdot \coth\left(\sqrt{Q \cdot R_{ion} \cdot (i\omega)^\alpha}\right)$ [59]

The constant phase element is an element used for cases which have unideal capacitors. If the parameter α equals one, the constant phase element equals a capacitor [66]. The Warburg element express the 1D lithium diffusion and becomes dominating at low frequencies. There are mainly three types of Warburg elements namely infinite- and finite-Warburg, in which finite Warburg can be divided into transmissive (short) and reflective (open). In the infinite model the diffusion is unrestricted by assuming a large planar electrode, in which the diffusion region is much larger than the diffusion length [67] [68]. However, in some cases the diffusion of lithium ions is restricted by the diffusion region, meaning that the diffusion length is not infinite. In this case a finite Warburg model have been established. For cases with a finite diffusion length without a blocking boundary, a Warburg short element is used. For the finite open Warburg element on the other hand, the diffusion of charge carriers is limited by a blocking boundary. For graphite electrodes, the active particles and the pores filled with electrolyte are small. Additionally, the thickness of the electrode is thin, such that some of the lithium ions enables to

penetrate through the entire electrode. This gives a finite diffusion length. Moreover, a blocking boundary is obtained from the current collector in which no lithium ions can pass. Therefore, of the three Warburg elements, the finite open element describes the diffusion in a graphite electrode best [\[51\]](#) [\[69\]](#).

The transmission line model is used in this work to calculate the tortuosity of electrodes. In the paper "Tortuosity Determination of Battery Electrodes and Separators by Impedance Spectroscopy" written by J. Landesfeind [\[59\]](#), this model was used to find the ionic resistance in porous electrodes. The following presentation of the TLM- model is based on this article.

This model can be used to describe the ionic resistance in a porous electrode filled with electrolyte. In this model, the electronic resistance in the solid phase is given by ohmic resistors connected in series. In the liquid phase, the ionic resistance is given by a series of ionic resistors. Furthermore, the surface impedance element represents the charge transfer between the two phases which can occur as non-faradaic or faradaic reactions.

As this is a complex model, some simplifications can be made. Firstly, as the surface roughness of the materials affects the geometry of the system, a constant phase element is used instead of an ideal capacitor. Moreover, because the conductivity of carbon is high, the electronic resistance in the solid phase is considerably smaller compared to the ionic resistance in the liquid phase. As a result, the electronic resistance in the solid phase is neglected. The circuit element of the simplified transition line model can be seen in [Figure 2.10](#) in which q represent the contribution from the constant phase element, and r_{ion} is the ionic resistance. Here, the green lined area illustrates the solid phase, while the red area represents the electrolyte. This model is often presented as M_a in a circuit.

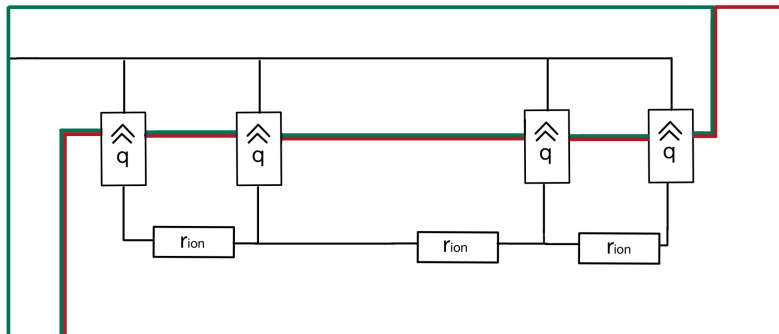


Figure 2.10: Circuit element use to fit the impedance data from the tortuosity measurements. The model is named the simplified transition line mode. Inspired by [\[59\]](#).

2.9.3 Ionic conductivity measurement with electrochemical impedance spectroscopy

Electrochemical impedance spectroscopy can also be used to find the conductivity of an electrolyte. The conductivity is given by Equation [2.15](#), where K_{cell} is the cell constant, and R_{el} is the resistance in the electrolyte.

$$\sigma = \frac{K_{cell}}{R_{el}} \tag{2.15}$$

The cell constant is a parameter which gives information about the volume between two electrodes and is often given in cm^{-1} . For a cell with a simple geometry, the cell constant is given by the ratio of the distance between the electrodes to the surface area of it. An example of such system is two parallel electrodes. However, for more complex structure, the cell constant can't be found directly from the geometry. For these cases, the cell constant can be calculated from Equation [2.15](#), in which the resistance of the electrolyte is found by EIS of a solution with known conductivity.

2.10 Physicochemical characterisation techniques

2.10.1 Scanning electron microscopy

Scanning electron microscopy (SEM) is a technique used to investigate the sample morphology, by having an electron beam interacting with the sample surface. Apertures and lenses are used to obtain a focused beam. To avoid the electrons colliding with particles when being accelerated, the system is under vacuum during the measurements. When the electrons interact with the sample surface, three main signals are being formed namely, X-rays, secondary- and backscattered- electrons. These signals are collected by detectors which generate an image of the sample. Because these signals are generated differently, they also contain different information. When using the scanning electron microscope, it is therefore important to understand the usage of these signals.

Secondary electrons have their origin from the sample and are generated during an inelastic reaction between the sample and the electron beam. These electrons are generated at the surface and do therefore provide information about the sample surface. In contrast, backscattered electrons provide information of the material deeper down in the sample. These electrons have their origin from the electron beam and are generated when they are backscattered from the sample during an elastic interaction with the sample. The

intensity of the backscattered electrons is highly dependent on the atomic number of the elements they were backscattered from. Elements having a high atomic number generates more electrons which makes them brighter compared to elements having a lower atomic number. However, backscattered electrons do not give the exact element, it can only be used to distinguish between high- and low- atomic number elements. One way to identify the different elements in a material is by using Energy-dispersive X-ray spectroscopy (EDS). As every material generates X-rays with a unique energy, these signals can be used to determine the different elements. [\[71\]](#) [\[72\]](#).

2.10.2 BET surface area measurement by BET- theory

Brunauer- Emmett- Teller-(BET) theory is used to measure the specific surface area of a sample, and is usually given in m^2/g . To remove physically bonded impurities, the sample is degassed before the specific surface area is measured by applying a gas, usually nitrogen or argon. As the gas are being added, the sample surface will physically adsorb the gas molecules. Eventually, the saturation point is reached, in which no more gas is adsorbed. As the amount of gas being applied is known, the amount of gas being adsorbed can be measured based on the change in pressure during the adsorption process. From this, the specific surface area of the sample can be found. Because the interaction between the solid and gaseous phases are relative weak at room temperature, a cryogenic temperature is used, typically by using liquid nitrogen [\[73\]](#)

2.10.3 Laser diffraction

Laser diffraction is the most used method to measure the particle size distribution of a powder and is specially favoured for particles in the range of 0.5 to 1000 microns. When the laser beam interacts with the sample, the beam is scattered by the particles. The angle at which the light is scattered is inverse proportional to the particle size, meaning that large particles give a small scattering angle, while small particles provide larger angles. By detecting the scattering angles, the PSD of the powder can be detected. The fact that particles within the same powder obtain different shapes constitutes a challenge for determine the particle size. As spheres are the only shape that can be described in 1D, the particle size distribution technique assumes the particles to be spheres. [\[74\]](#) [\[75\]](#).

3 Experimental

Three main experiments were performed in this project. Firstly, the tortuosity of electrodes made by two different powders was measured. Afterwards, the rate-performance of these electrodes were studied. The last experiment considered porosity graded electrodes. Before these experiments were performed, the specific capacity of the powders was found, and the slurry recipes were optimized. The experimental procedures of these experiments are presented in the following sections.

The C-rates used for testing were based on the graphite electrode using the specific capacity of the powders. In the description of the experimental procedure, lithiation and delithiation is referred to the graphite electrode. All experiments were performed at constant temperature of 25 °C.

3.1 Materials

The materials used in the project are presented in Table 3.1 with corresponding producer and purity.

Table 3.1: Materials used in the project with corresponding producer and purity.

Material	Supplier	Purity
C45, Carbon black	MTI CORP	
CMC 2000PA, Sodium Carboxyl Methyl Cellulose	Daicel	
Celgard 2400 separator	Celgard	
Graphite	Vianode	
SBR100, Styrene butadiene rubber (15 wt% in water)	Targray	
Ethylene carbonate	Sigma Aldrich	≥ 99 %
Dimethyl carbonate	Sigma Aldrich	≥ 99 %
Tetrabutylammonium hexafluorophosphate (Bu ₄ NPF ₆)	Sigma Aldrich	98 %
Insulating sleeve, PP; Li-referance, Separator FS-5P	EL-cell	
LiPF ₆ ; 1.2 mol/L lithium hexafluorophosphate in (3:7 wt %) Ethylene carbonate: Ethyl methyl carbonate + 2wt % Vinylene carbonate	Solvionic	
LFP (LiFePO ₄)	Customcells	

3.2 Powder characterization

Two synthetic graphite powders with different morphology were tested both which were provided by Vianode. These powders are referred to as S48 and S93 further in this report. To obtain a visual of the differences, SEM micrographs were taken, and BET- and PSD-

analyses were performed on the powders. Sections [3.2.1](#), [3.2.2](#) and [3.2.3](#) describes the experimental procedure for these experiments.

3.2.1 Morphology

The morphology of the powders was investigated by SEM using Zeiss-Supra 55VP. The powders were applied onto a carbon tape, and secondary electrons were used for imaging. An accelerating voltage of 10 kV was used.

3.2.2 Particle size distribution

The particle size distribution of the powders was measured on a Horiba Partica LA-960. The powder was added in small amounts until the transmittance had reached approximately 90%. Isopropanol was used as solvent, and the chosen refractive indexes equal $1.920 - 0.522i$ (real and imaginary part) and 1.378 for carbon and isopropanol respectively. To avoid agglomeration of the powder, ultrasound combined with an increased stirring rate was used for 10 minutes before the measurements.

3.2.3 BET-surface area

The BET-surface area of the two powders given in m^2/g were measured by nitrogen adsorption. The powder was degassed by using a Micromeritics SmartPrep. Nitrogen gas (N_2) was used to flush the powder with a temperature ranging from 30 to 250 °C, having a temperature ramp rate equal 10 °C /min. At 30 °C and 90 °C, the temperature was kept constant for 10 and 60 minutes respectively. When the temperature had reached 250 °C, it was held constant for 1000 minutes. The degassing procedure was finalized by lowering the temperature to 30 °C which was held constant for 100 minutes. Liquid nitrogen was used to achieve a cryogenic temperature, and nitrogen gas was used as the absorption gas. A Micromeritics 3-Flex Surface characterization was used for the measurements.

3.3 Slurry production and tape casting

The graphite electrodes were made by tape casting a slurry onto a current collector. This section gives the experimental procedure of slurry production and manufacturing of anode laminates.

The graphite electrodes were made by a slurry consisting of carbon black (C45), graphite, carboxymethylcellulose (CMC-solution) and a 15 wt% styrene- butadiene rubber (SBR)-

solution. The aimed slurry composition was based on a recommendation from Vianode which is shown in Table 3.2.

Table 3.2: Aimed slurry composition based on recommendation from Vianode.

	Graphite [wt%]	Carbon black [wt%]	CMC [wt%]	SBR [wt%]
Aimed composition	95	2	1.5	1.5

Prior to the slurry mixing, a CMC-solution with aimed concentration of 1.5 wt% was made by mixing CMC- powder and deionized water to a homogeneous solution. The CMC-powder was added to a container before the deionized water was supplied. A centrifugal vacuum mixer was used to mix the components by using the program presented in Table 3.3. To obtain a homogeneous solution, a spatula was used to crush eventual lumps in the solution after mixing. Accordingly, the procedure was repeated until a clear solution was formed. Calculations used to find the amount needed of each component are shown in Appendix B.1.1.

Table 3.3: Mixing program used to mix the CMC-solution. The program was performed by a centrifugal vacuum mixer.

Mixing program for CMC-solution
500 rpm in 60 sec. Vacuum: off
2000 rpm in 3300 sec. Vacuum: off
2000 rpm in 180 sec. Vacuum: on

After the CMC-solution was made, the slurry was manufactured. To achieve a homogeneous slurry, a centrifugal vacuum mixer with an optimized mixing program was used. The different programs are shown in Table 3.4.

The slurry was made by adding the CMC-solution to a container before carbon black was added and mixed with program 1 from Table 3.4. Afterwards, deionized water was added to the container and mixed with program 2. The amount of water depended on the targeted loading. The procedure was followed by adding graphite, and then homogenise it with program 3. Finally, SBR was added, and the slurry was finalised with program 4. Appendix B.1.2 presents the calculations used to find the amount of each component based on the aimed composition shown in Table 3.2.

Table 3.4: Mixing program for slurry production preformed by a centrifugal vacuum mixer.

Number	Program for slurrymixing
1	500 rpm for 60 sec. Vacuum: off 2000 rpm for 660 sec. Vacuum: off
2	500 rpm for 240 sec. Vacuum: off 2000 rpm for 600 sec. Vacuum: off 2000 rpm for 120 sec. Vacuum: on
3	500 rpm for 240 sec. Vacuum: off 1500 rpm for 120 sec. Vacuum: on 2000 rpm for 300 sec. Vacuum: off rest : 30 sek 2000 rpm for 300 sec. Vacuum: off 500 rpm for 100 sec. Vacuum: on
4	500 rpm for 60 sec. Vacuum: off 1000 rpm for 60 sec. Vacuum: on 1000 rpm for 60 sec. Vacuum: off

The final slurry was used to make anode laminates having copper-foil as the current collector. The thickness of the electrodes was controlled by using a rectangular four-sided fixed gap frame applicator from Zehntner. For the experiments performed in this project, gap-sizes of 50 μ m, 100 μ m, 150 μ m and 200 μ m were used. Section 3.6 provides detailed explanation of the different gap-sizes and solid/liquid-ratios used. To obtain a homogeneous anode laminate, ethanol was applied between the Cu-foil and the bottom of the tape caster before the foil was smoothed out. An image showing the procedure of tape-casting is presented in Figure 3.1. After tape-casting, the anode laminates were dried at 60 °C for 12 hours before the electrodes were punched out.

**Figure 3.1:** Experimental procedure of tape-casting.

3.4 Cell assembly

During this project, both coin cells and 3-electrode cells were used. Section [3.4.1](#) and [3.4.2](#) explains the assembly of coin cell and 3-electrode cell respectively. The assembly of both cells were performed inside an argon filled glove box.

3.4.1 Coin cell

The coin cells were made with Hohsen 2016 parts, having lithium metal as the counter electrode and graphite as the working electrode. A single layer microporous polypropylene Celgard 2400 with thickness equal 25 μm was used as the separator.

By using an electrode cutter (Hoshen), the anode laminate was punched into circular disks with diameter of 16mm, and dried under vacuum at 120 $^{\circ}\text{C}$ for 12 hours. The separators were punched into circular disks with diameter of 19 mm, and dried under vacuum at 60 $^{\circ}\text{C}$ for 5 hours. After drying, both electrodes and separators were transported into the glove box.

One graphite anode was placed in the lower coin cell part with the active material facing upwards. The separator was applied on top of the graphite electrode, such that both the anode and separator were centered. Afterwards, a gasket was assembled on top of the separator. Further, lithium metal was brushed to remove potential oxidised layer, and punched into a circular disk with diameter of 14 mm, before it was pressed onto a 0.3mm spacer. The separator was wetted with 50 μL electrolyte (1.2 mol/L LiPF_6 in 3:7 wt % ethylene carbonate: ethyl methyl carbonate and 2 wt% vinylene carbonate) before the lithium/spacer- component was placed on top of the separator with the lithium metal facing downwards. Finally, the upper coin cell part was placed on top of the spacer, and the cell was sealed by using a crimper. Figure [3.2](#) shows the components together with the assembly of a coin cell.

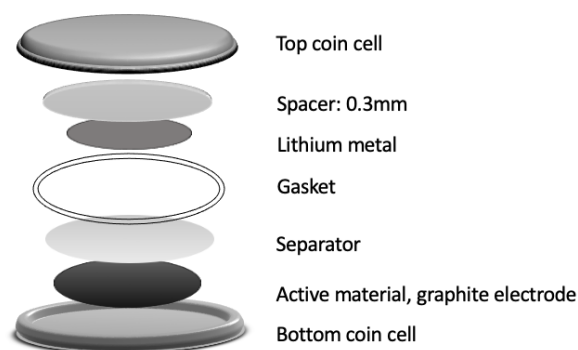


Figure 3.2: Components used in a coin cell and it's assembly [\[19\]](#).

3.4.2 3-electrode cell

The 3- electrode experiments were performed in PAT-cells. These cells had graphite as anode material, LFP as cathode material, and metallic lithium as the reference electrode. All graphite electrodes were calendered to a given geometrical density. To obtain as accurate densities as possible, the electrodes were punched out and then calendered. This was evaluated as a better approach compared to calendering the entire cast, as this often resulted in local differences. The densities of the graphite electrodes varied for the different experiments and are specified in the section for each experiment. Appendix [B.3](#) presents the calculations needed to find the correct electrode thickness to achieve the preferred geometrical density.

As rate-testing in half cells is not possible due to the overpotential from the lithium electrode, LFP is used as the cathode material for the 3-electrode experiments. To ensure fully utilization of the anode, an oversized cathode of 3.5 mAh/cm^2 provided by Customcells was used. The height of this cathode equal $208 \text{ }\mu\text{m}$, which required a height number of 350 for the lower plunger. This ensured that the reference ring was plane with the separator. The insulating sleeve used for these experiments was provided by EL-cell and contained a lithium reference ring and FS-5P separator^[76], which is a two layered separator made of polypropylene.

The LFP- and graphite- laminates was punched into circular disks with diameter of 18 mm by using an electrode cutter provided by El-Cell. The electrodes were dried at $120 \text{ }^\circ\text{C}$ in vacuum for 12 hours before they were transported into the glove box.

One insulating sleeve was taken out from a vacuum-packed bag and placed on the worktop with the smallest side facing upwards. A LFP electrode was placed on top of the separator such that the current collector pointed upwards. The lower plunger was applied on top of the cathode, and the component was placed in the bottom cell base such that the largest side of the insulating sleeve pointed upwards. Furthermore, the separator was wetted with $100 \text{ }\mu\text{L}$ electrolyte before the graphite anode was placed on top of the separator with the current collector facing upwards. The upper plunger was inserted, before the cell was sealed by the upper cell base. The type of electrolyte used in these cells varied, and are specified in the section for the specific experiment.

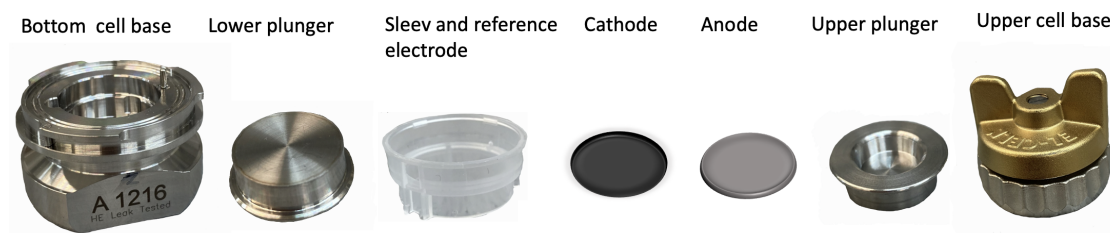


Figure 3.3: The components of a PAT-cell [\[19\]](#).

3.5 Determination of the specific capacity

Although the theoretical capacity of graphite equal 372 mAh/g, the specific capacity varies for different types of graphite powders. The specific capacity of the two powders were found by cycling coin cells at low lithiation- and delithiation- rates equal to $C/30$. Detailed explanation of the cycling program is presented in Appendix [C.1](#). Because the specific capacities of the two powders at this point were unknown, the theoretical value of 372 mAh/g was used to calculate the currents. The calculations used to find the cycling currents are shown in Appendix [B.2](#). This method is general for all currents used in this project. The specific capacities were used to calculate the cycling currents for the rest of the project.

3.6 Slurry optimization

To compare the performance of the two powders, it was preferred to have electrodes with similar capacity. The aimed capacity was 2 mAh/cm². Because the two powders had different specific capacity, the loading needed to obtain this value varied. Appendix [B.2](#) shows the calculations used to find the required loading to obtain 2mAh/cm² based on the specific capacity of the powder. Table [3.2](#) show the different solid/liquid-ratios and gap-sizes tested to reach the target loading. The recipe that gave electrodes with loading closes to the aimed value were used for the rest of the project.

Table 3.5: Slurry optimization of the S48- and S93- powder. The table shows the different solid/liquid-ratios as well as the gaps-sizes that were tested.

Type of powder	$\frac{\text{Solid}}{\text{Liquid}}$ - ratio [%]	Gap-size [μm]
S48	70	150, 180, 200
	72	100, 120, 150, 200
S93	72	120, 150, 180, 200
	75	150, 200

3.7 Formation of 3-electrode cells

Before any electrochemical tests were performed on the PAT-cells, a formation program was started to create the SEI- layer. The following paragraph explains this program.

The LFP electrode was set as the working-electrode, while graphite constitutes as the counter electrode. The formation started with a 5 minutes rest step followed by lithiation at C/20 until the cell potential had reached 1.5V. This step was applied to avoid corrosion of the copper current collector. Afterwards, a 12 hours rest step was applied to ensure good wetting of the electrodes. The graphite electrode was then lithiated at C/30. To avoid plating of the counter electrode, a lower potential limit was set to 5mV at the counter electrode. Additionally, a potential limit equal 4.2V was set at the working electrode, and 4V for the cell potential as safety measures. After lithiation, delithiation at C/30 followed. A safety limit equal 1V was set at the counter electrode, while the upper limit equal 3V for the working electrode, and 2V for the cell potential. The formation was followed by two cycles at C/10, having similar potential limits as described for the C/30 cycle. Appendix [C.2](#) provides detailed information about this program.

3.8 Tortuosity measurements

The tortuosity of electrodes made by the S48- and S93- powders was calculated by using Equation [2.12](#) which is presented in Section [2.8.2](#). Here, the electrode surface area (A), electrode- porosity (ϵ) and thickness (d) were known, while the ionic resistance (R_{ion}) and conductivity of the electrolytes (σ_{ion}) were found by EIS measurements. The experimental procedure was based on the application note "Determination of the through-plane tortuosity of battery electrodes by EIS" written by rhd instruments with GmbH and Co. KGDr. M. Drüscher [\[77\]](#).

This experiment was performed in PAT-cells with two electrolytes having different concentration of tetrabutylammonium hexafluorophosphate Bu_4NPF_6 . Two concentrations were used to validate the choice of using the simplified TLM-model to evaluate the impedance data. Section [3.8.1](#) [3.8.2](#) and [3.8.3](#) presents the experimental procedure for making the electrolytes, cell assembly and EIS-program.

3.8.1 Electrolytes

To measure the tortuosity of the electrodes, intercalation needs to be avoided. Therefore, lithium-free electrolytes were made by mixing ethylene carbonate (EC), dimethyl carbonate (DMC) and Bu_4NPF_6 .

EC was heated at 30 °C until melting. DMC was added to the container, followed by EC, in a 1:1(wt) -ratio. A syringe was used to apply both solutions. To avoid crystallisation of the EC-solution, the syringe was heated to 30 °C. Afterwards, the correct amount of Bu_4NPF_6 was added to obtain concentrations of 0.1 mol/L and 0.01 mol/L. Finally, a magnetic stirrer was used to mix the electrolytes overnight. The calculations used to find the amount of each component are presented in Appendix [B.5](#).

After making the electrolytes, the conductivity of the two solutions were calculated by using Equation [2.15](#). The electrolyte resistance was measured at 25 °C by EIS using the Nova 2.1.5 software. For these measurements a TSC70 cell [78](#) together with PGSTAT 204 with a FRA32M module [79](#) provided by Metrohm Autolab was used. As this is a complex structure, the cell constant could not be found directly as described in Section [2.9.3](#). The cell constant was calculated by using Equation [2.15](#), measuring the electrolyte resistance by EIS for a 0.1M KCl-solution with known conductivity equal 12.87 mS/cm at 25 °C.

For all the impedance measurements, the frequency interval ranged from 100 Hz to 500 kHz with the voltage amplitude equal 10mV. The program had 10 measuring points per decade, and all impedance curves were fitted by the RelaxIS software using the circuit element shown in Figure [3.4](#). Here $R1$ is the electrolyte resistance and $Q1$ is a constant phase element.

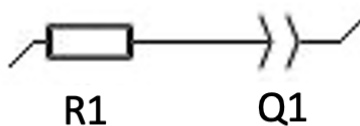


Figure 3.4: Circuit element used to fit the impedance data for the conductivity measurements. The circuit consists of the electrolyte resistance $R1$, and a constant phase element $Q1$.

3.8.2 Symmetric cell assembly

PAT-cell was used as test-cell, in which the basic assembly were similar as explained in Section 3.4.2. However, there were two main differences from this assembly. Firstly, instead of using a 3-electrode cell, a symmetrical two-electrode cell with graphite as both working- and counter- electrode was used. Both electrodes were calendered to a geometrical density of $1.35 \pm 0.02 \text{ g/cm}^3$ which corresponded to a porosity of approximately $38.4 \pm 0.3\%$. The porosity depended on the slurry composition, and the calculations of this is shown in Appendix B.4. The electrode area equal 2.545 cm^2 . The average thickness of the two graphite electrodes in the same cell (excluding the current collector) was used for the tortuosity calculations. These values varied between approximately $53 \text{ }\mu\text{m}$ and $55.5 \text{ }\mu\text{m}$ including the current collector and required a lower plunger with height number equal 200. Secondly, as these measurements did not use a lithium reference electrode, the insulating sleeves used for the PAT-cell assembly described in Section 3.4.2 was not used. Instead, a Celegard 2400 separator with diameter equal 21 mm was placed in a PAT-Core PEEK sleeve provided by EL-cell^[80]. The assembly of the sleeve and the PAT-cell was performed inside a glove box.

3.8.3 Test program: ionic resistance

The ionic resistance (R_{ion}) in the symmetrical cells was found with EIS, using a frequency interval from 10 mHz to 100 kHz. The voltage amplitude was set to 1mV and 20 measuring points per decade were chosen. Based on the application note "Determination of the through-plane tortuosity of battery electrodes by EIS" written by rhd instruments with GmbH and Co. KGDr. M. Drüschler^[77], a transmission- line open element model (TLM) was chosen to fit the experimental data. This model is explained in Section 2.9.2, and the circuit is shown in Figure 3.5.

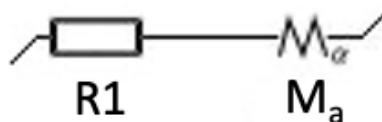


Figure 3.5: Circuit element used to fit the impedance data for the symmetrical cells for the tortuosity measurements. The circuit consists of the electrolyte resistance $R1$, and the simplified transmission line model M_a .

3.9 Fast charge ability of S48- and S93-electrodes

The S48- and S93-powder was further investigated by comparing the fast charge ability of S48- and S93-electrodes in a charge acceptance test. For this experiment PAT-cells were cycled using a potentiostat and assembled as described in Section [3.4.2](#). The LFP electrode was set as the working-electrode, while graphite constitutes as the counter electrode. The anodes were calendered to a geometrical density equal $1.35 \pm 0.02 \text{ g/cm}^3$. The electrolyte used for these experiments was 1.2 mol/L LiPF_6 in 3:7 wt % ethylene carbonate: ethyl methyl carbonate and 2 wt% vinylene carbonate.

3.9.1 Test program: charge acceptance test

After formation of the PAT- cell, a charge acceptance test was performed. This test had lithiation rate starting at C/2 and increased with C/2 steps up to 5C. The delithiation rate was kept constant during the entire test and equal C/2. Each cycle was performed 5 times. In this paragraph, one cycle sequence is described in detailed.

After 1 minute rest, lithiation at C/2 was applied. A safety limit of 4.0 V was set to the cell potential. To avoid overlithiation and hence plating of the graphite electrode a lower limit of 5mV was given at the counter electrode. After lithiation, a delithiation rate of C/2 was applied with an upper potential limit of 2.5V for the cell potential. The upper potential limit was set to 1V for the counter electrode. To ensure full delithiation of the graphite electrode, a rest step of 1 minute followed by a delithiation at C/10 was applied. The same potential limits as for the delithiation at C/2 were used. This sequence was performed 5 times before the lithiation rate increased with C/2, while the delithiation rate was kept constant throughout the test. Detailed explanation of the program is given in Appendix [C.3](#).

After rate-test, the resistance in the two cells were investigated with EIS-measurements. As graphite is most stable at potentials close to 75 mV, lithiation at C/20 with potential limit at 75mV for the graphite electrode was applied after the rate-test, before the EIS-measurement was started. During the measurements LFP was set as the counter electrode and graphite as the working electrode. The frequency interval used for the EIS- program ranged from 1mHz to 200 kHz, having 6 measuring points per decade. The voltage amplitude was set to 5 mV. The results were fitted to a R-Randles-circuit shown in Figure [3.6](#), where W_o is the open-warburg element.

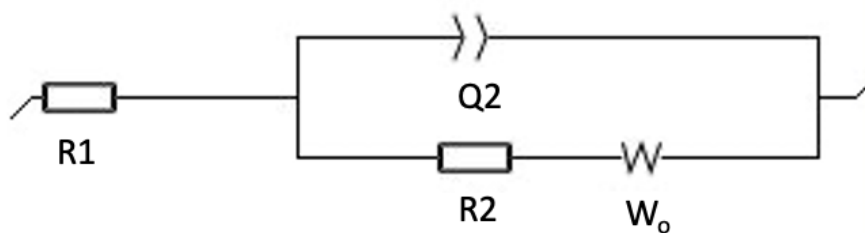


Figure 3.6: Circuit element used to fit the impedance result for a 3-electrode cell. The circuit consists of electrolyte resistance $R1$, constant phase element Q , charge transfer resistance $R2$ and Warburg open element W_o .

3.9.2 Postmortem characterization of cycled electrodes

To investigate whether the electrodes had suffered from lithium plating after the charge acceptance test, SEM micrographs of the graphite surface were taken. After the EIS-measurement, the cell was delithiated at $C/20$ with a potential limit of 1V for the graphite electrode before the cell was disassembled inside the glove box. The graphite electrode was washed with DMC and dried for 30 minutes before it was transported to the SEM instrument. During this transport the electrode was exposed to air. The electrode surfaces were imaged by using Zeiss-Supra 55VP with secondary electrons and an accelerating voltage equal 10 kV. The SEM micrographs of the cycled electrodes were compared to SEM micrographs of uncycled electrodes, which were taken with the same instrumental setup.

3.10 Porosity graded electrodes

The following sections describes the manufacturing, characterization, and measurements performed on porosity graded electrodes.

3.10.1 Manufacturing

Based on the result from the charge acceptance test and the tortuosity measurements, the powder showing the best performance was used to make double layered electrodes. The anode laminate had a bottom layer with geometrical density equal $1.45 \pm 0.02 \text{ g/cm}^3$ and a top layer with density of $1.25 \pm 0.02 \text{ g/cm}^3$. The bottom layer was tape casted similar as described in Section [3.3](#). After drying the laminate at $60 \text{ }^\circ\text{C}$ for 3 hours, the geometrical density of $1.45 \pm 0.02 \text{ g/cm}^3$ was achieved by calendered the entire cast to the preferred thickness, which was found by the calculations shown in Appendix [B.3](#). The loading used to calculate this thickness was found by making an additional anode laminate with the

same slurry and gap-size. From this cast, electrodes were punched out and the loading of these were used to calculate the thickness. Unfortunately, the calendering resulted in an uneven and wavy-like structure of the laminate, which made it challenging to tape cast the top layer. As an attempt to improve this, Cu-foils with different thicknesses of 18mm, 13 mm and 12 mm were tested, in which the thinnest foil also had better mechanical properties. Additionally, the laminate was pressed between two glass plates for 12 hours, before the top layer was applied. During pressing, the container with slurry that should be used to cast the top layer was sealed. Before applying the second layer, mixing at 500 rpm for 5 minutes in addition to an ultrasound bath was used to remove gas bubbles that had been formed in the slurry during the storage period.

The bottom layer was tape casted by using a fixed gap applicator with a width equal 9 cm, while the top layer was made by using a fixed gap applicator with a width equal 7 cm. This was to ensure a uniform distribution of the slurry. The first attempts of making the double layered electrode were performed with a gap-size equal 100 μm for both bottom- and top- layer. To reduce the loading, experiments using 50 μm in gap-size for both layers were tested.

After the second layer were tape casted, the anode laminate were dried at 60 $^{\circ}\text{C}$ for 12 hours before electrodes were punched out and pressed to the density of $1.25 \pm 0.02 \text{ g/cm}^3$ for the top layer. As calendering these electrodes resulted in the top layer peeling off, a uni-axial press was used instead. The same approach as previously described were used to calculate the thickness needed to achieve a top layer with density of $1.25 \pm 0.02 \text{ g/cm}^3$. Here, the loading of the specific electrode was used. Because the loading of the electrode was given for both layers, the average density of $1.35 \pm 0.02 \text{ g/cm}^3$ were set as the desired geometrical density. This approach assumed that the loading of the bottom- and top- layer was equal. Moreover, it was assumed that only the top layer would be affected by the pressing, and that the thickness of the bottom layer was kept unchanged. An illustration of the double layered anode laminate is shown in Figure [3.7](#).

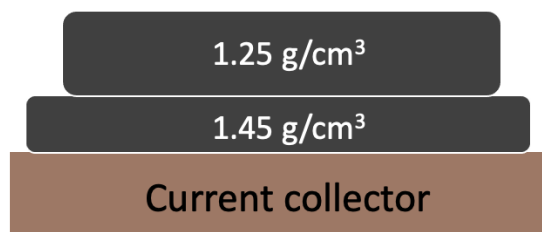


Figure 3.7: Illustration of a doubled layered electrode having a dense bottom layer and a more porous top layer.

3.10.2 Fast charge ability of porosity graded electrodes

The fast charge ability of the double layered electrode was compared to a single layer electrode in a charge acceptance test. To obtain the best basis for comparison, the loading of the single electrode was optimized such that it became close to the loading of the double layer electrode. The single layered electrode was made by using a solid/liquid-ratio of 72 % and gap size equal 200 μm . Additionally, the single electrode was calendered to a geometrical density of $1.35 \pm 0.02 \text{ g/cm}^3$, which corresponded to the average density of the double layer electrode. The electrodes were tested in PAT-cell and assembled similar as described in Section [3.4.2](#). The same rate-test program as described in Section [3.9.1](#) were used, with one change regarding the delithiation conditions.

It was observed that the potential of the LFP electrode dropped faster during delithiation than what was observed in the previous rate-tests. Consequently, the delithiation of graphite stopped at potential close to 0.3V instead of 1V. To avoid this, the delithiation was changed to C/5 with upper limit of 2 V for the cell potential and 1V for the graphite electrode. This was followed by a 1 minute rest step before delithiation at C/50 was applied, having the same potential limitations as for the C/5 delithiation.

To obtain an indication of the degradation of the cells, EIS was performed before and after the charge acceptance test for both cells. The same program as described in Section [2.9.2](#) was used. The graphite electrode was lithiated at C/20 to a stable potential equal 75mV before both EIS-measurements. To obtain a fully delithiated graphite electrode when the charge acceptance test started, the cell was delithiated at C/20 with a potential limit of 1V for the graphite electrode after the first EIS measurement.

3.10.3 Cross section characterization

The densities of the double- and single- layered electrodes were compared by taking SEM cross-section micrographs. The cross sections were generated by an argon beam mill at SINTEF Industry. The SEM micrographs taken by using Zeiss-Supra 55VP with secondary electrons and an accelerating voltage equal 10kV.

4 Results

4.1 Powder characterization

The morphology of the two powders was characterized with SEM micrographs and by measuring the BET surface area and PSD. The obtained BET surface area values are tabulated in Table 4.1 and were quite similar. The S48- powder had a slightly lower value equal $1.0210 \text{ m}^2/\text{g}$, compared to $1.2916 \text{ m}^2/\text{g}$ for the S93- powder.

Table 4.1: BET surface area of the S48- and S93- powder.

Powder	BET surface area [m^2/g]
S48	1.0210
S93	1.2916

In addition to BET- analysis, the PSD of the powders was measured by laser diffraction. The fraction as a function of particle diameter is presented in Figure 4.1 for both powders. As can be seen, the particle size was a bit larger for the S93- powder with d_{50} equal $11.72 \mu\text{m}$, compared to $9.75 \mu\text{m}$ for the S48- powder. Additionally, the S48- powder had a more narrow distribution compared to the S93-powder. This can be seen as the highest fraction equal 15.6% for the S48- powder, while it was 14.8% for the S93- powder.

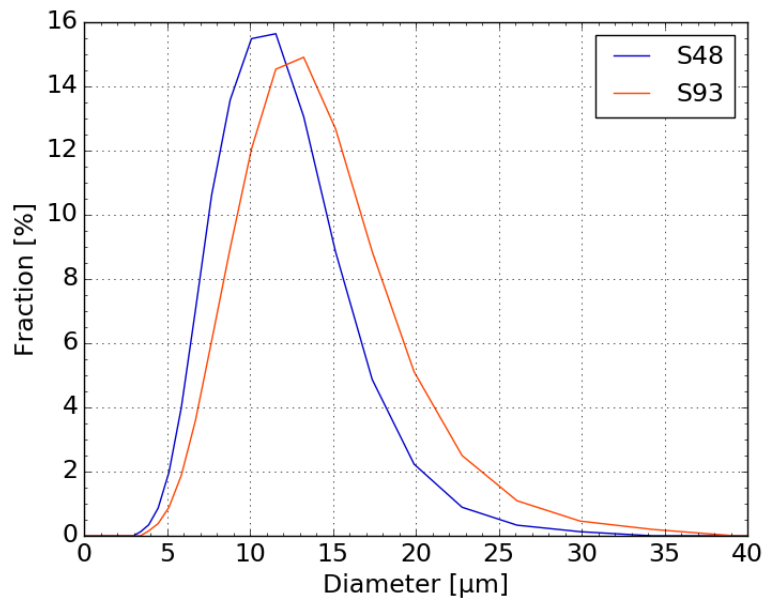


Figure 4.1: Particle size distribution of the S48- and S93- powder. The figure shows the fraction in % as a function of particle diameter, when assuming all particles to be spheres.

The morphology of the two powders was further investigated by SEM. The resulting SEM micrographs are presented in Figure 4.2. Here, Figure 4.2a and 4.2c represent the S48- powder, while Figure 4.2b and 4.2d show the S93-powder. The micrographs show a relative homogeneous particle size distribution, which is in correlation to the results obtained from laser diffraction shown in Figure 4.1. However, there are some differences between the two powders. More agglomerates were observed for the S93-powder compared to the S48-powder. A visual of this difference is shown in Figure 4.2c and 4.2d. The agglomerates consist of multiple small particles in which their edges are oriented in different directions. Additionally, the S48-particles seem to align better to the surface, compared to the S93-particles in which the edges of the particles seem to stick more up from the surface.

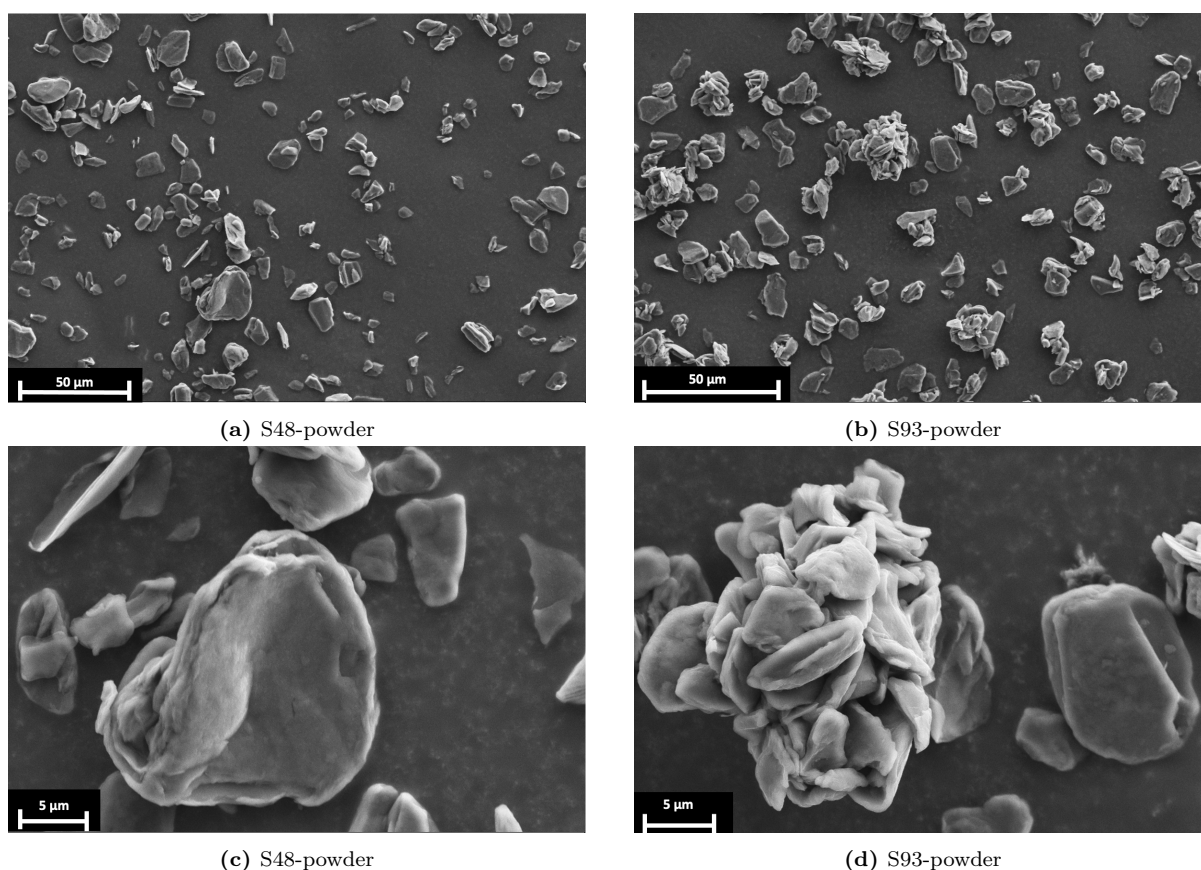


Figure 4.2: SEM micrographs of the S48- and S93- powders. Figure a and c represents the S48- powder, while figure b and d are the S93-powder.

4.2 Slurry optimization and manufacturing of anode laminates

To obtain the best basis for comparison of the S93- and S48- electrodes, it was preferred that they had the same capacity equal 2 mAh/cm^2 . This was achieved by optimizing the slurry recipes. The results from this process are presented in Section [4.2.1](#) and [4.2.2](#). These results were further used to manufacture the porosity graded electrodes, in which the results from this process are presented in Section [4.2.3](#).

4.2.1 Determination of the specific capacity

The specific capacity of the powders was found by cycling coin cells at C/30 having graphite and lithium metal as working- and counter- electrode respectively. Figure [4.3](#) shows the cell potential vs. Li/Li^+ as a function of capacity for both powders during the first two cycles. From Figure [4.3a](#) and [4.3b](#) the specific capacity of the S48- and S93- powder were found to be 352 mAh/g and 325 mAh/g respectively.

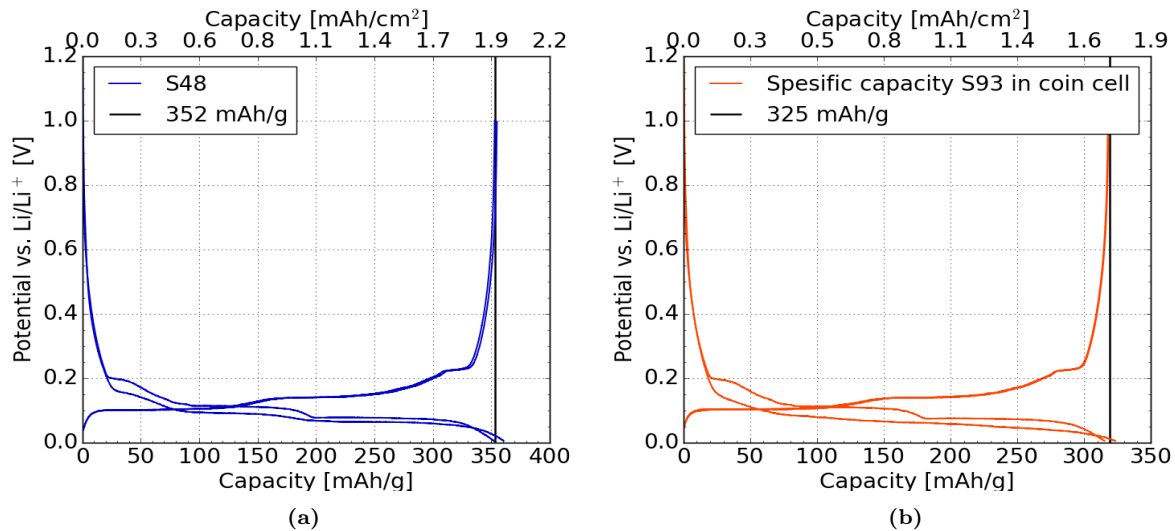


Figure 4.3: Cell potential vs. Li/Li^+ as a function of capacity for the S48- and S93-powder. The measurements are performed in coin cells having graphite and lithium metal as the working- and counter- electrode respectively. The theoretical capacity of graphite equal 372 mAh/g were used to calculate the cycling current of C/30.

4.2.2 Processing parameters

The specific capacities were used to calculate the loading needed to obtain electrodes with capacities of approximately 2 mAh/cm^2 . As the powders had different specific capacities, the targeted loading of the electrodes needed to reach 2 mAh/cm^2 also varied. The resulting targeted loadings equal 5.68 mg/cm^2 and 6.15 mg/cm^2 for S48- and S93- electrodes respectively and was calculated as show in Appendix [B.2](#). To obtain electrodes

with these loadings, different solid/liquid-ratios and gap-sizes were tested. These parameters together with the corresponding loading are presented in Table 4.2 and 4.3 for the S48- and S93- powder respectively. The average loading was based on five electrodes from each cast and was calculated as described in Appendix B.2. As expected, the loading increased with increasing gap-size and solid/liquid- ratio. Furthermore, it was observed that the standard deviation was higher for slurries with lower solid/liquid-ratio, with one exception for the S48- powder having solid/liquid-ratio equal 72 % and gap size equal 200 μm .

The recipes that gave electrodes with loading close to the targeted loading of 5.68 mg/cm^2 and 6.15 mg/cm^2 for S48 and S93 respectively were chosen. This resulted in a solid/liquid ratio of 70 % and gap-size of 150 μm for the S48- powder, while a solid/liquid ratio of 72 % and gap-size of 150 μm were used for the S93- powder. These recipes are highlighted in Table 4.2 and 4.3. The electrodes used to measure the tortuosity and evaluated the fast charge ability of the S48- and S93 powders were manufactured by using these recipes.

Table 4.2: Slurry optimization with the S48- powder. The table presents the different solid/liquid-ratios and gap-sizes tested, with the resulting average electrode loading. The recipe chosen for further experiments are highlighted in blue.

$\frac{\text{Solid}}{\text{Liquid}}$ - ratio [%]	Gap size [μm]	Average loading [$\frac{\text{mg}}{\text{cm}^2}$]
70	150	5.72 \pm 0.22
70	200	7.16 \pm 0.43
72	100	4.70 \pm 0.08
72	150	6.64 \pm 0.10
72	200	8.81 \pm 0.49

Table 4.3: Slurry optimization with the S93- powder. The table presents the different solid/liquid-ratios and gap-sizes tested, with the resulting average electrode loading. The recipe chosen for further experiments are highlighted in red.

$\frac{\text{Solid}}{\text{Liquid}}$ - ratio [%]	Gap size [μm]	Average loading [$\frac{\text{mg}}{\text{cm}^2}$]
72	50	2.03 \pm 0.28
72	100	4.26 \pm 0.21
72	150	5.81 \pm 0.25
72	200	7.59 \pm 0.27
75	150	7.14 \pm 0.18
75	200	9.67 \pm 0.11

4.2.3 Manufacturing of porosity graded electrodes

For the manufacturing of double-layer electrodes, the S93-powder was used with the same solid/liquid-ratio as was found in Section 4.2.2. However different gap-sizes of the fixed gap applicator were tested for these electrodes. The manufacturing of the double layer electrodes was challenging, and multiple types of current collectors and calendaring techniques were tested. This section presents the results obtained from the different manufacturing techniques.

The biggest challenge was to obtain a smooth and even laminate after calendaring the bottom layer to a geometrical density of 1.45 g/cm^3 . The Cu-foil tend to crease and caused a wavy structure of the anode laminate. To avoid this, different Cu-foils with thicknesses of $18 \text{ }\mu\text{m}$, $13 \text{ }\mu\text{m}$ and $12 \text{ }\mu\text{m}$ were tested. The results can be seen in Figure 4.4, in which the thickest and the thinnest foil is presented from the left to the right. As the pictures show, the thickest foil suffered most from deformation which became especially visible at the interface of the slurry and the Cu-foil. By changing to a thinner Cu-foil, the anode laminate became easier to handle in the calendar, which gave less deformation of the foil, hence also a more even anode laminate. This can be seen as the deformation decreases with decreasing thickness of the Cu-foil. The result became substantially better for the thinnest Cu-foil, as this foil also had better mechanical properties compared to the two others. For this reason, the thinnest foil of $12 \text{ }\mu\text{m}$ was used for further manufacturing.

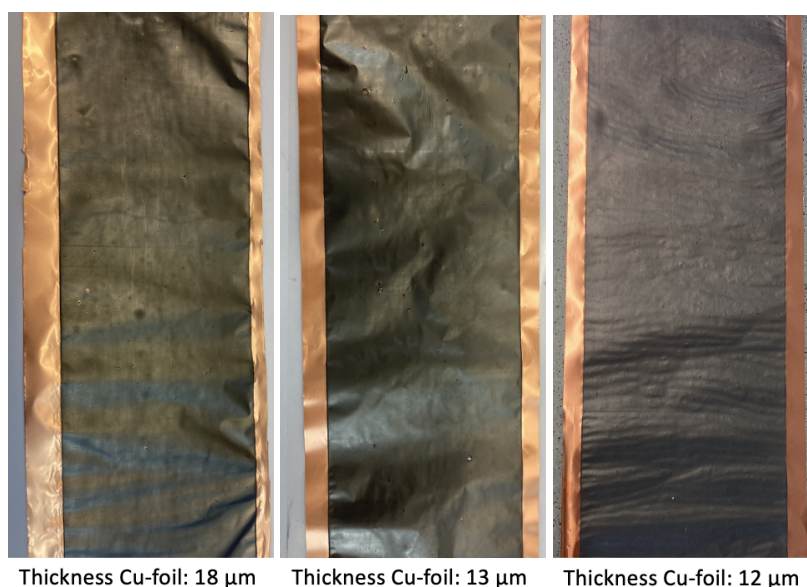


Figure 4.4: Bottom layer after calendaring with three different Cu-foils. The Cu-foil thicknesses tested were $18 \text{ }\mu\text{m}$, $13 \text{ }\mu\text{m}$ and $12 \text{ }\mu\text{m}$ going from the left to right in the figure respectively.

However, as can be seen from the pictures, smaller waves were observed at the surface of the anode laminate using the thinnest Cu-foil after calendaring. As an attempt to reduce this, the foil was pressed between two glass plates overnight. Figure 4.5 shows pictures of the anode laminate before (to the left) and after (to the right) pressing. As can be seen, the small waves have been smoothed out to a more uniform surface, giving a more even laminate. Therefore, it was concluded that pressing was needed before applying the second layer. Unfortunately, there was still some structure observed at the surface which was impossible to remove. Consequently, the laminate was a bit curved when applying the top layer.

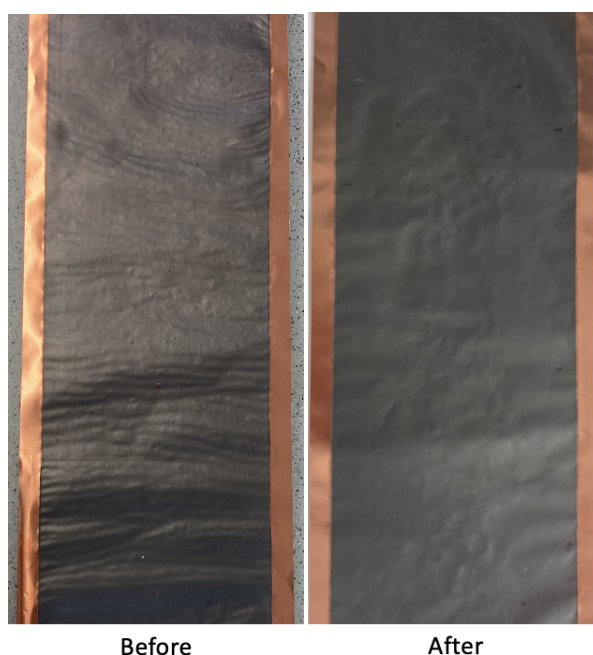


Figure 4.5: Anode laminate before and after pressing for the left and right image respectively. The laminate had Cu-foil with thickness equal $12\ \mu\text{m}$.

Since the anode laminate was uneven, an attempt of smooth it out by sticking it to the bottom of the tape-caster with ethanol was tried. Although the laminate became even smoother, it was unavoidable to have some part of the laminate sticking up from the tape-caster. Consequently, only some parts of the laminate were fully covered with the top layer. Therefore, another attempt of tape casting the top layer were performed without sticking the anode laminate to the tape-caster. This enabled the cast to adjust to the high of the fixed gap applicator during casting. This technique resulted in a fully covered second layer and was therefore the technique used for further manufacturing. The two cases can be seen in Figure 4.6, showing the result with- and without- the use of ethanol for the left and right pictures respectively.

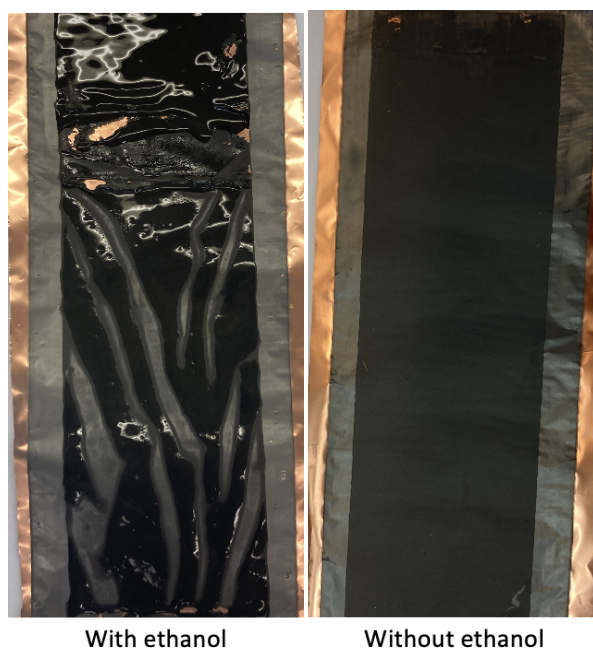


Figure 4.6: Anode laminate after applying the top layer. The pictures show the difference of using and not using ethanol to stick the laminate to the bottom of the tape caster. The left picture shows the case in which ethanol was used, while the right image shows the case in which the laminate was not stuck to the tape caster.

The double layer cast was first created by using a fixed gap applicator with gap-size equal $100\ \mu\text{m}$ for both layers. This resulted in an average capacity of $4.75 \pm 0.25\ \text{mAh}/\text{cm}^2$. As an oversized LFP cathode with capacity of $3.5\ \text{mAh}/\text{cm}^2$ was used for these experiments, the capacity of these anodes was too high. To reduce the loading, a fixed gap applicator with gap-size equal $50\ \mu\text{m}$ was used to cast the two layers. This resulted in an average capacity equal $2.45 \pm 0.16\ \text{mAh}/\text{cm}^2$. Because this gave anodes with lower capacity than the cathodes, this procedure was used for the further manufacturing of the double layered electrodes. The average loading and capacity with standard deviation for the two cases are presented in Table [4.4](#).

Table 4.4: The loading and theoretical capacity of double layer electrodes made by a fixed gap applicator with gap-size equal $50\ \mu\text{m}$ and $100\ \mu\text{m}$.

Gap-size μm	Loading $[\text{mg}/\text{cm}^2]$	Theoretical capacity $[\text{mAh}/\text{cm}^2]$
50	7.54 ± 0.48	2.45 ± 0.16
100	14.62 ± 0.77	4.75 ± 0.25

It was observed that the standard deviations of the double layer electrodes were higher

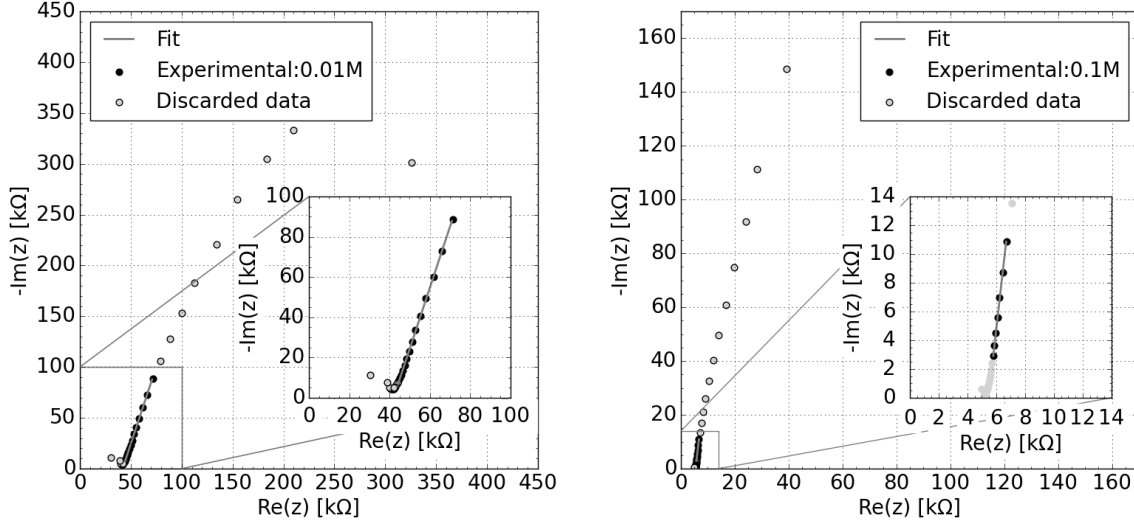
compared to the single layer electrodes made during the slurry optimization for the S93-powder which can be seen in Table 4.3. Moreover, the loading of the double layer electrodes made by applying two layers of 50 μm was higher compared to the loading of a single layer electrode made with a gap-size of 100 μm of the same powder(S93) from Table 4.3. This can be seen as the double layered electrode had an average loading equal $7.54 \pm 0.48 \text{ mg/cm}^2$ while the single layered electrode had $4.26 \pm 0.21 \text{ mg/cm}^2$. The same observation was made for the double layer electrodes made with a 100 μm gap-size compared to a single layer electrode made with a gap-size equal 200 μm .

4.3 Tortuosity measurement: comparing S48- and S93- electrodes

The results from the tortuosity measurements on S48- and S93- electrodes are presented in the following sections.

4.3.1 Ionic conductivity measurements

To determine the ionic conductivity of the electrolytes used in the tortuosity measurements, the cell constant was found by measuring the electrolyte resistance by EIS of a 0.1M KCl- solution with a known conductivity of 12.87 mS/cm at 25 °C. The Nyquist plot together with the obtained values of the circuit parameters are presented in Appendix [D.2.1](#) and gave a cell constant equal $16.22 \pm 0.24 \text{ cm}^{-1}$. Afterwards, the conductivity of the electrolytes was calculated with EIS- measurements. The results are presented as Nyquist plots in Figure [4.7](#) for the two electrolytes. The EIS data were fitted with RelaxIS to the circuit shown in Figure [3.4](#). The fitted values are presented in Appendix [D.2.2](#), Table [D.2](#). The choice of circuit was based on the application note "Fundamental Calculation of Cell Constants using the Autolab Microcell HCTSC70 and TSC1600" published by Metrohm Autolab [\[70\]](#). As can be seen, the experimental data deviated from a linear trend at low frequencies. Because the goal was to find the resistance of the electrolytes, only the linear region at high frequency was evaluated. In this region the impedance of the constant phase element becomes close to zero which can be seen from the equation presented in Table [2.1](#). Therefore, the dominating circuit element in the high frequency region was the electrolyte resistance [\[81\]](#). It was observed that the KCl- solution gave a more linear trend compared to the two electrolytes for a wider frequency interval. Consequently, a larger number of the experimental data points were evaluated for the KCl- solution.

(a) Electrolyte: 0.01M Bu_4NPF_6 in 1:1 wt% EC:DMC.(b) Electrolyte: 0.1M Bu_4NPF_6 in 1:1 wt% EC:DMC.**Figure 4.7:** Nyquist plot for the EIS-measurements of the electrolytes used to calculate the ionic conductivity.

The resistance values (R) for the two electrolytes equal $42.013 \pm 0.168 \text{ k}\Omega$ and $5.460 \pm 0.013 \text{ k}\Omega$ for 0.01M and 0.1M respectively. By using these values together with the cell constant equal $16.22 \pm 0.24 \text{ cm}^{-1}$, Equation 2.15 was used to calculate the conductivity of the electrolytes. This gave $0.386 \pm 0.006 \text{ mS/cm}$ and $2.971 \pm 0.045 \text{ mS/cm}$ for the 0.01M and 0.1M electrolyte respectively as shown in Table 4.5. As expected, the electrolyte having the lowest concentration of Bu_4NPF_6 also had the lowest conductivity. The 0.01M electrolyte had almost ten times lower conductivity compared to the 0.1M electrolyte.

Table 4.5: The conductivity of the two electrolytes used in the tortuosity measurements.

$C_{\text{electrolyte}} [\text{mol/L}]$	$\sigma_{\text{dc}}(25 \text{ }^\circ\text{C}) [\text{mS/cm}]$
0.01	0.386 ± 0.006
0.1	2.971 ± 0.045

4.3.2 Symmetrical cell impedance

After calculating the ionic conductivity of the electrolytes, the ionic resistance in the symmetrical two-electrode cells was found by EIS- measurements. For these measurements it was desired to have approximately equal loading of the electrodes in the same cell. The targeted loading presented in Section 4.2 were used. However, because of a large

deviation in loading, it was evaluated as most important to have electrodes with equal loading within the same cell more than being close to the targeted loading. The resulting loading, theoretical capacity, geometrical density, and thickness (excluding the thickness of the current collector) of the electrodes are presented in Table 4.6. The calculation of the theoretical capacity was based on the specific capacity of each powder.

Table 4.6: The loading, theoretical capacity, geometrical density and thickness of the electrodes used in the symmetrical two-electrode cells.

Powder	Electrolyte	Loading [mg/cm ²]	Theoretical capacity [mAh/cm ²]	Geometrical density [g/cm ³]	Average thickness [μ m]
S48	0.01	5.57 and 5.55	1.96 and 1.95	1.36 and 1.35	41.0350 \pm 0.0002
	0.1	5.69 and 5.64	2.00 and 1.99	1.36 and 1.35	41.8500 \pm 0.0001
S93	0.01	5.90 and 5.92	1.92 and 1.93	1.36 and 1.35	43.5202 \pm 0.0005
	0.1	5.75 and 5.79	1.88 and 1.88	1.35 and 1.36	42.6250 \pm 0.0001

The results from the EIS-measurements are presented as Nyquist plots in Figure 4.9, in which the blue graphs represent the S48-powder, and the red graphs show the S93-powder. To obtain the exact values for the ionic resistance, the experimental data were fitted to the simplified transmission line model shown in Section 2.9.2. The fitted parameters are shown in Appendix D.2.3 Table D.3. For the S48-cells the ionic resistance equal 113.0 \pm 0.98 Ω and 16.18 \pm 0.93 Ω for 0.01M and 0.1 M electrolytes respectively. The ionic resistance of the S93-cells were measured to be 69.54 \pm 0.99 Ω and 11.14 \pm 0.99 Ω for the 0.01M and 0.1 M electrolyte respectively.

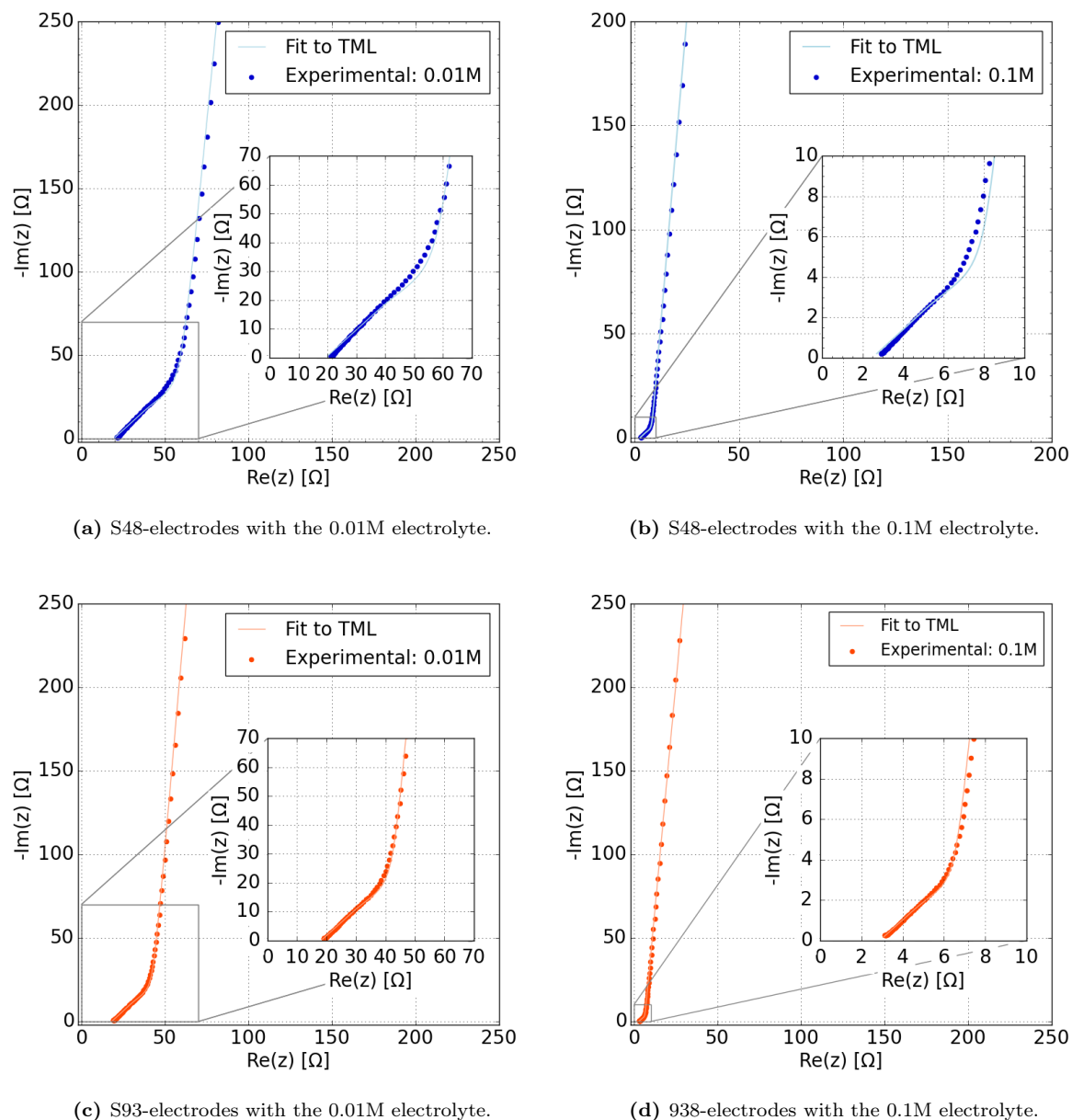


Figure 4.9: Nyquist plot for the EIS-measurements of symmetrical cell having graphite as counter- and working- electrode with electrolytes having 0.01M and 0.1M of Bu_4NPF_6 in 1:1 wt% EC:DMC.

By using the conductivity of the electrolytes and the ionic resistance in the cell, the tortuosity of the electrodes was calculated with Equation 2.12 for both powders with the two electrolytes. The average thickness of the two graphite electrodes in the same cell was used for the calculations. These values are presented in Table 4.6 for each cell. Based on the true electrode density which was calculated from the slurry composition as shown in Appendix B.4, the average porosity of $38.4 \pm 0.3\%$ were used for all four cells. Furthermore, the electrode area equal 2.545 cm^2 . The resulting tortuosity values are presented

in Table 4.7. It was observed that the S48- electrodes had the highest tortuosity with 5.20 ± 0.1 and 5.61 ± 0.35 for the 0.01M and 0.1 M electrolytes respectively. Moreover, the S93- electrodes had tortuosity of 3.01 ± 0.07 and 3.79 ± 0.36 for 0.01M and 0.1M electrolytes respectively. Additionally, it appears that the highest tortuosity was given for the cells having the electrolyte with the highest conductivity.

Table 4.7: The resulting tortuosity values of S48- and S93- electrodes using two electrolytes with different conductivity.

Powder	$C_{\text{electrolyte}}$ [mol/L]	τ [-]
s48	0.01	5.20 ± 0.10
	0.10	5.61 ± 0.35
s93	0.01	3.01 ± 0.07
	0.10	3.79 ± 0.36

4.4 Evaluation of the fast charge ability of S48- and S93-electrodes

The fast charge capability of the two powders was evaluated in a charge acceptance test with charging rates from $C/2$ to $5C$. Similar as for the tortuosity measurements, the targeted loading of 5.68 mg/cm^2 and 6.15 mg/cm^2 for the S48- and S93- powder respectively were used. The resulting loading, theoretical capacity, thickness, and geometrical density are presented in Table 4.8. The theoretical capacities are based on the specific capacity of the powders found in Section 4.2. The table shows a slightly higher theoretical capacity of the S48-electrode compared to the S93-electrode.

Table 4.8: The loading, theoretical capacity, thickness, and geometrical density of the graphite electrodes used in the charge acceptance test.

Powder	Loading [mg/cm^2]	Theoretical capacity [mAh/cm^2]	Thickness [μm]	Geometrical density [g/cm^3]
S48	5.57	1.96	41.4	1.35
S93	5.84	1.90	43.4	1.35

The cell potential and the potential of the counter- and working- electrode as a function of time is presented in Figure 4.11. The figure presents the two first cycles in the charge acceptance test with charge- and discharge- rate equal $C/2$. This gives the correlation between the three potentials, and constitutes the bases for the three-electrode experiments that is presented in the coming sections. The data was obtained from the S93-cell, and similar tendency was observed for the S48-cell. The entire voltage profile during the charge acceptance test is presented in Appendix C.3 Figure C.3 for the S93-cell.

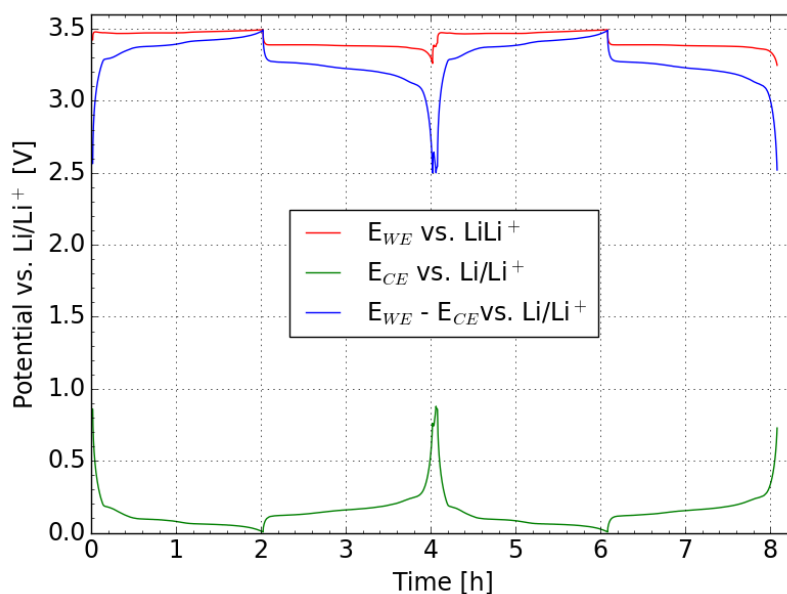


Figure 4.11: The cell potential and the potential of the working- and counter- electrode as a function of time. The figure shows the two first cycles at charge- and discharge- rate equal $C/2$ for the charge acceptance test. The data is obtained from the S93 cell having graphite as counter electrode, oversized LFP as working electrode and lithium metal as the reference electrode. The cycling currents is based on the graphite electrode, using the specific capacity of the S93-powder.

Before the fast charge ability of the S48- and S93- cell was investigated, both cells were cycled with a formation program as explained in Section 3.7. From this, a maximum capacity of 342 mAh/g and 347 mAh/g were reached for the S48- and S93- cell respectively for the first delithiation curve at $C/30$. The potential of the graphite electrode vs. Li/Li^+ as a function of capacity for this cycle is shown in Appendix D.1 Figure D.1 for both cells. It was observed that the maximum capacity obtained from the first formation cycle of the S93- cell was higher than the specific capacity of the S93- powder obtained from coin cell shown in Figure 4.3b. The opposite trend was observed for the S48- cell, as the specific capacity of the S48- powder was measured to be 352 mAh/g as can be seen in Figure 4.3a.

The results from the charge acceptance test are presented in Figure 4.12, which shows the capacity as a function of cycle number for the S48- and S93- cell. The lithiation rates going from $C/2$ to $5C$ are also indicated in the figure. As can be seen, the S93- cell showed better rate- performance compared to the S48-cell as it reached higher maximum capacity and had smaller capacity drops when increasing the lithiation rate. The maximum reached capacity of the S93-cell equal 325 mAh/g while it was 311 mAh/g for S48-cell when cycling at $C/2$. Compared to the maximum capacity from the first delithiation curve

during formation, this corresponds to a SOC equal 93.7 % and 90.9 % for the S93- and S48- cell respectively. Both cells enabled to reach approximately the same capacity for the five first- and five last- cycles at C/2.

In terms of obtainable capacity, the S93- cell showed the best results at the three first C-rates. Afterwards the capacities became almost identical for both cells. When increasing the lithiation rate from C/2 to 1C, the capacity of the S48-cell decreased with 20.6 % which was higher compared to 13.9% for the S93-cell. Further increase in lithiation rate gave an almost equal capacity fade for the two cells. This can be seen as the capacity fades equal 25.5 % and 26.0 % for the S93- and S48- cell respectively when increasing from 1C to 1.5C. The increase from 1.5C to 2C gave the largest capacity drop for the S93- cell equal 33.3 %. The same increase in lithiation rate resulted in a capacity drop equal 29.1 % for the S48- cell.

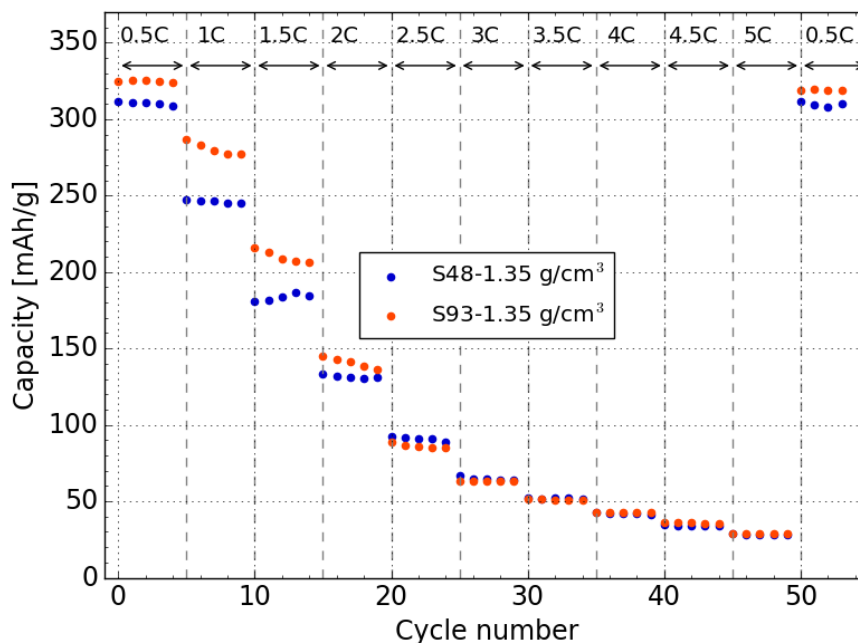


Figure 4.12: Capacity as a function of cycle number for the S48- and S93- cells. The figure includes the different lithiation rates from C/2 to 5C, with a constant delithiation rate equal C/2. The currents are based on the loading of the graphite electrode and the specific capacity of the graphite powders. The cells had graphite as counter electrode, oversized LFP as working electrode and lithium metal as the reference electrode.

Based on the results shown in Figure 4.12 the S93- cell had the best performance. This was further confirmed by studying Figure 4.13 which presents the potential of the graphite electrode vs. Li/Li^+ as a function of capacity for the five cycles at lithiation rates of C/2 and 1C. To increase the readability, these potential curves were plotted between 0V and

0.5V, however it has to be noted that the anode end potential upon discharge reached ca 0.9V.

As can be seen from the figure, the S48- cell shows more polarisation which makes the voltage plateaus less pronounced compared to the S93-cell at lithiation rates of $C/2$ and $1C$.

From Figure 4.12 it was observed that the S93-cell reached a higher SOC compared to the S48- cell, which indicates that the S93-cell was more lithiated. This can further be confirmed by studying the potential curves at $1C$. Here, the first plateau in the delithiation curve is longer for the S93-cell, which indicated a higher lithiation of this cell.

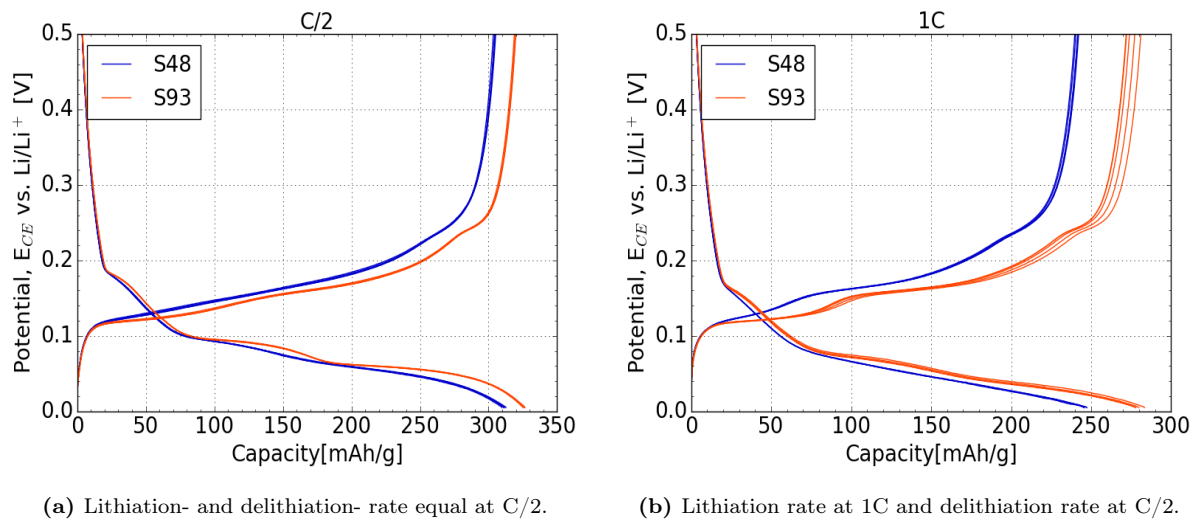


Figure 4.13: The potential of the graphite electrode vs. Li/Li^+ as a function of capacity at lithiation rates of $C/2$ and $1C$, and a constant delithiation rate equal $C/2$.

To obtain an understanding of the resistance in the cells, EIS-measurements were performed after the charge acceptance test for both cells. The experimental data together with the fitted curves are presented in Figure 4.14. RelaxIS with the Randles circuit shown in Figure 3.6 was used to evaluate the impedance data. The fitted parameters are presented in Appendix D.3 Table D.4. As can be seen from Figure 4.14 the fitted data corresponds well with the experimental data.

The impedance results are in correlation with the results obtained from Figure 4.12 and 4.13 as the S93- cell had lower resistance compared to the S48- cell. From the article "Modeling and Applications of Electrochemical Impedance Spectroscopy (EIS) for Lithium-ion Batteries" written by Woosung Choi et. al. [66], R_1 is usually evaluated as the resistance of the electrolyte, while the charge transfer resistance is given by R_2 . From the values presented in Table D.4 the electrolyte resistance of the two cells were simi-

lar to each other and equals $4.52 \pm 0.05\Omega$ and $4.48 \pm 0.02\Omega$ for the S48- and S93- cell respectively. A larger difference was however observed for the charge transfer resistance in which the S48-cell had $7.39 \pm 0.12\Omega$ while it was $5.90 \pm 0.09\Omega$ for the S93-cell. This indicates that more energy was required to transfer charge in the S48-cell, which can contribute to a lower rate performance for this cell.

For the diffusion, the finite open Warburg element was chosen for this setup. The reason for this choice was based on article "Electrochemical Impedance and its Applications in Energy-Storage Systems" written by Deyang Qu et al. [\[51\]](#). They argue that this element gives a better description of battery electrodes compared to the infinite Warburg element as explained in theory Section [\[2.9.2\]](#). However, the Warburg model have assumptions that is not fulfilled for porous electrodes [\[67\]](#). To mention some of them, the model assumes a planar symmetry, and that the diffusion follows Fick's second law which assumes a homogeneous diffusion of lithium ions [\[67\]](#). Therefore, the exact diffusion coefficient can't be obtained from the Warburg element. Further discussion of this model and factors influencing the diffusion of lithium ions is given in Section [\[5.1.2\]](#).

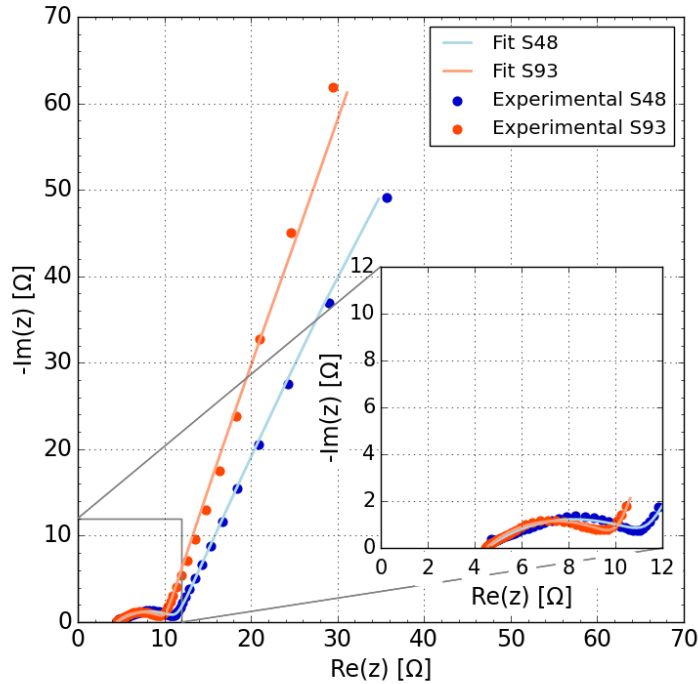


Figure 4.14: Nyquist plot from EIS measurements after the charge acceptance test for two cells having the S48- and S93- powders as the graphite anodes.

4.4.1 Postmortem characterisation of cycled electrodes

Post-mortem characterization of the electrode surfaces was performed after the charge acceptance test by SEM. The goal was to investigate if any degradation in terms of lithium plating had occurred. As described in Section 2.7.3 lithium is hard to detect. To easier detect possible degradation, the cycled electrodes were compared to uncycled electrodes. Figure 4.15a and 4.15b corresponds to uncycled S48- and S93- electrodes respectively, while Figure 4.15c and 4.15d shows cycled S48- and S93- electrodes respectively. Both the edges and the center of the electrodes were inspected. The pictures are a representative micrographs of the four cases.

In the micrographs of the uncycled electrodes, it appears that the S48- particles had a more flat structures compared to the S93- particles which seems to be a bit rounder. This can be seen as the S48- particles align better in a layer-by-layer structure compared to the S93- powder. However, this difference was not substantial.

By comparing the uncycled and cycled electrodes, no changes were observed. The investigation of lithium plating was based on the article "Stable Li Metal Anodes via Regulating Lithium Plating/Stripping in Vertically Aligned Microchannels" written by S.H. Wang et.al. [55], which imaged plated lithium metal as a worm-like structure. However, no such structure was observed for any of the samples. Based on this, none of the electrodes seemed to have suffered from lithium plating during the charge acceptance test.

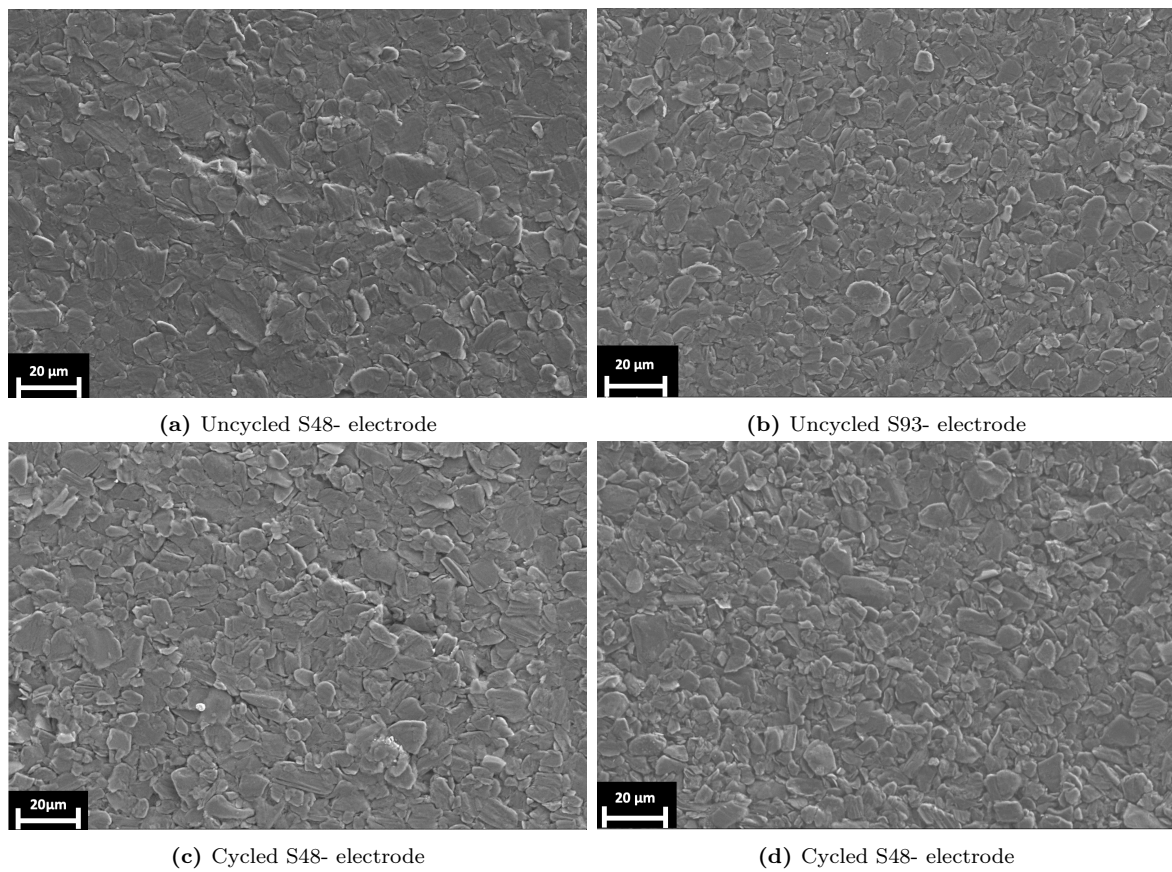


Figure 4.15: SEM micrographs of the electrode surface for uncycled and cycled S48- and S93-electrodes.

4.5 Porosity graded electrodes

In this section, the results of the porosity graded electrode experiments are presented. Based on the results from the tortuosity measurements and the fast charge ability of the S48- and S93-powder, the S93-powder was evaluated as the best. Therefore, this powder was used to manufacture the double layer electrodes, in which the results from this process are presented in Section [4.2.3](#).

4.5.1 Cross section characterization of the single- and double- layer electrode

A double layered electrode was compared to a single layered electrode with uniform porosity, by studying their cross section micrographs. The cross sections of the electrodes were generated by an argon ion beam mill at SINTEF Industry. Figure [4.17a](#) and [4.17b](#) presents the cross section micrographs of the double- and single- layer electrode respectively. Be aware that the double- layer electrode used for imaging was made with a gap-size of 100 μm which was higher than what was used for the double layer electrode in the electrochemical tests equal 50 μm . This resulted in a higher loading for the imaged double layer electrode equal 13.56 mg/cm^2 . However, because the same approach was used to calculate the thickness needed to achieve the geometrical densities, the effect of porosity was assumed to be the same. The single layered electrode shown in Figure [4.17b](#) was made with the same gap-size as for the single layer electrode in the electrochemical test equal 200 μm . However, the loading of the imaged electrode was higher and equal 8.88 mg/cm^2 .

The loading of the electrodes used for electrochemical testing are presented in Table [4.9](#).

Because of the large difference in loading for the double- and single-layer electrode the thickness of the electrodes was also large as can be seen from Figure [4.17a](#) and [4.17b](#). The thickness of the double layered electrode was measured with a micrometer screw and equal 101 μm . The same measuring technique gave 66 μm for the single layered electrode. By using the loading of the electrodes, this gave a geometrical density of 1.34 g/cm^3 and 1.35 g/cm^3 for the double- and single- layer electrode respectively. This was close to the aimed average geometrical density of 1.35 g/cm^3 . To verify these values, the geometrical density of the two electrodes can be calculated from the SEM micrographs. This gave thicknesses of approximately 98 μm for the double layer electrode, while it was approximately 64 μm for the single layer electrode. Based on these values and the given loading, the average geometrical density of the double- and single- layer electrode was

1.38 g/cm³ and 1.39 g/cm³ respectively. A small difference in the geometrical density was therefore observed when measuring the thickness with a micrometer screw and evaluating the SEM micrographs. Moreover, as the exact loading of the layers in the double layer electrode was unknown, the geometrical density of these cannot be determined from the SEM micrographs.

In addition to evaluate the average geometrical densities of the electrodes, a visual consideration of the porosities can be obtained from the SEM micrographs. From Figure 4.17a, a large difference in porosity between the top- and the bottom- layer was observed. The particles in the bottom layer was pressed closer together compared to the top layer, resulting in a thinner bottom layer with less pores. The SEM micrographs shows even layers, in which the density seems to be uniform throughout the layers. Additionally, the interface between the two layers is tight with good contact between them. Moreover, it was observed that the electrode material lost contact with the current collector. However, it cannot be concluded whether this indicates worse adhesion to the current collector or was caused by the argon milling.

The double layer electrode was compared to a single layered electrode with uniform porosity. As can be seen, the porosity was uniform throughout the single layer electrode. Furthermore, the SEM micrographs show that the porosities of the single layer and the top layer of the double-layer electrode was quite similar. A larger difference in porosity was however observed between the bottom layer and the single layer. Lastly, for both electrodes, small porous structures which blocks some of the pores were observed. These structures can be associated to undissolved binder or carbon black agglomerates.

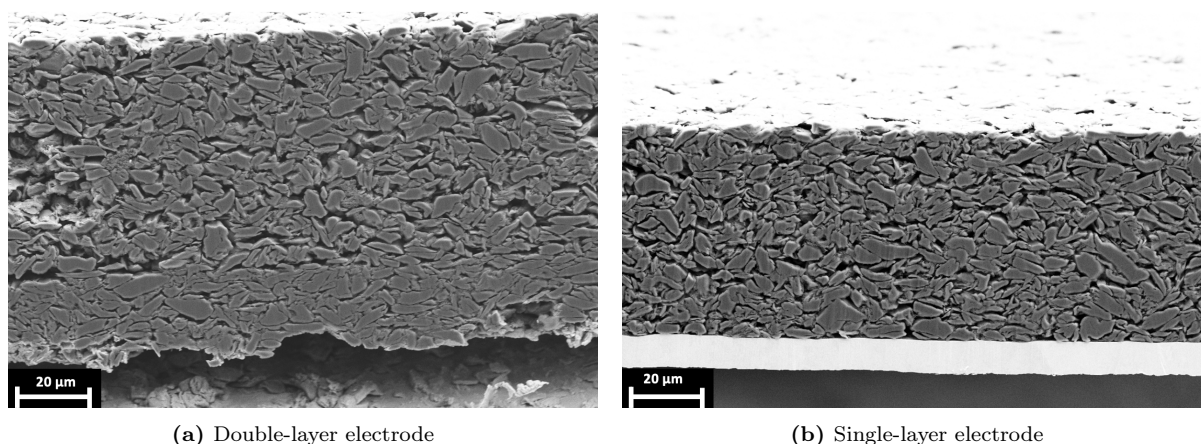


Figure 4.17: Cross section micrographs of a double- and single- layered electrode. The cross sections were obtained by an argon ion beam mill at SINTEF Industry.

4.5.2 Evaluation of fast charge ability of single- and double-layer electrode

To evaluate the fast charge capability of porosity graded electrodes, a double-layered electrode was compared to a single-layered electrode in a charge acceptance test. To achieve as equal conditions as possible, it was preferred to have approximately equal loading of the two electrodes. The loading of the single-layer electrode was optimized to the loading of the double-layered electrode. The double-layered electrode was made by casting two layers with a 50 μm gap-size, as explained in Section 4.2.3. This resulted in a loading equal 7.50 mg/cm^2 . Based on the slurry optimization of the S93-powder presented in Section 4.2 Table 4.3, a solid/liquid-ratio equal 72 % and a fixed gap size applicator with gap-size of 200 μm gave electrodes with loading closest to this value. Although the two electrodes were made with different gap-sizes, the thickness was almost identical for the two cases showing 56 μm and 58 μm for the double- and single-layer electrode respectively. The resulting loading, theoretical capacity, thickness, and geometrical density of the electrodes used in the charge acceptance test are presented in Table 4.9.

Table 4.9: The loading, theoretical capacity, thickness, and geometrical density for the double- and single-layer electrode used in the charge acceptance test.

Electrode	Loading [mg/cm^2]	Theoretical capacity [mAh/cm^2]	Thickness [μm]	Geometrical density [g/cm^3]
Double layer	7.50	2.44	56	1.34
Single layer	7.88	2.56	58	1.36

The basis of the charge acceptance test comparing the fast charge ability of the double- and single-layer electrodes is similar as shown in Figure 4.11. Here, the cell potential and the potential of the working- and counter- electrode as a function of time are presented for the S93-cell.

From the first formation cycle at C/30 of the double- and single-layer electrode cell, a maximum capacity equal 330 mAh/g and 340 mAh/g respectively was reached during delithiation. The potential of the graphite electrode as a function of capacity for these cells are given in Appendix D.1 Figure D.1. These values were both higher than the specific capacity of the S93-powder from Figure 4.3b. Additionally, the maximum capacity of the single layer electrode cell was higher than for the double layer electrode cell.

The results from the charge acceptance test are presented in Figure 4.18 and shows the capacity as a function of cycle number for the single- and double-layer electrode cell.

The lithiation rates from C/2 to 5C are also presented in the figure. As can be seen, the double-layered electrode cell had a considerably lower rate performance compared to the single-layered electrode cell. The single-layered electrode reached a maximum capacity equal 304 mAh/g which corresponds to a SOC equal 89.4 % at C/2 based on the maximum obtained capacity from the formation cycle during delithiation. On the other hand, the double-layer electrode only reached a maximum capacity of 272 mAh/g at C/2. This corresponds to a SOC equal 82.4 % based on the capacity obtained from the first formation cycle. Moreover, it was observed that the capacity of the five last cycles at C/2 was lower than the capacity for the initial five cycles for both cells. As can be seen from the figure, the double-layered electrode reached lower capacity than the single-layer electrode regardless of the current, however the differences decrease with increasing C-rate. The figure shows that the capacity drop was higher for the double-layer electrode specially for the three first lithiation rates. Already at 1C the graded sample showed a drastic reduction in the reversible capacity. This can be seen as an increase from C/2 to 1C resulted in a capacity drop of 21.7 % for the single-layer electrode, while it was 46.44 % for the double-layered electrode. Similar trend was observed when increasing the intercalation rate from 1C to 1.5C. Here, the capacity of the double-layered electrode decreased with 59.1 % while the capacity drop equal 31.66 % for the single-layer electrode.

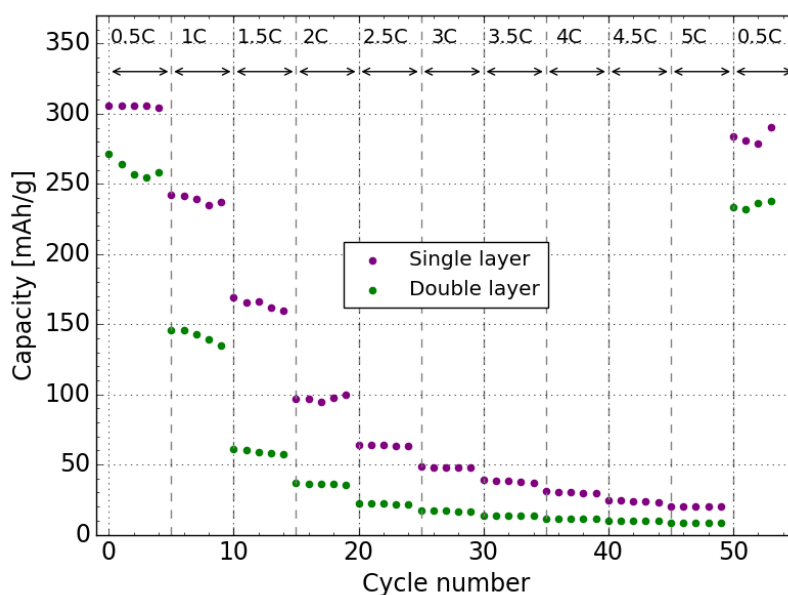


Figure 4.18: Capacity as a function of cycle number for cells having double- and single-layer graphite electrodes. The figure also includes the different lithiation rates from C/2 to 5C. A constant delithiation rate equal C/2 was used. The cell had oversized LFP as the working electrode, graphite as counter electrode, and lithium metal as the reference electrode. The cycling currents were based on the loading of the graphite electrode and the specific capacity of the S93-powder.

The potential of the graphite electrode vs. Li/Li^+ as a function of capacity for the single- and double-layered electrode cell at $C/2$ and $1C$ are presented in Figure 4.19. Similar as for Figure 4.13 the upper potential in this figure was sat to 0.5V to obtain a better visual of the lithiation curves. However, in reality the counter electrode reached 1V during delithiation.

From Figure 4.18 it was shown that the double layered electrode cell had a lower SOC and a larger capacity drop going from $C/2$ to $1C$. This was confirmed by studying Figure 4.19. At charging rate equal $C/2$, the first plateau in the delithiation curve was longer for the single layer electrode. This indicates that this electrode was more lithiated than the double layer electrode. Furthermore, at $1C$ the first plateau during delithiation was no longer visible for the double layer electrode cell. This also confirms a lower degree of lithiation for this cell.

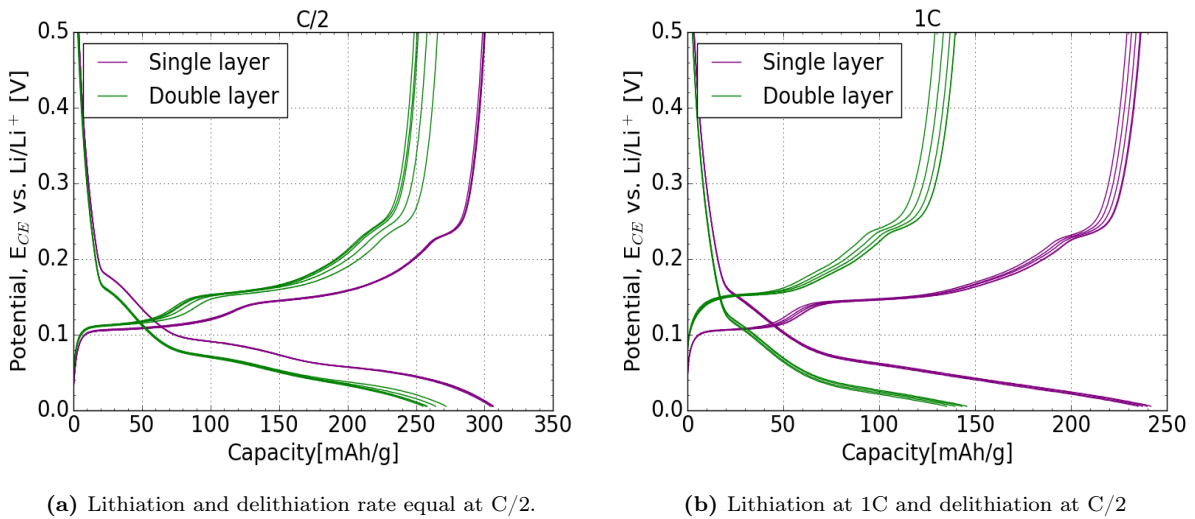


Figure 4.19: The potential of the graphite electrode vs. Li/Li^+ as a function of capacity comparing the single- and double- layer electrode cell.

Figure 4.20 and 4.21 shows the Nyquist plots before and after the charge acceptance test for the double- and single- layered electrode cell respectively. The experimental data are fitted to the Randles circuit shown in Figure 3.6, and the parameters are presented in Appendix D.4 Table D.5 and D.6 for the double- and single- layered electrode cell respectively. As can be seen from these results, the double-layered electrode showed a higher total resistance as both the electrolyte- and the charge transfer- resistance was highest for this cell. This can be seen as the resistance in the electrolyte equal $5.13 \pm 0.04\Omega$ and $4.32 \pm 0.03\Omega$ for the double- and single- layered electrode cell respectively before the charge acceptance test. Moreover, the charge transfer resistance equals $6.56 \pm 0.10\Omega$

and $5.93 \pm 0.11\Omega$ for double- and single- layered electrode respectively before the charge acceptance test. The higher resistance in the double- layered electrode cell indicates that more energy was required to transport lithium ions into the electrode. Discussion of these results is given in Section [5.2.2](#)

By comparing the results from the EIS-measurements before and after the charge acceptance test, the goal was to study the degradation of the cells. However, by evaluating the EIS-results this cannot be understood fully. For the double layered electrode, the resistance in the electrolyte decreased going from before to after the test showing $5.13 \pm 0.04\Omega$ and $4.91 \pm 0.04\Omega$ respectively. The opposite tendency was observed for the charge transfer resistance which increased from $6.56 \pm 0.1\Omega$ to $6.80 \pm 0.17\Omega$ before and after the charge acceptance test respectively. For the single-layer electrode both the electrolyte resistance and the charge transfer resistance decreased going from before to after the test. The charge transfer resistance showed $5.93 \pm 0.11\Omega$ before, and $5.79 \pm 0.08\Omega$ after, while the resistance in the electrolyte equal $4.32 \pm 0.03\Omega$ before and $4.06 \pm 0.02\Omega$ after the charge acceptance test.

Because the two resistances barely changed during the charge acceptance test for the two cells, it indicates that no major changes have occurred during this period.

As the same set- up as was used for the impedance measurements of the S48- and S93-cells was used, the diffusion coefficient could not be extracted from the Warburg data. However, discussion of parameters affecting the diffusion of lithium ions are presented in Section [5.2.2](#)

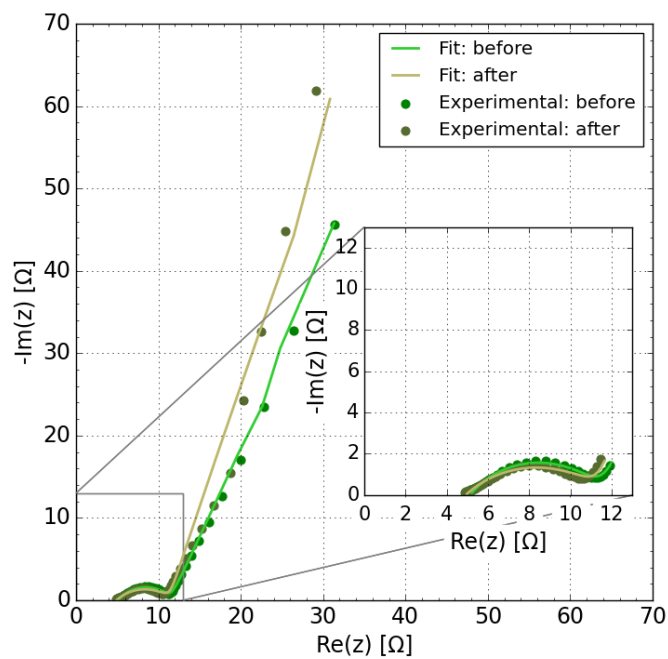


Figure 4.20: Nyquist plot before and after the charge acceptance test of the double layered electrode cell.

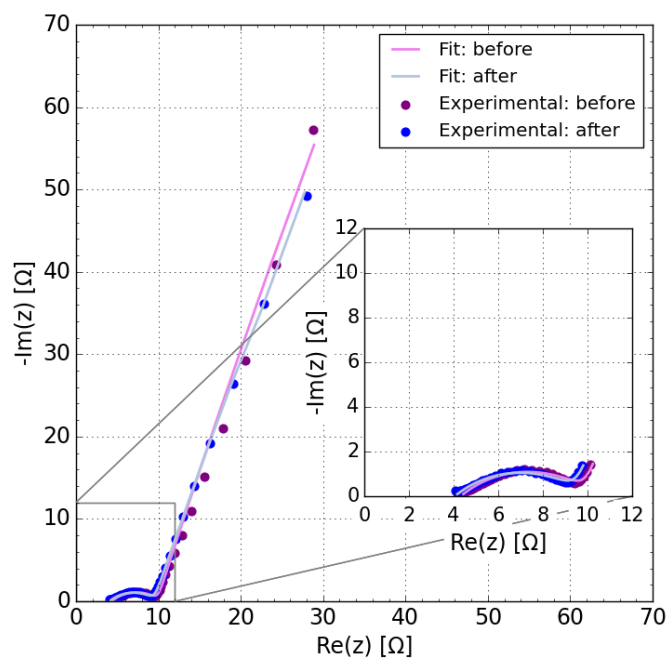


Figure 4.21: Nyquist plot before and after the charge acceptance test of the single layered electrode cell.

5 Discussion

5.1 Comparison of the S48- and S93- powder

5.1.1 Tortuosity measurement

The tortuosity measurements gave a lower tortuosity for the S93- electrodes compared to the S48- electrodes. In this section, this result in addition to the ionic conductivity measurements, and the choice of using the simplified TLM are discussed.

As expected, the electrolyte having the lowest concentration of Bu_4NPF_6 equal 0.01M, had the lowest conductivity. This was expected as lower concentration of the salt gives a lower number of ions which reduces the conductivity of the solution. With conductivity of 0.386 ± 0.006 mS/cm for the 0.01M electrolyte and 2.971 ± 0.045 mS/cm for the 0.1M electrolyte, a slope of approximately 1 was observed for the relation of conductivity as a function of concentration.

Moreover, from the Nyquist plots of the electrolytes shown in Figure 4.7 a nonlinear trend of the experimental data was observed. Because of the nonlinear trend, only the high frequency data points were evaluated. The choice of frequency interval affected the values of the electrolyte resistance, hence also the resulting tortuosity values. However, after experimenting with different frequency intervals for the two electrolytes, it was observed that the choice of frequency did not change the tortuosity values substantially. The choice of interval shown to be most critical for the 0.01M electrolyte as this deviated mostly from a linear trend. The KCl- solution on the other hand had an almost linear trend, hence a larger number of experimental data points were evaluated, and a more accurate value of the electrolyte resistance was obtained.

The highest tortuosity was measured for the S48-electrodes. Depending on the electrolyte, the calculations gave the S48- electrodes a tortuosity between 5.20 ± 0.10 and 5.61 ± 0.35 , while it was 3.01 ± 0.07 and 3.79 ± 0.36 for the S93- electrodes. From the definition of tortuosity presented in Section 2.8.2 this means that the S48-electrodes had longer pathways through the electrode compared to the S93- electrodes. The main reason for these results was believed to be caused by the different particle shapes of the two powders. From the SEM micrographs of the uncycled electrodes presented in Figure 4.15, the S93- particles seemed rounder compared to the S48-particles in which a flake-like structure was more visible. A more flake-like structure may give better overlapping of the particles, hence also a higher tortuosity compared to an electrode with rounder particles.

The particle shape can further be evaluated from the SEM micrographs of the powders in Figure 4.2. Here, the S93-particles tend to agglomerate more. However, because this was not observed at the electrode surface or at the cross section of the single layer electrode, it was assumed that the particles have dispersed properly during the slurry production. Other parameters that could have affected the tortuosity were geometrical density of the electrodes, PSD and particle size. However, as the results showed a small difference in PSD and the geometrical densities, these factors did not contribute to the observed difference in tortuosity. From the BET- analysis, the S48-particles was smaller than the S93-particles, which according to the theory causes a higher tortuosity. However, as this difference was small, it would not affect the results to a large extend.

By evaluating the results presented in Figure 4.9 the simplified TLM seemed to be a good fit. The validation of using the simplified TLM can be evaluated by considering the dependency of the electrolyte conductivity. This was done in the article "Tortuosity of Battery Electrodes: Validation of Impedance-Derived Values and Critical Comparison with 3D Tomography" written by Johannes Landesfeind et al. [82]. Here they measured the tortuosity of NMC and graphite electrodes using electrolytes with conductivity of 0.156 mS/cm and 6.97 mS/cm. In the simplified TLM the contribution from the resistance in the active electrode material was neglected as this was assumed to be considerably lower compared to the ionic resistance. The article shows how this assumption could be verified by evaluating the product of the ionic resistance and the electrolyte conductivity.

The same approach was used to determine whether the simplified TLM was valid for this experiment. If the resistance of the electrodes was to be neglected, the tortuosity should have been constant when using electrolytes with different conductivity. This would imply that the contribution from the electrode resistance was very much lower compared to the electrolyte resistance even when using electrolytes with high conductivity. However, this was not the case. The S48- electrodes had a tortuosity equal 5.20 ± 0.10 and 5.61 ± 0.35 , while the S93-electrodes had 3.01 ± 0.07 and 3.79 ± 0.36 for the 0.01M and 0.1M electrolytes respectively. By evaluating the product of the electrolyte conductivity and ionic resistance from the measurements, 0.044 cm^{-1} and 0.048 cm^{-1} were given for the 0.01M and 0.1M electrolytes respectively for S48. Similar calculations gave 0.027 cm^{-1} and 0.033 cm^{-1} for the 0.01M and 0.1M electrolytes respectively for S93. Because the differences of these products are relatively small considering that the conductivity of the

electrolytes varied with a factor close to 10, the simplified TLM was evaluated as valid for this experiment. The fact that graphite has a high conductivity equal 10^4 S/cm^[83] strengthens the assumption of neglecting the resistance of this material. Moreover, by using electrolytes with low conductivity this assumption is more likely to be satisfied, as this gives an electrolyte resistance much higher than the electrode resistance^[82].

Lastly, the difference in tortuosity was highest for the S93-electrodes equal 0.78, while it was 0.41 for the S48-electrodes. Because the same electrolytes were used for the S48- and S93- electrodes, it was expected that the dependency of the electrolyte conductivity would be the same for both cases. Therefore, the larger differences in tortuosity for the S93-electrodes was expected to be caused by natural differences in the cells. From Table 4.6 the differences in loading were small for the electrodes, only varying with 0.01 mAh/cm² at the most. Also, the geometrical density was almost identical for all electrodes. These factors are therefore not expected to contribute to the larger differences in tortuosity obtained for the S93-electrodes.

5.1.2 Fast charge ability

To evaluate the fast charge ability of the two powders, an anode controlled 3-electrode cell was used with an oversized LFP cathode. This setup allowed for fully utilization of the anode as the cathode contained more lithium ions than the graphite electrode could store. In this way the potential limitations were controlled by the anode, which was preferred when investigating the performance of graphite electrodes. Based on this, the anode controlled cell was preferred over a cell in which the N/P-ratio had to be considered. For a N/P-ratio larger than 1, the anode has the highest capacity, which makes the cathode as the limiting electrode.

However, there might have been a limitation related to the oversized LFP cathode for the anode controlled cell during the 3-electrode experiments. As this electrode had a capacity of 3.5 mAh/cm³ the thickness of this cathode was high. This might have limited the lithiation rate, which was seen as a low discharge rate (lithiation of the LFP cathode) of C/2 was needed for the charge acceptance test.

From the first formation cycle at C/30, the maximum discharge capacity of the S93-cell was 6.35 % higher than the specific capacity of the powder found by cycling coin cells at C/30. However, the opposite trend was observed for the S48-cell. Here, the specific capacity of the powder obtained from coin cells at C/30 was 2.85 % higher than the

discharge capacity from the first formation cycle of the 3-electrode cell. These differences may have been caused by local differences in the cells and unstable cycling temperature in the cycling room. Also, the fact that the coin cell used lithium metal, while the 3-electrode cell had LFP as the lithium source could have influenced the performance. Lastly, the formation programs of the coin cells and 3-electrode cells were different, which also could have affected the obtainable capacities.

The results from the charge acceptance test showed that the S93-cell had the best rate performance. Based on the discharge capacity obtained from the first formation cycle at C/30, the S93- cell had the highest SOC equal 93.7 % while the S48-cell achieved a maximum SOC equal 90.9 %. Moreover, the capacity dropped 20.6 % for the S48-powder, which was larger compared to 13.9 % for the S93-powder when increasing the lithiation rate from C/2 to 1C.

There are multiple factors that could have contributed to the better performance of the S93-cell. As presented in the theory, the particle shape and size, porosity, and tortuosity affect the rate performance of an electrode. The influence of porosity is in this case however expected to be neglected, as both electrodes were calendered to a geometrical density of 1.35 g/cm³. Although there might have been small deviations of density between the two electrodes, this effect would have been too small to affect the rate-performance substantially.

In terms of particle size, the PSD- analysis showed a slightly smaller mean particle size for the S48-powder, with d50 equal 9.75 μm and 11.72 μm for the S48 and S93 respectively. Because the S48- powder had smaller particles one should expect that this powder also had the largest surface area. However, this was not the case. The result from the BET-analysis showed that the surface area equal 1.0210 m²/g for S48 while it was 1.2916 m²/g for S93. From the theory Section [2.8.3](#) the compromise of having small particles to quickly reach a high SOC and the risk of increasing the SEI formation was discussed. As the S48 particles were smaller while the surface area was larger for the S93 powder, this would imply a better performance of the S48 powder. However, this was not the case. Because the differences between the particle size and surface area were small, the influence of these parameters are too small to affect the result to a large extend. Moreover, the unexpected result of S48 having a smaller surface area while having smaller particles may not be accurate. As the SEM micrographs of the powders showed more agglomerates of the S93-powders this could have affected the PSD- analysis. Error in the measurements could

also have been cause using too small amounts of powder in the BET- analysis.

In contrast, the effect of particle shape seems to be important for the performance of the electrodes. Evaluation of the results from the powder characterization indicates more edge planes of the S93- powder. However, as the accessibility of the edge planes was not measured in this work, this is only based on a qualitative evaluation of the SEM micrographs. More accessible edge planes for the S93-powder improves the intercalation rate of lithium ions as explained in Section [2.6](#). This contributes to a better fast charge ability of the S93-powder.

As previously discussed, the particle shape also affects the tortuosity of the electrodes. This was evaluated as the main reason for the improved rate-performance of the S93-cell. From the theory Section [2.8.2](#), it was explained that electrodes having a high tortuosity often have lower intercalation rate, uneven current distribution and hence also more rapid degradation of the electrodes. This is in line with the observations of the rate performance. Because the S93-electrode had the lowest tortuosity, the lithium ions had a shorter pathway from the electrode surface towards the current collector which resulted in a faster transport of solvated lithium ions into the porous electrode. For the S48-electrode on the other hand, the pathway was longer and more tortuous. This inhibits the solvated lithium ions' ability to quickly diffuse into the porous electrode which further decreases the intercalation rate. As the difference in capacity was largest at C/2 and 1C, the effect of tortuosity seemed to be most important at these currents. At higher currents the diffusion of lithium ions in the porous structure is not fast enough. Consequently, only the graphite particles close to the surface are being almost fully lithiated, while the particles closer to the current collector have a lower SOC. This further contributes to polarization of the electrode such that the potential limitations of the electrodes are reached. Therefore, at high currents none of the electrodes enabled to obtain a high transportation rate of lithium ions into the porous electrode, hence the capacity of the two cells became almost identical.

This theory was strengthened by studying the potential curves at C/2 and 1C in Figure [4.13](#). As the SOC of the S93-cell was higher than for the S48- cell at C/2, it indicated that this cell was more lithiated. The higher lithiation of the S93-electrode is in addition to be affected by tortuosity, also affected by the concentration of the solvated lithium ions in the porous structure.

As explained in the theory Section [2.7.2](#), the concentration of lithium in the electrolyte

is likely to be reduced as the distance to the current collector decreases. For an electrode with low tortuosity, the pathway for solvated lithium ions is shorter which enable them to faster diffuse into the electrode. This ensures higher concentration closer to the current collector, compared to electrodes with higher tortuosity. As a result, a higher fraction of the active electrode material is being utilized for an electrode with low tortuosity.

In terms of degradation, both the particles size, and tortuosity are important parameters. As explained in theory, an electrode with high tortuosity tends to have higher probability of degradation, as uneven current densities are expected at the surface. However, from the SEM micrographs of the cycled electrode surfaces presented in Figure [4.15](#) there were no signs of degradation. This was expected as the lower potential limit was set to 5 mV for the graphite electrode, which ensured a potential outside the region that favours lithium plating.

Furthermore, the resistance in the cells was evaluated with EIS-measurements. The electrolyte resistances were almost identical for the two cells showing $4.52 \pm 0.05 \Omega$ and $4.48 \pm 0.02 \Omega$ for the S48-cell and S93-cell respectively. This was expected as the same electrolyte was used in both cases. By comparing the charge transfer resistance, a larger difference was observed as the S48-cell had $7.39 \pm 0.12 \Omega$ while it was $5.90 \pm 0.09 \Omega$ for the S93-cell. The observed difference in charge transfer resistance is in line with the observation from the charge acceptance test. The higher resistance for the S48-cell indicates that the process of converting the solvated lithium ion to lithium metal in this cell was slower, which reduces the rate performance. The main theory for these results is believed to be caused by the larger fraction of edge-planes in the S93-electrode, which improves the charge transfer process in this cell.

In contrast to the charge transfer- and electrolyte- resistance, the diffusion of lithium ions was more challenging to evaluate from the EIS-results. The choice of using the finite open Warburg element in this project was based on the paper "Electrochemical Impedance and its Applications in Energy-Storage Systems" written by Deyang Qu et al. [\[51\]](#). In this article, they showed how the diffusion coefficient could be calculated from both the infinite and the finite Warburg element. For the finite open Warburg element the diffusion length in the graphite particles had to be known. The article suggested that the effective diffusion length could be found by calculating the length of the basal planes. Although the diffusion coefficient have been calculated by using the Warburg element for porous battery electrodes in some studies [\[84\]](#) [\[85\]](#), other papers have argued that the as-

assumptions in the Warburg impedance is not fulfilled for a porous electrode^{[67][51]}. Firstly, the Warburg element assumes a planar geometry which is not the case for the graphite electrodes. Secondly, the model assumes pure diffusion without any contributions from migration and convection. As the infinite Warburg model is based in Fick's second law^[51] it assumes an homogeneous diffusion of charge carriers. However, this is not the case for porous electrodes. The diffusion of lithium ions depends on solid state diffusion in the graphite particles, as well as diffusion in the electrolyte which are present in the pores of the electrode^[51]. The solid state diffusion, is according the article "Electrochemical Impedance and its Applications in Energy-Storage Systems" written by Deyang Qu et al.^[51] homogeneous. However due to the anisotropic properties of graphite described in Section 2.6, the diffusion is only homogeneous in the basal plane. Moreover, as the electrode have pores with different sizes, the diffusion inside the pores is expected to be heterogeneous^[51]. Consequently, Fick's second law is not suitable for a porous electrode. An alternative model to evaluate an porous electrode is described in "Diffusion impedance of electroactive materials, electrolytic solutions and porous electrodes: Warburg impedance and beyond" by Jun Huang^[67], which present a model for spherical and cylindrical geometries. Furthermore, the use of transmission line model have also been presented as a model to evaluate porous electrodes^[51]. Although the diffusion coefficient could not be obtained from the impedance data, a qualitative analysis can be done. Firstly, as synthetic graphite powders were used for both anodes, the solid-state diffusion was assumed to be quite similar for the two cases. The biggest difference in diffusion of lithium ions in the S48- and S93-electrodes was believed to be in the porous structure. As discussed, this was among others affected by the tortuosity and the particle shape.

5.2 Porosity graded electrodes

5.2.1 Manufacturing

The manufacturing of the doubled layer electrodes was challenging. This was mostly related to the calendaring of the bottom layer which creased the anode laminate. Consequently, an uneven top layer was applied. This resulted in a large deviation of loading for these electrodes compared to the deviation observed for the single layered electrodes. This can be seen in Table 4.4 having a deviation of 6.4 % and 5.3 % for the double layer electrodes made by a 50 μm and 100 μm gap-size respectively. In comparison, the standard deviation equal 3.4 % for single layer electrodes made with gap-size of 150

μm which can be seen in Table 4.3. The wavy structure seemed to be due to plastic deformation of the current collector^[86]. This deformation was probably caused by the high demand of energy that was needed for the calendaring. The results showed best performance when choosing the thinnest Cu-foil, however none of the attempts gave an optimal result. One way to improve the manufacturing of the double layer electrodes is by heating the laminate during calendaring such that the deformation of the current collector is reduced. This method was used in the article "Experimental and Simulation Investigations of Porosity Graded Cathodes in Mitigating Battery Degradation of High Voltage Lithium-Ion Batteries" written by Lin Liu et al^[13]. Here a double layered LNMO cathode laminate was made by hot rolling the laminates at 100 °C to the preferred thickness. By using this method, no observation of a wavy bottom layer was reported. Worth noting, aluminium foil was used in their experiments, hence some differences from the Cu-foil would be expected.

From the SEM cross section micrographs, the average geometrical density was calculated to be 1.38 g/cm³ and 1.39 g/cm³ for the double- and single-layer electrode respectively. This was higher than the geometrical density found from measuring the thickness with a micrometer screw which gave 1.34 g/cm³ and 1.35 g/cm³ for the double- and single-layer respectively. The difference in the measured densities was probably caused by errors during measuring with the micrometer screw. Therefore, the geometrical density obtained from the SEM micrographs was evaluated as more accurate, hence these densities are used for the further discussions.

The single layer electrode had a uniform porosity and showed a more porous structure compared to the bottom layer of the double layer electrode. This was expected as the aimed geometrical densities were 1.45 g/cm³ and 1.35 g/cm³ for the bottom- and single-layer respectively. In contrast, the difference in porosity of the single layer and the top layer was not as clear. This was unexpected as the aimed geometrical densities were 1.25 g/cm³ and 1.35 g/cm³ for the top- and single-layer respectively. However, one can not necessarily observe the difference between 1.25 g/cm³ and 1.35g/cm³ visually. To evaluate the exact porosities, analysis techniques such as FIB-SEM tomography could have been used.

The average geometrical density of the double layer equal 1.38 g/cm³ was denser than expected. This could have been caused by three reasons: the bottom layer was denser than the aimed value of 1.45 g/cm³, the top layer was denser than the aimed value of

1.25 g/cm³, or that both layers were denser than the aimed values.

To detect the geometrical densities of the two layers, the loading had to be known for both layers. As the standard deviation of the loading for the double-layer electrodes was high equal 5.3%, the loading of the two layers could not be determined. Consequently, the geometrical densities could not be found from the SEM micrographs. To estimate the loading of the two layers, the experiments must have been reproducible such that more statistics could have been obtained.

However a qualitative analysis of the porosity of the two layers can be given. Theoretically, one should expect that the double layer electrode made by two layers of 100 μm gap-size had a loading corresponding to twice the loading of an electrode made by a single layer of 100 μm gap-size. However, this was not the case. The average loading of the double layer electrode equal 14.62 ± 0.77 , which was more than three times higher than the loading of a single layer electrode made with 100 μm gap size which equal 4.25 ± 0.21 mg/cm². This can be seen from Table 4.3 and 4.4 for the single- and double- layer electrodes respectively. This large difference was expected to mainly be caused by the top layer, as an uneven distribution of slurry was observed. For the calculation of the thickness needed to calender the top-layer to 1.25 g/cm³, it was assumed that the loading of the bottom- and top-layer was identical. As this was not the case, this assumption may have caused a higher density than preferred for the top layer. Additionally, it was assumed that the density of the bottom layer remained unchanged during calendaring of the top layer. However as the loading of the top layer probably was higher than expected, this may have caused a too high pressure on the laminate, such that the density of the bottom layer also changed. Be aware that this analysis only is qualitative, and that proper measuring techniques are needed to obtain the correct evaluation of the densities of the two layers.

5.2.2 Fast charge ability of porosity graded electrodes

The results from the charge acceptance test showed that the single layered electrode had better rate performance compared to the double layered electrode. Firstly, the single layer electrode cell reached a higher capacity during the first formation cycle at C/30 equal 340 mAh/g. In comparison the double layer electrode cell reached 330 mAh/g for the same C-rate. Based on these capacities, the double layer electrode obtained a SOC equal 82.4 % while it was 89.4 % for the single layer electrode at C/2 during the charge acceptance test.

As the single layer electrode were made by the same powder and solid/liquid-ratio as the graphite electrode in the S93-cell, it was expected that these cells obtained similar SOC. However, this was not the case, as the S93-cell reached a SOC equal 93.7% at C/2 during the charge acceptance test. This tendency was most likely caused by the different loadings, as the S93-cell had graphite with loading equal 5.84 mg/cm² while it equal 7.88 mg/cm² for the single layer electrode. Consequently, the single-layer electrode was thicker, which gave a longer diffusion length for the solvated lithium ions. As a result, a lower utilization of the active material was obtained for the single-layer electrode.

Moreover, the capacity drop was considerably larger for the double layered electrode equal 46.4 % going from C/2 to 1C, while it was 21.7 % for the single electrode. The capacity drop going from 1C to 1.5 C equal 59.1 % and 31.4% for the double- and single- layer electrode respectively. Compared to the literature, these results were unexpected. In the article "Gradient Porosity Electrode for Fast Charging Lithium-Ion Batteries" written by Jian Yang et. al [\[12\]](#), a three layered graphite electrode with porosity of 15 %, 25 % and 35 % for the bottom-, middle- and top- layered respectively was studied. This electrode was compared to single layered graphite electrode with uniform porosity of 25 % with corresponded to the average porosity of the three layer electrode. Their results showed that the specific capacity was almost identical for both electrodes. Moreover, the three layer electrode reached higher capacities than the single layered electrode at higher C-rates. Although this article used a three layer electrode, similar trend was expected by using a double layered electrode.

There are multiple reasons for this unexpected result. Firstly, as the manufacturing of the double layer electrodes was challenging and time consuming, lack of statistics affects these results. The reproducibility of these experiments has to be improved to determine the fast charge ability of graded graphite electrodes.

Furthermore, the results may have been affected by poor electrical contact between the current collector and the bottom layer in the double layer electrode. From the cross section micrographs, the bottom layer had lost contact to the current collector. As this was not observed for the single-layer electrode, this may indicate worse adhesion to the current collector, which affects the fast charge ability. However, it can be determined whether this was only caused by the argon milling.

Another reason for the reduced performance of the double layer electrode may have been caused by the different porosities. As the density of the top layer in theory should have been

lower than for the single layer electrode, the transport of solvated lithium was expected to be fastest in the top layer. However, as discussed in Section 5.2.1, the density of the top layer could have been higher than expected due to the unexpected higher loading. Consequently, the electrolyte's ability to penetrate into the porous electrode was reduced in the top layer. The transportation rate of solvated lithium would therefore be quite similar for the single- and top-layer. Moreover, because the bottom layer was denser than the single layered electrode, the available pathways would be less and more tortuous in the bottom layer. Consequently, the electrolyte enabled to penetrate deeper into the single layer electrode, giving this electrode a higher total transportation rate of lithium ions. As a result, a larger degree of graphite particles was being lithiated in the single layer electrode, which improves its rate performance. This is in line with Figure 2.8 shown in theory Section 2.7.3, which shows how the particles closer to the electrode surface would be lithiated faster compared to particles closer to the current collector.

The fact that the single layered electrode was more lithiated than the double layered electrode was confirmed by evaluating the potential curves presented in Figure 4.19. The first plateau during delithiation at $C/2$ was longer for the single layer electrode, which indicates that a larger fraction of the active material was being utilized in this electrode. This theory was strengthened as the first plateau in the delithiation curve at $1C$ for the double layer electrode was not visible.

Moreover, because the thickness of the electrodes was almost identical equal $56\ \mu\text{m}$ and $58\ \mu\text{m}$ for the double- and single- layered electrode respectively, the diffusion length was almost identical for the two electrodes and should therefore not affect the result to a large extent. The thickness of the single layered electrode was slightly higher as this electrode had a higher loading equal $7.88\ \text{mg}/\text{cm}^2$ compared to $7.50\ \text{mg}/\text{cm}^2$ for the double layered electrode. This difference in loading was however evaluated as too small to contribute to the large difference in rate performance.

Furthermore, the resistance in the cells having the single- and double- layered electrodes was evaluated with EIS- measurements. Be aware that the difference in loading of the two graphite electrodes can have affected these results.

The results showed that the double-layered electrode cell had the highest electrolyte- and charge transfer- resistance, which gave the cell a higher total resistance. The biggest contribution to the higher resistance for the double- layered electrode was believed to be caused by the dense bottom layer. This was based on the previously presented theory that the electrolytes ability to penetrate into the bottom layer was lower compared to

the single-layered electrode. In addition, if the contact between the bottom layer and current collector was sub-optimal, this would also contribute to increase the resistance in the double layer electrode cell. Additionally, as the density of the two electrodes was different the tortuosity would probably also be different which also affects the resistance in the cell. The particle shape and size did not affect the impedance results as the same powder was used for the two electrodes.

Furthermore, the electrolyte resistance before and after the charge acceptance decreased for both cells. This may indicate poor wetting of the electrodes. This indicates that the electrolyte had not enabled to wet the electrode properly before the charge acceptance test. However, after the charge acceptance test, more time had passed, which may have given better wetting of the electrodes.

In contrast, the charge transfer resistance increased going from before to after the charge acceptance test for the double-layered electrode, while it was reduced for the single-layered electrode. In both cases this difference was not substantial, and the difference can only be caused by small differences such as temperature in the cycling room. Because of the small changes in the electrolyte- and charge transfer- resistances before and after the charge acceptance test for the two cells, no major degradation was believed to have occurred at the electrodes.

6 Conclusion

From this work, the effect of tortuosity and porosity have shown to be important for the battery performance. Further, the morphology affected the tortuosity, and hence constitutes an important parameter for the electrode performance.

From the EIS-measurements on symmetrical graphite-graphite cells employing non intercalating salts, the simplified transition line model gave tortuosity values for the S93-electrodes of 3.01 ± 0.07 and 3.79 ± 0.36 for the 0.01M and 0.1M electrolyte respectively. The S48-electrodes had a higher tortuosity equal 5.20 ± 0.10 and 5.61 ± 0.35 for the 0.01M and 0.1M electrolyte respectively. The higher tortuosity of the S48-electrodes was caused by the different morphology of the two powders. Here, the particle shape was evaluated as an important parameter. The SEM micrographs showed a more flake-like structure of the S48-particles compared to the S93-powder which had rounder particles. Consequently, the S48-particles tend to overlap more causing a higher tortuosity. Furthermore, the fast charge ability of the S48- and S93-cell was investigated in a charge acceptance test.

The results showed a higher SOC for the S93-cell with 93.7% compared to 90.9% for the S48- cell at C/2 in constant current mode. Additionally, the capacity drop when increasing the rate from C/2 to 1C was highest for the S48-cell equal 20.6%, compared to 13.9% for the S93-cell. The main reason for these results was believed to be caused by the tortuosity. High tortuosity electrodes have long and complex pathways for the solvated lithium ions through the porous electrode. This decreases the intercalation rate hence also the rate performance of the cell. From this it was concluded that lower tortuosity improves the rate performance, and is therefore an important parameter to consider when making electrodes with high loading and low porosity.

Furthermore, the resistance of the S93- was found to be lower than the S48-cell. This result was believed to be caused by a larger fraction of edge-planes for the S93-powder, which increases the intercalation rate in the electrode.

Therefore, after studying the performance of the S48-and S93-cells, it was concluded that the tortuosity of graphite electrode constitutes an important parameter when optimizing the electrode performance. This factor was further affected by the morphology of the synthetic graphite powders, in which the particle shape and fraction of edge planes shown to be important.

Additionally, the effect of porosity graded electrodes was investigated. The manufac-

turing of these electrodes was proven to be challenging. After calendering the bottom layer to a density of 1.45 g/cm^3 , the anode laminate obtained an unwanted wavy structure. Consequentially, an uneven distribution of the top layer was observed, giving the top layer a loading more than three times higher than expected. By comparing the fast charge ability of the double-and single-layer electrode having a loading of 7.50 mg/cm^2 and 7.88 mg/cm^2 respectively, the single layered electrode reached the highest SOC equal 89.4% while it was 82.4 % for the double layer electrode cell. Moreover, the capacity drop was largest for the double layered electrode with the 59.1%, while it was 31.66% for the single-layer electrode going from C/2 to 1C. Two main theories were presented for these results. Firstly, the cross section micrographs showed poor adhesion between the bottom layer and the current collector, which worsening the electrical contact hence also the fast charge ability of the double-layer electrode cell. Secondly, the effect of porosity highly affected the results. As the top layer had a higher loading than expected, it was believed that the density of this layer also became higher than the aimed value of 1.25 g/cm^3 . Consequently, the transport of solvated lithium ions in the porous electrode was assumed to be almost identical for the top-layer and single layer electrode. As the bottom layer was denser than the single-layer electrode, the electrolyte's ability to penetrate this region was reduced in the bottom layer. As a result, the overall transport of lithium ions in the single-layer electrode was believed to be highest which contributed to the better rate-performance.

From the impedance measurements, the total resistance was highest for the double layered electrode. This was also expected to be caused by the dense bottom layer and a sub-optimal contact between the bottom layer and the current collector.

To summarize, the results from the porosity graded electrode experiments was highly effected by the challenging manufacturing of these electrodes. To be able to fully understand the effect of these electrodes during fast charging, more statistics are needed, hence the manufacturing technique must be improved, and more parallels need to be tested.

7 Further work

The results showed an improved rate performance for electrodes with the lowest tortuosity. To meet the demand of high loading electrodes from the industry without sacrificing the rate-performance, the tortuosity is therefore an important parameter to consider for further optimization of graphite electrodes. Moreover, as the morphology of the graphite powders shown to be important for the performance of the electrodes, further optimization of this is needed. Here, factors such as particle size and shape, and fraction of edge-planes must be optimized to improve the rate-performance, while limiting the irreversible capacity loss from the SEI-formation.

In terms of the double layer electrodes, the manufacturing technique must be improved. The main challenge was related to the calendaring of the bottom layer. One alternative to reduce this deformation might be to use heat when calendaring, such that the plastic deformation of the Cu-foil is reduced. By obtaining an even bottom layer, the loading of the two layers would be close to identical. This makes it possible to achieve a more accurate geometrical density of the two layers.

In addition to improve the manufacturing of the double layer electrodes, further optimisation of these electrodes is desired. For instance, the geometrical densities used for the different layers can be optimized, to obtain the perfect combination of high loading, and porous structure to improve the transport of lithium ions. Moreover, experimenting with different numbers of layers and hence the densities of them would also contribute to optimize these electrodes. Lastly, the thickness of the layers could vary. Instead of casting the top and bottom layer with the same gap-size, once could vary the thicknesses, to improve the transport of lithium ions.

As an alternative to porosity graded electrodes, a porosity gradient could also be achieved by using graphite powders with different particle sizes. One option is to use a powder with small particle size for the bottom layer, while the top layer consists of a powder with larger particles. The entire laminate can then be calendared to a specific geometrical density. This eliminates the challenges related to calendaring the bottom layer. Furthermore, a higher density is expected for the bottom layer as the small particles enables to be stacked closer together. The top layer on the other hand would have a more porous structure, as these particles are larger. In this way, some of the theoretical advantages of the graded electrodes should be maintained, while the challenge of calendaring the bottom layer is avoided.

Lastly, as have been shown in this work, the effect of the tortuosity and porosity of the graphite electrode constitutes important factors when optimizing battery performance. Therefore, to achieve the best performance, it is important to evaluate these factors together. By finding the perfect compromise between tortuosity, porosity, and particle size and shape, the performance of the graphite electrode would be improved.

References

- [1] EIA: Courtney Sourmehi. EIA projects nearly 50% increase in world energy use by 2050, led by growth in renewables. Available at: <https://www.eia.gov/todayinenergy/detail.php?id=49876#>, 2021. Accessed: 16.04.2022.
- [2] European Commission. 2050 long-term strategy. Available at: https://ec.europa.eu/clima/eu-action/climate-strategies-targets/2050-long-term-strategy_en, 2021. Accessed: 03.05.2022.
- [3] Our world in data. Cars, planes, trains: where do co2 emissions from transport come from? Available at: <https://ourworldindata.org/co2-emissions-from-transport>, 2020. Accessed: 04.05.2022.
- [4] Julio A. Sanguesa, Vicente Torres-Sanz, Piedad Garrido, Francisco J. Martinez, and Johann M. Marquez-Barja. A review on electric vehicles: Technologies and challenges. *smart cities*, 4(1):372–404, 2021. doi: 10.3390/smartcities4010022.
- [5] Jakob Asenbauer, Tobias Eisenmann, Matthias Kuenzel, Arefeh Kazzazi, Zhen Chen, and Dominic Bresser. The success story of graphite as a lithium-ion anode material-fundamentals, remaining challenges, and recent developments including silicon (oxide) composites. *Sustainable Energy and Fuels*, 4(11):5387–5416, 2020. doi: 10.1039/d0se00175a.
- [6] Anna Tomaszewska, Zhengyu Chu, Xuning Feng, Simon O’Kane, Xinhua Liu, Jingyi Chen, Chenzhen Ji, Elizabeth Endler, Ruihe Li, Lishuo Liu, Yalun Li, Siqi Zheng, Sebastian Vetterlein, Ming Gao, Jiuyu Du, Michael Parkes, Minggao Ouyang, Monica Marinescu, Gregory Offer, and Billy Wu. Lithium-ion battery fast charging: A review. *eTransportation*, 1, 2019. doi: 10.1016/j.etrans.2019.100011.
- [7] Christian Julien, Alain Mauger, Ashok Vijh, and Karim Zaghbi. *Lithium Batteries Science and Technology*. Springer, 2016. doi: 10.1007/978-3-319-19108-9.
- [8] Xianke Lin, Kavian Khosravinia, Xiaosong Hu, Ju Li, and Wei Lu. Lithium Plating Mechanism, Detection, and Mitigation in Lithium-Ion Batteries. *Progress in Energy and Combustion Science*, 87, 11 2021. doi: 10.1016/j.pecs.2021.100953.
- [9] Hao Chen, Allen Pei, Jiayu Wan, Dingchang Lin, Rafael Vilá, Hongxia Wang, David

- Mackanic, Hans Georg Steinrück, William Huang, Yuzhang Li, Ankun Yang, Jin Xie, Yecun Wu, Hansen Wang, and Yi Cui. Tortuosity Effects in Lithium-Metal Host Anodes. *Joule*, 4(4):938–952, 4 2020. doi: 10.1016/j.joule.2020.03.008.
- [10] Tianshu Deng and Xiaoping Zhou. The preparation of porous graphite and its application in lithium ion batteries as anode material. *Journal of Solid State Electrochemistry*, 20(10):2613–2618, 10 2016. doi: 10.1007/s10008-016-3260-1.
- [11] Yiling Dai and Venkat Srinivasan. On Graded Electrode Porosity as a Design Tool for Improving the Energy Density of Batteries. *Journal of The Electrochemical Society*, 163(3):A406–A416, 2016. ISSN 0013-4651. doi: 10.1149/2.0301603jes.
- [12] Jian Yang, Yejing Li, Aleksandar Mijailovic, Guanyi Wang, Jie Xiong, Kevin Mathew, Wenquan Lu, Brian Sheldon, and Qingliu Wu. Gradient Porosity Electrode for Fast Charging Lithium-Ion Batteries. *Journal of Materials Chemistry A*, 2022. doi: 10.1039/D2TA01707E.
- [13] Lin Liu, Pengjian Guan, and Changhong Liu. Experimental and Simulation Investigations of Porosity Graded Cathodes in Mitigating Battery Degradation of High Voltage Lithium-Ion Batteries. *Journal of The Electrochemical Society*, 164(13): A3163–A3173, 2017. doi: 10.1149/2.1021713jes.
- [14] Vianode. Advanced battery materials. Available at: <https://www.vianode.com>, 2022. Accessed: 12.04.2022.
- [15] Naoki Nitta, Feixiang Wu, Jung Tae Lee, and Gleb Yushin. Li-ion battery materials: Present and future. *Materials Today*, 18(5):252–264, 6 2015. doi: 10.1016/j.mattod.2014.10.040.
- [16] Reiner Weyhe and Xiaofei Yang. Investigation about Lithium-Ion Battery Market Evolution and future Potential of Secondary Raw Material from Recycling. Technical report, ACCUREC Recycling GmbH, 2018.
- [17] Jarod C. Kelly, Qiang Dai, and Michael Wang. Globally regional life cycle analysis of automotive lithium-ion nickel manganese cobalt batteries. *Mitigation and Adaptation Strategies for Global Change*, 2019. doi: 10.1007/s11027-019-09869-2.
- [18] Richard Schmuch, Ralf Wagner, Gerhard Hörpel, Tobias Placke, and Martin Win-

- ter. Performance and cost of materials for lithium-based rechargeable automotive batteries. *Nature Energy*, 3(4):267–278, 4 2018. doi: 10.1038/s41560-018-0107-2.
- [19] Mari Hognestad. The effect of porosity and temperature on graphite during fast charging. Technical report, NTNU, 2021.
- [20] Jan C. Keith B. Oldham. *Electrochemical Science and technology, Fundamentals and Application*. Wiley, 2011. doi: <https://doi.org/10.1201/9781351052702>.
- [21] Aylward and Findlay’s. *SI Chemical Data*, volume 7. Wiley, 2014.
- [22] John B. Goodenough and Kyu Sung Park. The Li-ion rechargeable battery: A perspective. *Journal of the American Chemical Society*, 135(4):1167–1176, 1 2013. doi: 10.1021/ja3091438.
- [23] R. Borah, F. R. Hughson, J. Johnston, and T. Nann. On battery materials and methods. *Materials Today Advances*, 6, 6 2020. doi: 10.1016/j.mtadv.2019.100046.
- [24] Hamdi Abdi, Behnam Mohammadi-ivatloo, Saeid Javadi, Amir Reza Khodaei, and Ehsan Dehnavi. Energy Storage Systems. In *Distributed Generation Systems: Design, Operation and Grid Integration*, pages 333–368. Elsevier, 5 2017. doi: 10.1016/B978-0-12-804208-3.00007-8.
- [25] Dong Hyup Jeon. Wettability in electrodes and its impact on the performance of lithium-ion batteries. *Energy Storage Materials*, 18:139–147, 3 2019. doi: 10.1016/j.ensm.2019.01.002.
- [26] Tongtong Liu, Kai Wang, Yongxiu Chen, Shuangliang Zhao, and Yongsheng Han. Dominant role of wettability in improving the specific capacitance. *Green Energy and Environment*, 4(2):171–179, 4 2019. doi: 10.1016/j.gee.2019.01.010.
- [27] Shuowei Dai, Jian Chen, Yanjie Ren, Zhimin Liu, Jianlin Chen, Cong Li, Xinyuan Zhang, Xiao Zhang, and Taofang Zeng. Electrochemical corrosion behavior of the copper current collector in the electrolyte of lithium-ion batteries. *International Journal of Electrochemical Science*, 12(11):10589–10598, 11 2017. doi: 10.20964/2017.11.28.

- [28] Kang Xu. Electrolytes and interphases in Li-ion batteries and beyond. *Chemical Reviews*, 114(23):11503–11618, 12 2014. doi: 10.1021/cr500003w.
- [29] D. Bresser, E. Paillard, and S. Passerini. Lithium-ion batteries (LIBs) for medium- and large-scale energy storage: Current cell materials and components. In *Advances in Batteries for Medium and Large-Scale Energy Storage: Types and Applications*, pages 213–289. Elsevier, 12 2014. doi: 10.1016/B978-1-78242-013-2.00006-6.
- [30] Pekka Peljo and Hubert H. Girault. Electrochemical potential window of battery electrolytes: The HOMO-LUMO misconception. *Energy and Environmental Science*, 11(9):2306–2309, 9 2018. doi: 10.1039/c8ee01286e.
- [31] Keisuke Ushirogata, Keitaro Sodeyama, Zdenek Futera, Yoshitaka Tateyama, and Yukihiro Okuno. Near-Shore Aggregation Mechanism of Electrolyte Decomposition Products to Explain Solid Electrolyte Interphase Formation. *Journal of The Electrochemical Society*, 162(14):A2670–A2678, 2015. doi: 10.1149/2.0301514jes.
- [32] Peng Lu and Stephen J. Harris. Lithium transport within the solid electrolyte interphase. *Electrochemistry Communications*, 13(10):1035–1037, 10 2011. doi: 10.1016/j.elecom.2011.06.026.
- [33] John B. Goodenough and Youngsik Kim. Challenges for rechargeable Li batteries. *Chemistry of Materials*, 22(3):587–603, 2 2010. doi: 10.1021/cm901452z.
- [34] Aiping Wang, Sanket Kadam, Hong Li, Siqi Shi, and Yue Qi. Review on modeling of the anode solid electrolyte interphase (SEI) for lithium-ion batteries. *npj Computational Materials*, 4(1), 12 2018. doi: 10.1038/s41524-018-0064-0.
- [35] Joseph W Abbott and Felix Hanke. Kinetically corrected Monte Carlo-molecular dynamics simulations of solid electrolyte interphase growth. Technical report, Dassault Systemes, Cambridg, 2021.
- [36] Brian J. Landi, Matthew J. Ganter, Cory D. Cress, Roberta A. DiLeo, and Ryne P. Raffaele. Carbon nanotubes for lithium ion batteries. *Energy and Environmental Science*, 2(6):638–654, 2009. doi: 10.1039/b904116h.
- [37] Fernanda F.C. Bazito and Roberto M. Torresi. Cathodes for lithium ion batteries:

- The benefits of using nanostructured materials. *Journal of the Brazilian Chemical Society*, 17(4):627–642, 2006. doi: 10.1590/S0103-50532006000400002.
- [38] Arumugam Manthiram. A reflection on lithium-ion battery cathode chemistry. *Nature Communications*, 11(1), 12 2020. doi: 10.1038/s41467-020-15355-0.
- [39] Hui Bi, Fuqiang Huang, Yufeng Tang, Zhanqiang Liu, Tianquan Lin, Jian Chen, and Wei Zhao. Study of LiFePO₄ cathode modified by graphene sheets for high-performance lithium ion batteries. *Electrochimica Acta*, 88:414–420, 1 2013. doi: 10.1016/j.electacta.2012.10.050.
- [40] M. Simolka, J.-F. Heger, N. Traub, H. Kaess, and K. A. Friedrich. Influence of Cycling Profile, Depth of Discharge and Temperature on Commercial LFP/C Cell Ageing: Cell Level Analysis with ICA, DVA and OCV Measurements. *Journal of The Electrochemical Society*, 167(11):110502, 6 2020. doi: 10.1149/1945-7111/ab9cd1.
- [41] Seung Ho Yu, Xinran Feng, Na Zhang, Jeesoo Seok, and Héctor D. Abruña. Understanding Conversion-Type Electrodes for Lithium Rechargeable Batteries. *Accounts of Chemical Research*, 51(2):273–281, 2 2018. doi: 10.1021/acs.accounts.7b00487.
- [42] Chenglong Wu, Jiulin Hu, Zhenguo Yao, Dongguang Yin, and Chilin Li. Highly Reversible Conversion Anodes Composed of Ultralarge Monolithic Grains with Seamless Intragranular Binder and Wiring Network. *ACS Applied Materials and Interfaces*, 11(26):23280–23290, 7 2019. doi: 10.1021/acsami.9b07169.
- [43] Dongliang Liao, Xuanlin Kuang, Jiangfeng Xiang, and Xiaohong Wang. A Silicon Anode Material with Layered Structure for the Lithium-ion Battery. In *Journal of Physics: Conference Series*, volume 986. Institute of Physics Publishing, 3 2018. doi: 10.1088/1742-6596/986/1/012024.
- [44] Zhenyu Zhang, Keenan Smith, Rhodri Jervis, Paul R. Shearing, Thomas S. Miller, and Daniel J.L. Brett. Operando Electrochemical Atomic Force Microscopy of Solid-Electrolyte Interphase Formation on Graphite Anodes: The Evolution of SEI Morphology and Mechanical Properties. *ACS Applied Materials and Interfaces*, 12(31): 35132–35141, 8 2020. doi: 10.1021/acsami.0c11190.
- [45] Ponor: Our world in data. Graphene - sigma and pi bonds. Available at <https://>

- [//commons.wikimedia.org/wiki/File:Graphene_-_sigma_and_pi_bonds.svg](https://commons.wikimedia.org/wiki/File:Graphene_-_sigma_and_pi_bonds.svg), 2020.
- [46] Qiang Liu, Shuai Li, Senhao Wang, Xianggong Zhang, Sisi Zhou, Ying Bai, Jieyun Zheng, and Xia Lu. Kinetically Determined Phase Transition from Stage II (LiC₁₂) to Stage I (LiC₆) in a Graphite Anode for Li-Ion Batteries. *Journal of Physical Chemistry Letters*, 9(18):5567–5573, 9 2018. doi: 10.1021/acs.jpcclett.8b02750.
- [47] Zhaohui Wang, Arne Petter Ratvik, Tor Grande, and Sverre M. Selbach. Diffusion of alkali metals in the first stage graphite intercalation compounds by vdW-DFT calculations. *RSC Advances*, 5(21):15985–15992, 2015. doi: 10.1039/c4ra15529g.
- [48] M. M. Kabir and Dervis Emre Demirocak. Degradation mechanisms in Li-ion batteries: a state-of-the-art review. *International Journal of Energy Research*, 41(14):1963–1986, 11 2017. doi: 10.1002/er.3762.
- [49] Thomas Waldmann, Björn Ingo Hogg, and Margret Wohlfahrt-Mehrens. Li plating as unwanted side reaction in commercial Li-ion cells – A review. *Journal of Power Sources*, 384:107–124, 4 2018. doi: 10.1016/j.jpowsour.2018.02.063.
- [50] Albert H Zimmerman and Michael V Quinzio. Lithium Plating in Lithium-Ion Cells. Technical report, Aerospace, 2010.
- [51] Deyang Qu, Gongwei Wang, Janak Kafle, Joshua Harris, Logan Crain, Zhihong Jin, and Dong Zheng. Electrochemical Impedance and its Applications in Energy-Storage Systems. *Small Methods*, 2(8):1700342, 8 2018. doi: 10.1002/smt.201700342.
- [52] Alec S. Ho, Dilworth Y. Parkinson, Donal P. Finegan, Stephen E. Trask, Andrew N. Jansen, Wei Tong, and Nitash P. Balsara. 3D Detection of Lithiation and Lithium Plating in Graphite Anodes during Fast Charging. *ACS Nano*, 15(6):10480–10487, 6 2021. doi: 10.1021/acsnano.1c02942.
- [53] Dongxu Ouyang, Yaping He, Jingwen Weng, Jiahao Liu, Mingyi Chen, and Jian Wang. Influence of low temperature conditions on lithium-ion batteries and the application of an insulation material. *RSC Advances*, 9(16):9053–9066, 2019. doi: 10.1039/c9ra00490d.
- [54] Marco T. Marco, Seoung Bum Son, Andrew M. Colclasure, Ilya A. Shkrob,

- Stephen E. Trask, Ira D. Bloom, and Daniel P. Abraham. How Fast Can a Li-Ion Battery Be Charged? Determination of Limiting Fast Charging Conditions. *ACS Applied Energy Materials*, 4(2):1063–1068, 2 2021. doi: 10.1021/acsaeem.0c03114.
- [55] Shu Hua Wang, Ya Xia Yin, Tong Tong Zuo, Wei Dong, Jin Yi Li, Ji Lei Shi, Chang Huan Zhang, Nian Wu Li, Cong Ju Li, and Yu Guo Guo. Stable Li Metal Anodes via Regulating Lithium Plating/Stripping in Vertically Aligned Microchannels. *Advanced Materials*, 29(40), 10 2017. doi: 10.1002/adma.201703729.
- [56] Florian Ringbeck, Christiane Rahe, Georg Fuchs, and Dirk Uwe Sauer. Identification of Lithium Plating in Lithium-Ion Batteries by Electrical and Optical Methods. *Journal of The Electrochemical Society*, 167(9):090536, 5 2020. doi: 10.1149/1945-7111/ab8f5a.
- [57] Md Arafat Rahman, Yat Choy Wong, Guangsheng Song, and Cuie Wen. A review on porous negative electrodes for high performance lithium-ion batteries. *Journal of Porous Materials*, 22(5):1313–1343, 10 2015. doi: 10.1007/s10934-015-0010-1.
- [58] Kevin G. Gallagher, Stephen E. Trask, Christoph Bauer, Thomas Woehrle, Simon F. Lux, Matthias Tschech, Peter Lamp, Bryant J. Polzin, Seungbum Ha, Brandon Long, Qingliu Wu, Wenquan Lu, Dennis W. Dees, and Andrew N. Jansen. Optimizing Areal Capacities through Understanding the Limitations of Lithium-Ion Electrodes. *Journal of The Electrochemical Society*, 163(2):A138–A149, 2016. doi: 10.1149/2.0321602jes.
- [59] Johannes Landesfeind, Johannes Hattendorff, Andreas Ehrl, Wolfgang A. Wall, and Hubert A. Gasteiger. Tortuosity Determination of Battery Electrodes and Separators by Impedance Spectroscopy. *Journal of The Electrochemical Society*, 163(7):A1373–A1387, 2016. doi: 10.1149/2.1141607jes.
- [60] Jay Santoki, Simon Daubner, Daniel Schneider, Marc Kamlah, and Britta Nestler. Effect of tortuosity, porosity, and particle size on phase-separation dynamics of ellipsoid-like particles of porous electrodes: Cahn-Hilliard-type phase-field simulations. *Modelling and Simulation in Materials Science and Engineering*, 29(6), 9 2021. doi: 10.1088/1361-651X/ac11bc.
- [61] Jingyi Wu, Zhengyu Ju, Xiao Zhang, Xiao Xu, Kenneth J. Takeuchi, Amy C.

- Marschilok, Esther S. Takeuchi, and Guihua Yu. Low-Tortuosity Thick Electrodes with Active Materials Gradient Design for Enhanced Energy Storage. *ACS Nano*, page acsnano.2c00129, 3 2022. doi: 10.1021/acsnano.2c00129.
- [62] Fridolin Röder, Sören Sonntag, Daniel Schröder, and Ulrike Krewer. Simulating the Impact of Particle Size Distribution on the Performance of Graphite Electrodes in Lithium-Ion Batteries. *Energy Technology*, 4(12):1588–1597, 12 2016. doi: 10.1002/ente.201600232.
- [63] Bio-. Protocols for studying intercalation electrodes materials: Part i: Galvanostatic cycling with potential limitation (gcpl). Technical report, BioLogic, 2005. URL www.biologic.net.
- [64] Gamry Instruments. Basics of Electrochemical Impedance Spectroscopy. Technical report, Gamry Instruments, 2010.
- [65] Jens Wallauer. Relaxis impedance spectroscopy, user manual. Technical report, rhd instruments, 2013. URL <http://www.rhd-instruments.com>.
- [66] Woosung Choi, Heon Cheol Shin, Ji Man Kim, Jae Young Choi, and Won Sub Yoon. Modeling and applications of electrochemical impedance spectroscopy (Eis) for lithium-ion batteries. *Journal of Electrochemical Science and Technology*, 11(1): 1–13, 2 2020. doi: 10.33961/jecst.2019.00528.
- [67] Jun Huang. Diffusion impedance of electroactive materials, electrolytic solutions and porous electrodes: Warburg impedance and beyond. *Electrochimica Acta*, 281: 170–188, 8 2018. doi: 10.1016/j.electacta.2018.05.136.
- [68] Hui Chia Yu, Stuart B. Adler, Scott A. Barnett, and K. Thornton. Simulation of the diffusional impedance and application to the characterization of electrodes with complex microstructures. *Electrochimica Acta*, 354, 9 2020. doi: 10.1016/j.electacta.2020.136534.
- [69] Samuel Cruz-Manzo and Paul Greenwood. Frequency Transition from Diffusion to Capacitive Response in the Blocked-Diffusion Warburg Impedance for EIS Analysis in Modern Batteries. *Journal of The Electrochemical Society*, 167(14):140507, 10 2020. doi: 10.1149/1945-7111/abbfdc.

- [70] Metrohm Autolab. Application Area: Fundamental Calculation of Cell Constants using the Autolab Microcell HC TSC70 and TSC1600. Technical report, Metrohm Autolab Electrochemistry, 2020. URL www.metrohm.com/en/products/electrochemistry.
- [71] J-Hjelen. Scanning electron microscopy. Available at: <https://www.nb.no/nbsok/nb/4103cf534b134a2f8edceb208f901e0d?lang=no#0>, 1989. Accessed: 02.04.2022.
- [72] ThermoFisher Scientific. Scanning electron microscopy. Available at: <https://www.thermofisher.com/no/en/home/materials-science/learning-center/applications/sem-electrons.html>, 2020. Accessed: 05.04.2022.
- [73] D Dollimore, P Spooner, and A Turner. Review Paper: The BET method of analysis of gas adsorption data and its relevance to the calculation of the surface area. Technical report, Elsevier Sequoia, 1976.
- [74] ATA Scientific instruments. Basic principles of particle size analysis. Available at: <https://www.atascientific.com.au/basic-principles-of-particle-size-analysis/>, 2019. Accessed: 21.03.2021.
- [75] Yang Yang, Lijuan Wang, Ole Wendroth, Baoyuan Liu, Congcong Cheng, Tingting Huang, and Yangzi Shi. Is the Laser Diffraction Method Reliable for Soil Particle Size Distribution Analysis? *Soil Science Society of America Journal*, 83(2):276–287, 3 2019. doi: 10.2136/sssaj2018.07.0252.
- [76] EL Cell. Consumables. Available at: <https://el-cell.com/products/consumables/>, 2021. Accessed: 21.04.2022.
- [77] GmbH and Dr. B. Huber Co. KGDr. M. Drüschler. Application note determination of the through-plane tortuosity of battery electrodes by eis. Technical report, rhd instruments, 2013. URL www.rhd-instruments.de.
- [78] rhd instruments. Tsc 70 closed. Available at: <https://www.rhd-instruments.de/en/products/cells/tsc-70-closed>, 2022. Accessed: 22.04.2022.
- [79] Metrohm Autolab. Compact potentiostats/galvanostats. Available at: https://www.metrohm.com/en_gb/products/electrochemistry/compact-line.html, 2022. Accessed: 23.04.2022.

- [80] EL Cell. Pat core peek sleeves. Available at: https://el-cell.com/pat-core_peek-sleeves/, 2021. Accessed: 23.04.2022.
- [81] M. Vogt, S. Hidalgo, T. Musch, M. Mallach, T. Lange, and J. Förster. 1.4.3 Concepts for accurate electrical conductivity measurement of liquids in industrial process analytics. In *Fachtagung Sensoren und Messsysteme*, pages 105–112. AMA Service GmbH, 12 2020. doi: 10.5162/sensoren2019/1.4.3.
- [82] Johannes Landesfeind, Martin Ebner, Askin Eldiven, Vanessa Wood, and Hubert A. Gasteiger. Tortuosity of Battery Electrodes: Validation of Impedance-Derived Values and Critical Comparison with 3D Tomography. *Journal of The Electrochemical Society*, 165(3):A469–A476, 2018. doi: 10.1149/2.0231803jes.
- [83] Manju Kumari Thakur Vijay Kumar Thakur and Asokan Pappu. *Hybrid Polymer Composite Materials Applications*, volume Volume 4, Hybrid Polymer Composite Materials Hybrid polymer composite material. Woodhead publishing, 2017.
- [84] Dongsheng Lu, Weishan Li, Xiaoxi Zuo, Zhongzhi Yuan, and Qiming Huang. Study on electrode kinetics of Li⁺ insertion in Li_xMn₂O₄ ($0 \leq x \leq 1$) by electrochemical impedance spectroscopy. *Journal of Physical Chemistry C*, 111(32):12067–12074, 8 2007. doi: 10.1021/jp0732920.
- [85] K. Dokko, M. Mohamedi, Y. Fujita, T. Itoh, M. Nishizawa, M. Umeda, and I. Uchida. Kinetic Characterization of Single Particles of LiCoO₂ by AC Impedance and Potential Step Methods. *Journal of The Electrochemical Society*, 148(5):A422, 2001. doi: 10.1149/1.1359197.
- [86] C. M. Kuo, C. H. Lin, and Y. C. Huang. Plastic deformation mechanism of pure copper at low homologous temperatures. *Materials Science and Engineering A*, 396(1-2):360–368, 4 2005. doi: 10.1016/j.msea.2005.01.052.
- [87] Marrckr. Dimethyl carbonate. Available at: <https://www.sigmaaldrich.com/NO/en/substance/dimethylcarbonate9008616386?attributes=density.default%2C%2C>, 2021. Accessed: 20.05.2022.
- [88] PubCchem. Ethylene carbonate. Available at: <https://pubchem.ncbi.nlm.nih.gov/compound/Ethylene-carbonate>, 2021. Accessed: 20.05.2022.

-
- [89] Marrckr. Tetrabutylammonium hexafluorophosphate. Available at: <https://www.sigmaaldrich.com/NO/en/product/aldrich/281026>, 2021. Accessed: 20.05.2022.
- [90] Britannica. Carbon chemical element. Available at: <https://www.britannica.com/science/carbon-chemical-element>, 2021. Accessed: 05.12.2021.
- [91] Chemical book. Carbon black. Available at: https://www.chemicalbook.com/ProductMSDSDetailCB3109508_EN.htm, 2021. Accessed: 05.12.2021.
- [92] Chemical book. Sodium carboxymethyl cellulose. Available at: https://www.chemicalbook.com/ChemicalProductProperty_EN_CB5209844.htm, 2021. Accessed: 05.12.2021.
- [93] Targray. Anode binders. Available at: <https://www.targray.com/li-ion-battery/anode-materials/binders>, 2021. Accessed: 05.12.2021.

A Acronyms

Table [A.1](#) presents the constants and variables used in the calculations for this project.

Table A.1: Constants and variables used in the calculations.

Symbol	Description	Unit	Value
$\bar{C}_{\text{carbon black}}$	Aimed concentration of carbon black	wt%	2
\bar{C}_{CMC}	Aimed concentration of CMC	wt%	1.5
$\bar{C}_{\text{graphite}}$	Aimed concentration of graphite	wt%	95
\bar{C}_{SBR}	Aimed concentration of SBR	wt%	1.5
$A_{\text{electrode}}$	Area of an electrode	cm ²	-
C_{CMC}	Concentration of CMC- solution	%	-
C_{graphite}	Concentration of graphite in the electrode	%	-
C_{SBR}	Concentration of SBR- solution	%	15
C_{sol}	Concentration of solution	mol/L	-
σ	Conductivity	mS/cm	-
ρ_{DMC}	Density of DMC	g/cm ³	1.07 [87]
ρ_{EC}	Density of EC	g/cm ³	1.32 [88]
ρ_i	Density of a component i	g/cm ³	-
$m_{\text{active graphite}}$	Mass of active graphite on an electrode	mg	-
m_A	Mass of active material	g	-
$m_{\text{carbon black}}$	Mass of carbon black	g	-
m_{CMC}	Mass of CMC-powder	g	-
$m_{\text{CMC-solution}}$	Mass of CMC-solution	g	-
m_i	Mass of component i	g	-
m_{Cu}	Mass of Cu-foil	g	-
m_{water}	Mass of deionized water	g	-
m_{graphite}	Mass of graphite powder	g	-
$m_{\text{electrode}}$	Mass of electrode	g	-
m_{liquid}	Mass of liquid in the slurry	g	-
$m_{\text{SBR-solution}}$	Mass of SBR-solution	g	-
m_{solid}	Mass of solid active materials in the slurry	g	-
$m_{\text{Bu}_4\text{NPF}_6}$	Mass of Bu ₄ NPF ₆	g	387.43 [89]
$M_{\text{Bu}_4\text{NPF}_6}$	Molar mass of Bu ₄ NPF ₆	g/mol	387.43 [89]
$C_{\text{specific cap.}}$	Specific capacity of powder	mAh/g	-
R	Resistance	Ω	-
T_{Cu}	Thickness of Cu-foil	cm	-
$T_{\text{electrode}}$	Thickness of electrode	cm	-
TD	True density	g/cm ³	-
V_i	Volume of a component i	mL	-
$wt\%$	Weight percentage	%	-

B Calculations for experimental procedure

B.1 Slurry production

B.1.1 CMC-solution

The CMC-solution was made by mixing CMC-powder and deionized water. Batches of 50 mL solution was made by assuming a density of 1 g/cm^3 with a target concentration of 1.5 %. The amount needed of each component is given by

$$m_{\text{CMC}} = 50\text{g} \cdot \frac{15\%}{100\%} = 7.5\text{g}$$

$$m_{\text{water}} = 50\text{g} \cdot \frac{85\%}{100\%} = 42.5\text{g}$$

were m_{CMC} and m_{water} is the mass needed of CMC-powder and deionized water respectively.

B.1.2 Calculations of slurry components

Multiple slurries were made during this project in which the amount of active material varied. The amount of active material for each slurry depended on the amount of anode laminates made and the used gap-size. Therefore, in the following, a general explanation is given, in which m_A is used as the variable for active material.

The amount of graphite is given by following equation

$$m_{\text{graphite}}[g] = m_A \cdot \frac{\bar{C}_{\text{graphite}}}{100\%}$$

were $\bar{C}_{\text{graphite}}$ is the aimed wt % of graphite. Similar calculation was used to calculate the amount of carbon black, and is given by

$$m_{\text{carbon black}}[g] = m_A \cdot \frac{\bar{C}_{\text{carbon black}}}{100\%}.$$

were $\bar{C}_{\text{carbon black}}$ is the aimed wt % of carbon black.

The amount of CMC- and SBR- solution needed were based on the aimed wt % of CMC (\bar{C}_{CMC}) and SBR (\bar{C}_{SBR}), and the concentration of the specific CMC-solution (C_{CMC})

and SBR-solution (C_{SBR}) respectively. The calculations are given below.

$$m_{\text{CMC-solution}}[g] = m_A \cdot \frac{\bar{C}_{\text{CMC}}}{C_{\text{CMC}}}$$

$$m_{\text{SBR-solution}}[g] = m_A \cdot \frac{\bar{C}_{\text{SBR}}}{C_{\text{SBR}}}$$

The amount of water added depended on the desired loading, and was calculated based on the solid/ liquid-ratio. This ratio is given by

$$\text{solid/liquid-ratio} = \frac{m_{\text{solid}}[g]}{m_{\text{liquid}}[g]}$$

in which m_{solid} is the mass of solid active materials in the slurry, and m_{liquid} is the mass of liquid in the slurry. This parameters can be calculated based on the following two equations

$$m_{\text{solid}}[g] = m_{\text{graphite}} + m_{\text{carbon black}} + m_{\text{SBR-solution}} \cdot \frac{C_{\text{SBR}}}{100} + m_{\text{CMC-solution}} \cdot \frac{C_{\text{CMC}}}{100}$$

$$m_{\text{liquid}}[g] = m_{\text{water}} + m_{\text{SBR-solution}} \cdot \left(1 - \frac{C_{\text{SBR}}}{100}\right) + m_{\text{CMC-solution}} \cdot \left(1 - \frac{C_{\text{CMC}}}{100}\right)$$

B.2 Loading and C-rates

The loading of an electrode is defined by the amount of active material per area. This is given by Equation [B.1](#).

$$\text{Loading}[mg/cm^2] = \frac{m_{\text{active graphite}}}{A_{\text{electrode}}} \quad (\text{B.1})$$

Here, $A_{\text{electrode}}$ is the surface area of the electrode, and $m_{\text{active graphite}}$ is the mass of active graphite in the electrode. This can be found by

$$m_{\text{active graphite}} = [m_{\text{electrode}} - m_{\text{Cu}}] \cdot \left(\frac{C_{\text{graphite}}}{100}\right) \quad (\text{B.2})$$

in which $m_{\text{electrode}}$ is the mass of the electrode, m_{Cu} is the mass of Cu-foil and C_{graphite} is

the percentage of graphite in the electrode.

Based on the mass of active graphite $m_{\text{active graphite}}$ on the electrode, the C-rate can be calculated. Equation [B.3](#) shows the calculation for 1C. Other C-rates can be found based on the 1C value.

$$1C = m_{\text{active graphite}} \cdot C_{\text{specific cap.}} \quad (\text{B.3})$$

To find the aimed loading needed to obtain a capacity of 2 mAh/cm² for both powders during the slurry optimization, the specific capacities were used. The calculation are shown in Equation [B.4](#)

$$\text{Aimed Loading } [mg/cm^2] = \frac{\text{desired capacity}[mAh/cm^2]}{\text{specific capacity}[mAh/g]} \quad (\text{B.4})$$

B.3 Calendering

All graphite electrodes used in the 3-electrode experiments were calendered to a preferred geometrical density. The total thickness of the electrode including the Cu-foil needed to obtain a specific geometrical density is given by Equation [B.5](#)

$$T_{\text{electrode}} = \frac{\text{loading of the electrode}[g/cm^2]}{\text{geometric density of the electrode}[g/cm^3]} + T_{Cu} \quad (\text{B.5})$$

where T_{Cu} is the thickness of the copper-foil.

B.4 Porosity

The porosity of an electrode was calculated based on the geometrical density of the electrode and the true electrode density as shown in Equation [B.6](#)

$$\text{Porosity } [\%] = \left[1 - \frac{\text{Geometrical density of the electrode } [g/cm^3]}{\text{True electrode density } [g/cm^3]} \right] \cdot 100 \quad (\text{B.6})$$

The geometrical density of electrode is based on the thickness and loading of the electrode as described in Equation [B.5](#), while the true electrode density is based on the density of the slurry as shown in Equation [B.7](#). Here TD is the true density and $wt\%$ is the

exact weight percentage of each component in the slurry. The wt% is unique for each slurry as the exact aimed concentration varies due to unaccuracy during weighting. The theoretical density of each component is presented in Table [B.1](#).

$$\text{True electrode density} = (\text{TD} \cdot \text{wt}\%)_{\text{graphite}} + (\text{TD} \cdot \text{wt}\%)_{\text{carbon black}} + (\text{TD} \cdot \text{wt}\%)_{\text{CMC}} + (\text{TD} \cdot \text{wt}\%)_{\text{SBR}} \quad (\text{B.7})$$

Table B.1: The theoretical density of the slurry components.

Component	True density [g/cm ³]
Carbon (s48)	2.24 90
Carbon black (C45)	2.00 91
CMC	1.60 92
SBR	0.98 93

B.5 Electrolyte

The electrolyte was made by mixing ethylene carbonate (EC) and dimethyl carbonate (DMC) in a 1:1 (wt%) ratio. Two solutions were made having a concentration of 0.01 mol/L and 0.1 mol/L of Bu₄NPF₆. The aimed volume of each electrolyte was 6 mL. Based on the density of EC and DMC which are 1.32 g/mL and 1.07 m/mL respectively, a targeted weight equal 3.5g was set for each component. Table [B.2](#) gives an overview of the target and actual mass of EC, DMC and Bu₄NPF₆ for each solution.

Table B.2: The composition of the two electrolytes used for the tortuosity measurements.

Concentration [mol/L]		0.1	0.01
Mass [g]	EC	3.5065	3.5027
	DMC	3.4993	3.5129
Volume [mL]	EC	2.6564	2.6536
	DMC	3.2704	3.2831
	Total	5.9268	5.9366
Mass of Bu ₄ NPF ₆ [g]	Target	0.22960	0.02300
	Actual	0.22987	0.02333

The volume of each compound was calculated based on the mass and density of EC and DMC, according to Equation [B.8](#). The density of EC and DMC is presented in the list of Acronyms in Table [A.1](#).

$$V_i = \frac{m_i}{\rho_i} \quad (\text{B.8})$$

Based on the total volume of EC and DMC, the amount of Bu_4NPF_6 to achieve the two solution of 0.01 mol/L and 0.1 mol/L was calculated based on Equation [B.9](#).

$$m_{\text{Bu}_4\text{NPF}_6} = C_{\text{sol}} \cdot V_{\text{tot}} \cdot M_{\text{Bu}_4\text{NPF}_6} \quad (\text{B.9})$$

C Cycling programs

To obtain a better visual of the different cycling programs used in this work, this section presents detailed explanation of the charge- and discharge- current with corresponding potential limitations. Additionally, for each program the potential as a function of time is presented.

C.1 Determination of the specific capacity

The specific capacity of the S48- and S93- powder was found by cycling coin cells with charge- and discharge- rate equal $C/30$. The cells had graphite and lithium metal as the working- and counter- electrode respectively. Figure C.1 shows the cell potential vs. Li/Li^+ as a function of time for this cycling program. Table C.1 presents the cycling program with corresponding potential limitations. Because coin cells were used, the only controllable potential was the cell potential.

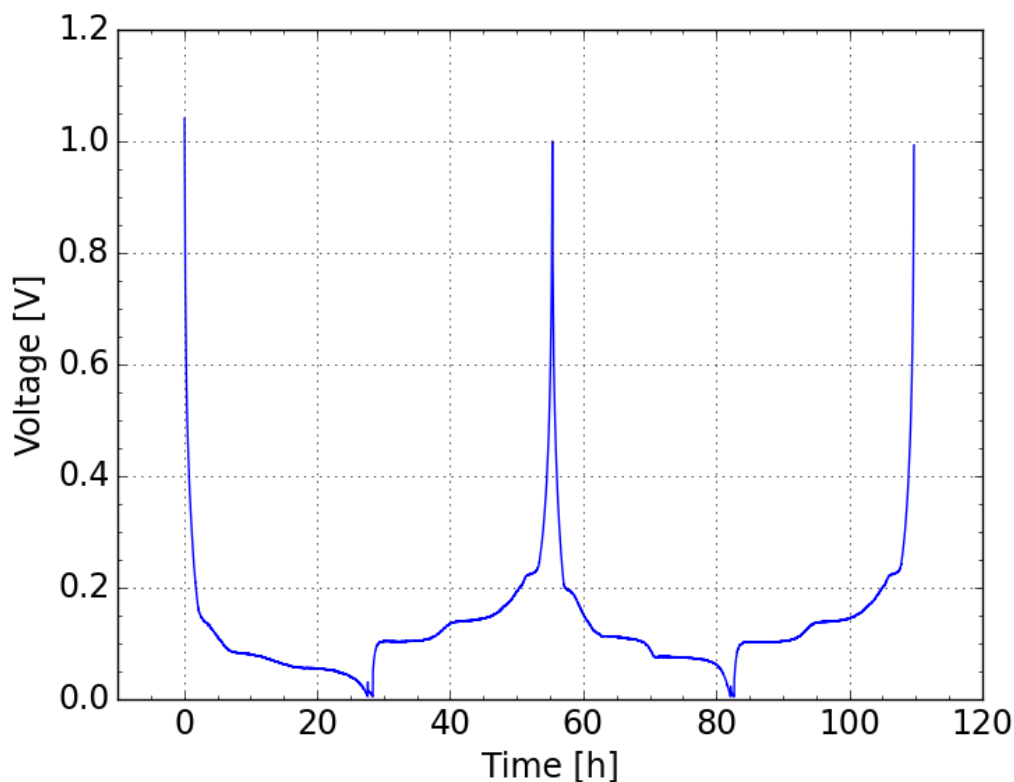


Figure C.1: The cell potential vs. Li/Li^+ as a function of time for determination of the specific capacity of the S49- and S93-powder. Coin cells having graphite and lithium metal as working- and counter- electrode respectively were used for the measurements. The cycling currents were based on the graphite electrode with the theoretical capacity equal 372 mAh/g.

Table C.1: Cycle program for the determination of the specific capacity of the S48- and S93-powder. The C-rates were based on the loading of the graphite electrode.

Number of repetitions	Cycling	Potential imitations
	Rest: 24 hours	
2	Lithiation at $\frac{C}{30}$ Constant voltage down to $\frac{C}{50}$ Delithiation at $\frac{C}{30}$	$E_{cell} \leq 5\text{mV}$. $E_{cell} \geq 1\text{V}$.

C.2 Formation of 3-electrode cells

A visual of the formation program for 3-electrode cells is shown in Figure C.2. Here the cell potential, as well as the potential vs. Li/Li^+ of the working- and counter-electrode are plotted as a function of time. These data was obtained from the S93-cell.

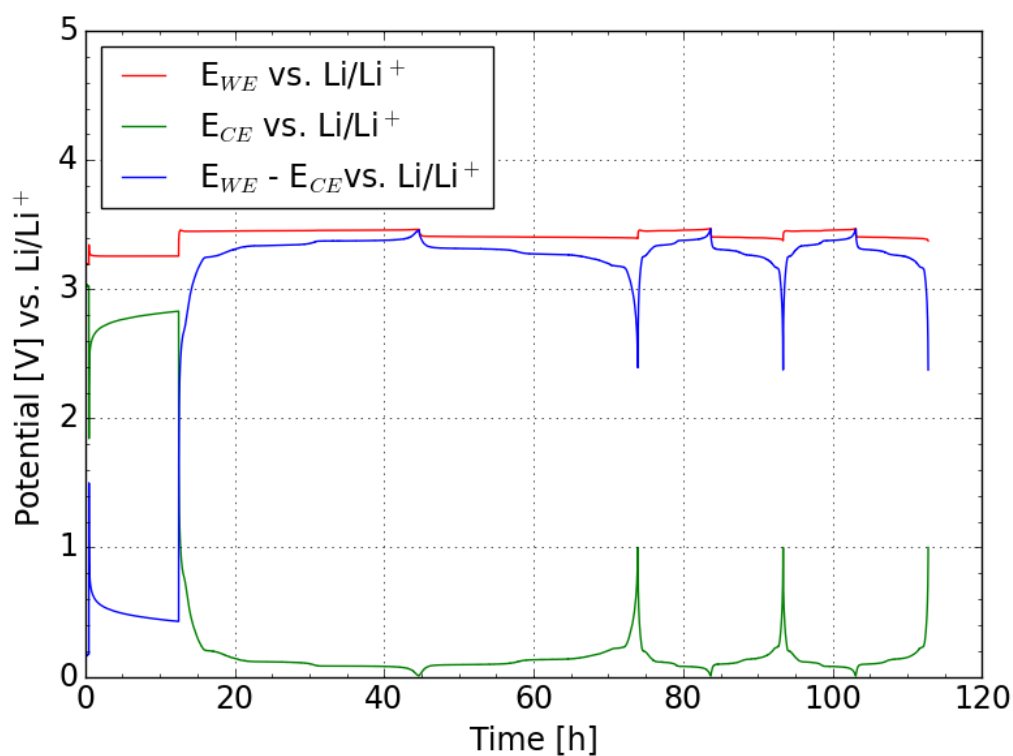


Figure C.2: The cell potential, as well as the potential of the working- and counter- electrode vs. Li/Li^+ as a function of time during formation of 3-electrode cell. The cycling current were based on the graphite electrode using the specific capacity of the powder.

Table C.2 presents the program used for formation of 3-electrode cell. Here, the cycling current with corresponding potential limitation is shown as well as number of repetitions.

Table C.2: Cycle program for formation of 3-electrode cells. The C-rates were based on the loading of the graphite electrode.

Number of repetitions	Cycling	Potential limitations
1	Rest: 30 minutes	
1	Lithiation at $C/20$	$E_{WE}-E_{CE} > 1.500V$ $E_{WE} > 4.000V$ $E_{CE} < 0.005 V$
1	Rest: 12 hours	
1	Lithiation at $\frac{C}{30}$ Delithiation at $\frac{C}{30}$	$E_{WE}-E_{CE} > 4.000V$ $E_{WE} > 4.200V$ $E_{CE} < 0.005 V$ $E_{WE}-E_{CE} > 2.000V$ $E_{WE} > 3.000V$ $E_{CE} < 1.000V$
2	Lithiation at $\frac{C}{10}$ Delithiation at $\frac{C}{30}$	$E_{WE}-E_{CE} > 4.000V$ $E_{WE} > 4.200V$ $E_{CE} < 0.005 V$ $E_{WE}-E_{CE} < 2.000V$ $E_{WE} > 3.000V$ $E_{CE} < 1.000V$

C.3 Charge acceptance test for 3-electrode cell

The cell potential and the potential of the working-, counter- electrode vs. Li/Li^+ as a function of time during the charge acceptance test are shown in Figure C.3. These data is obtained from the S93-cell.

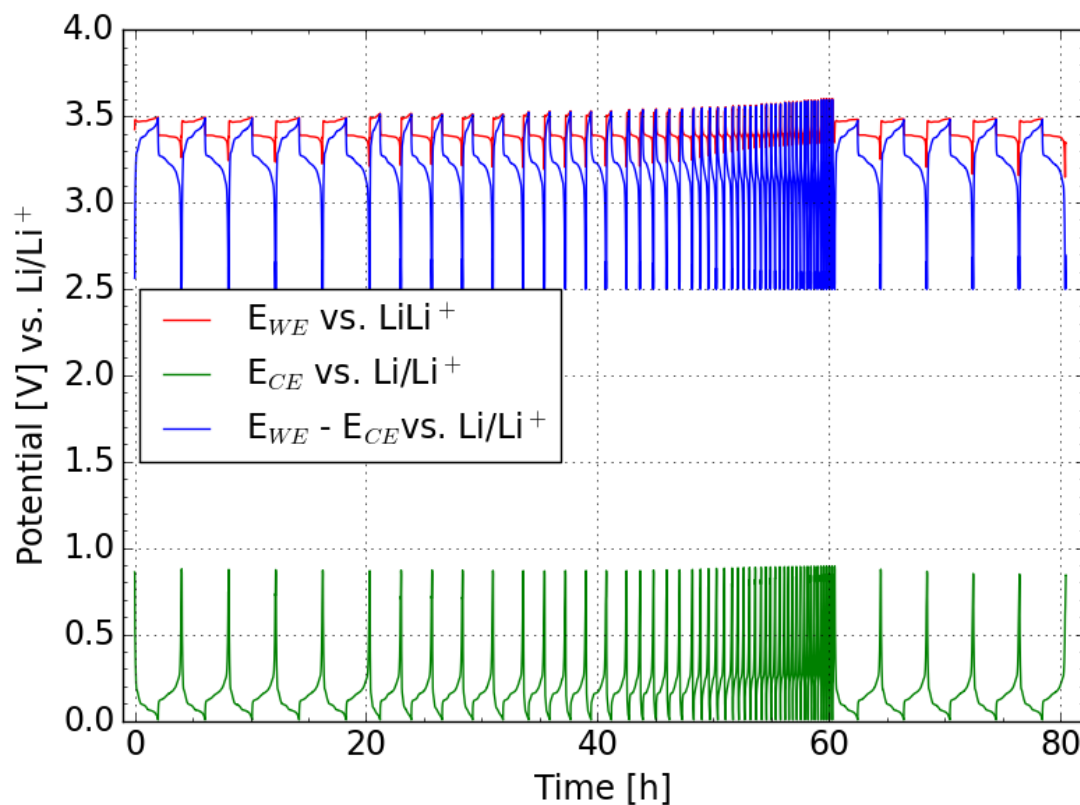


Figure C.3: The cell potential, as well as the potential of the working- and counter- electrode vs. Li/Li^+ as a function of time during the charge acceptance test. The cycling current were based on the graphite electrode using the specific capacity of the powder.

The cycling program used for the charge acceptance test on 3-electrode cells are shown in Table C.3. The table show the charge- and discharge- rats with corresponding potential limitations.

Table C.3: Cycle program for charge acceptance test on 3-electrode cells. The C-rates are based on the specific loading of the graphite electrode. The C-rates were based on the loading of the graphite electrode.

Number of repetitions	Cycling program	Potential limitations
5	Rest: 1 minutes Lithiation at $\frac{C}{2}$ Delithiation at $\frac{C}{2}$ Rest: 1 minute Delithiation at $\frac{C}{10}$	$E_{CE} < 0.005V$ or $E_{WE}-E_{CE} > 4.000 V$ $E_{CE} > 1.000 V$ or $E_{WE}-E_{CE} < 2.500 V$ $E_{CE} > 1.000 V$ or $E_{WE}-E_{CE} < 2.500 V$
5	Rest: 1 minutes Lithiation at 1C Delithiation at $\frac{C}{2}$ Rest: 1 minute Delithiation at $\frac{C}{10}$	$E_{CE} < 0.005V$ or $E_{WE}-E_{CE} > 4.000 V$ $E_{CE} > 1.000 V$ or $E_{WE}-E_{CE} < 2.500 V$ $E_{CE} > 1.000 V$ or $E_{WE}-E_{CE} < 2.500 V$
5	Rest: 1 minutes Lithiation at $\frac{3C}{2}$ Delithiation at $\frac{C}{2}$ Rest: 1 minute Delithiation at $\frac{C}{10}$	$E_{CE} < 0.005V$ or $E_{WE}-E_{CE} > 4.000 V$ $E_{CE} > 1.000 V$ or $E_{WE}-E_{CE} < 2.500 V$ $E_{CE} > 1.000 V$ or $E_{WE}-E_{CE} < 2.500 V$
5	Rest: 1 minutes Lithiation at 2C Delithiation at $\frac{C}{2}$ Rest: 1 minute Delithiation at $\frac{C}{10}$	$E_{CE} < 0.005V$ or $E_{WE}-E_{CE} > 4.000 V$ $E_{CE} > 1.000 V$ or $E_{WE}-E_{CE} < 2.500 V$ $E_{CE} > 1.000 V$ or $E_{WE}-E_{CE} < 2.500 V$
5	Rest: 1 minutes Lithiation at $\frac{C}{2}$ Delithiation at $\frac{C}{2}$ Rest: 1 minute Delithiation at $\frac{5C}{2}$	$E_{CE} < 0.005V$ or $E_{WE}-E_{CE} > 4.000 V$ $E_{CE} > 1.000 V$ or $E_{WE}-E_{CE} < 2.500 V$ $E_{CE} > 1.000 V$ or $E_{WE}-E_{CE} < 2.500 V$
5	Rest: 1 minutes Lithiation at 3C Delithiation at $\frac{C}{2}$ Rest: 1 minute Delithiation at $\frac{C}{10}$	$E_{CE} < 0.005V$ or $E_{WE}-E_{CE} > 4.000 V$ $E_{CE} > 1.000 V$ or $E_{WE}-E_{CE} < 2.500 V$ $E_{CE} > 1.000 V$ or $E_{WE}-E_{CE} < 2.500 V$
5	Rest: 1 minutes Lithiation at 3.5C Delithiation at $\frac{C}{2}$ Rest: 1 minute Delithiation at $\frac{C}{10}$	$E_{CE} < 0.005V$ or $E_{WE}-E_{CE} > 4.000 V$ $E_{CE} > 1.000 V$ or $E_{WE}-E_{CE} < 2.500 V$ $E_{CE} > 1.000 V$ or $E_{WE}-E_{CE} < 2.500 V$
5	Rest: 1 minutes Lithiation at $\frac{C}{2}$ Delithiation at 4C Rest: 1 minute Delithiation at $\frac{C}{10}$	$E_{CE} < 0.005V$ or $E_{WE}-E_{CE} > 4.000 V$ $E_{CE} > 1.000 V$ or $E_{WE}-E_{CE} < 2.500 V$ $E_{CE} > 1.000 V$ or $E_{WE}-E_{CE} < 2.500 V$
5	Rest: 1 minutes Lithiation at 4.5C Delithiation at $\frac{C}{2}$ Rest: 1 minute Delithiation at $\frac{C}{10}$	$E_{CE} < 0.005V$ or $E_{WE}-E_{CE} > 4.000 V$ $E_{CE} > 1.000 V$ or $E_{WE}-E_{CE} < 2.500 V$ $E_{CE} > 1.000 V$ or $E_{WE}-E_{CE} < 2.500 V$
5	Rest: Lithiation at 1 minutes Lithiation at 5C Delithiation at $\frac{C}{2}$ Rest: 1 minute Delithiation at $\frac{C}{10}$	$E_{CE} < 0.005V$ or $E_{WE}-E_{CE} > 4.000 V$ $E_{CE} > 1.000 V$ or $E_{WE}-E_{CE} < 2.500 V$ $E_{CE} > 1.000 V$ or $E_{WE}-E_{CE} < 2.500 V$

D Results

This section presents the addition result obtained in this work. Here, the obtainable capacity of the 3-electrode cells are presented, as well as the results from the impedance measurements.

D.1 Obtainable capacity from first formation cycle

The obtainable capacity during formation at C/30 are presented in Figure [D.1](#). The figure shows the discharge capacities for the two cells tested for the S48- and S93-cells, and for the cells having double- and single- layer graphite electrode.

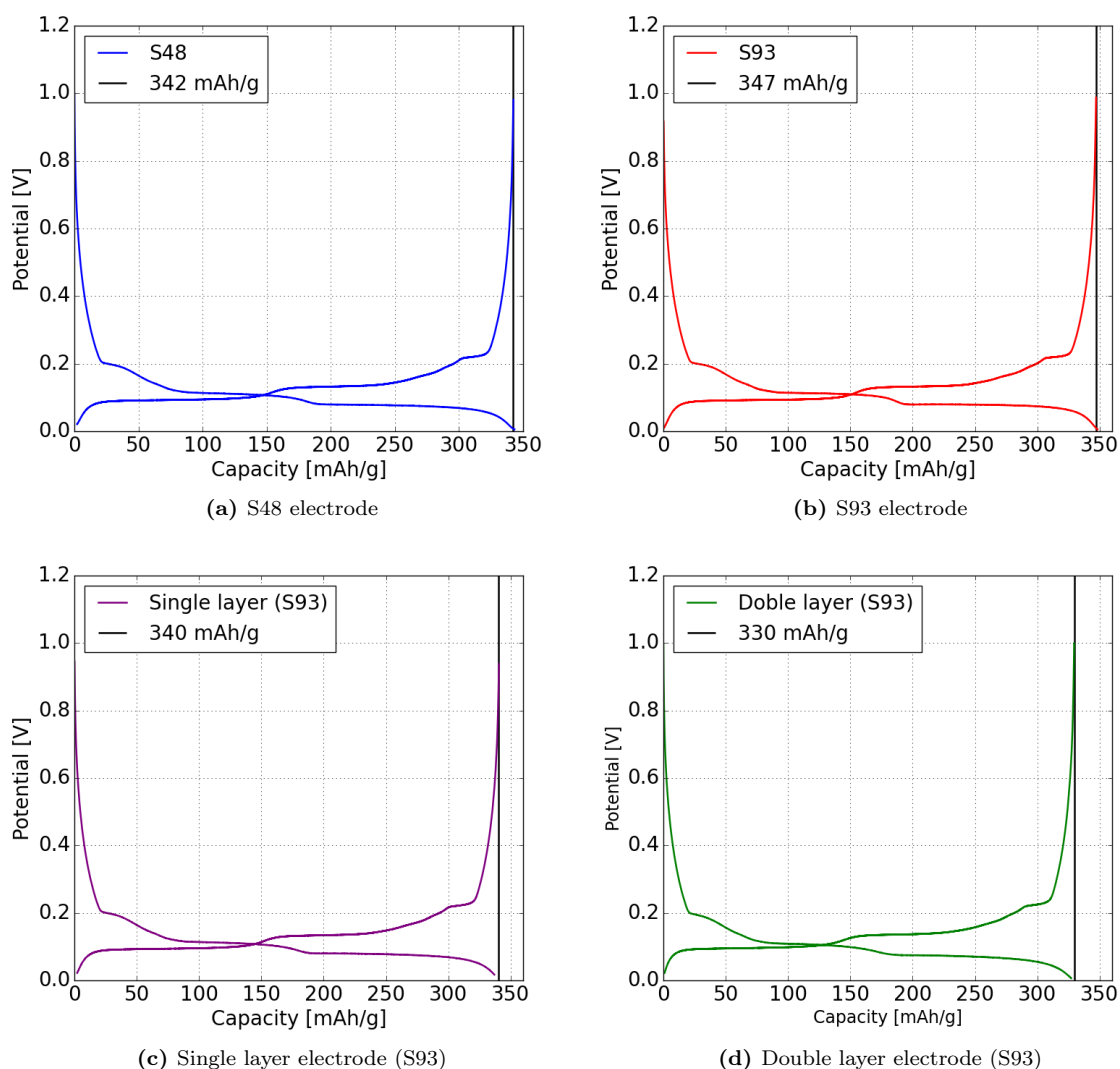


Figure D.1: Potential of the graphite electrode vs. Li/Li^+ as a function of capacity. The figures show the maximum capacity reached at C/30 for the first formation cycle. Figure a and b represents the S48- and S93- cell, while c and d are the single- and double-layer electrodes respectively. The cycling current were based on the graphite electrode using the specific capacity of the powder.

D.2 Ionic conductivity measurements

D.2.1 Cell constant

The cell constant was found by EIS -measurements of a 0.1M KCl-solution. The Nyquist plot from this measurement is shown in Figure [D.3](#).

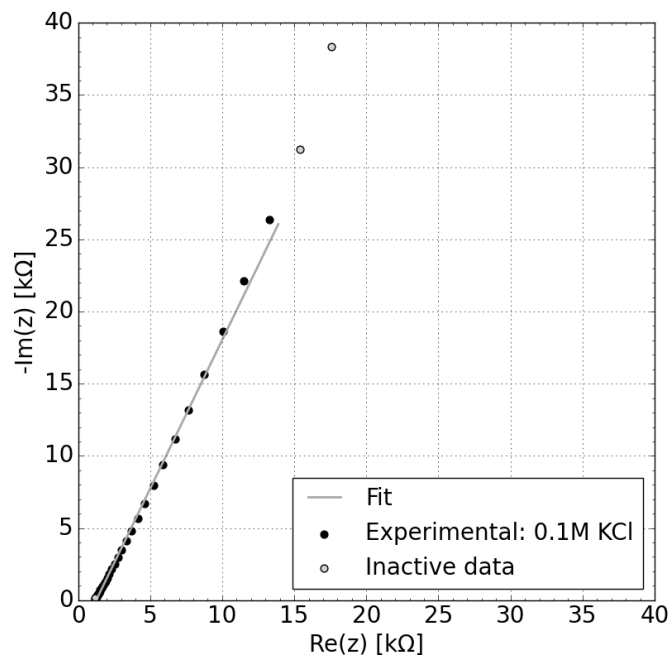


Figure D.3: Nyquist plot for a 0.1M KCl-solution.

By using RelaxIS, the experimental parameters were fitted to the circuit shown in Figure [3.4](#). The parameters with corresponding fitted value are presented in Table [D.1](#).

Table D.1: Parameters for 0.1M KCl-solution. The parameters are fitted to the circuit shown in Figure [3.4](#). RelaxIS were used to evaluate the impedance data.

Parameters	Values
R	$1260.4 \pm 18.3 \Omega$
Q	$2.500 \cdot 10^{-7} \pm 3.600 \cdot 10^{-9} F s^{\alpha-1}$
α	0.713 ± 0.002

Based on the resistance (R) and the known conductivity equal 12.87 mS/cm at 25 °C, the cell constant was found to be $16.22 \pm 0.24 \text{ cm}^{-1}$. The calculation is shown in Equation

D.1

$$K_{\text{cell}} = \sigma \cdot R = 12.87 \cdot 10^{-3} \text{S/cm} \cdot 1260.4 \Omega = 16.22 \text{cm}^{-1} \quad (\text{D.1})$$

D.2.2 Conductivity of electrolytes

The experimental data obtained from EIS-measurements for the two electrolytes were fitted to the circuit shown in Figure 3.4 by using RelaxIS. The resulting values are presented in Table D.2

Table D.2: The parameters for the circuit shown in Figure 3.4 with corresponding fitted value and standard deviation. RelaxIS was used to evaluate the experimental data. The results was obtained from the two electrolytes used in the tortuosity measurements.

Electrolyte concentration	Parameters	Values
0.01 M	R	$42013 \pm 168 \Omega$
	Q	$1.162 \cdot 10^{-8} \pm 3.11 \cdot 10^{-10} F s^{\alpha-1}$
	α	0.797 ± 0.003
0.1 M	R	$5460.2 \pm 13.8 \Omega$
	Q	$1.656 \cdot 10^{-8} \pm 2.26 \cdot 10^{-10} F s^{\alpha-1}$
	α	0.928 ± 0.001

D.2.3 Ionic resistance

The ionic resistance was found by evaluating the EIS-results from the symmetrical cell using the simplified transmission line model. Biologic was used to evaluate the experimental data. The resulting values are presented in Table D.3.

Table D.3: The parameter for the circuit shown in Figure 2.10 with corresponding fitted values and standard deviations. Biologic was used to evaluate the experimental data. The results were obtained from symmetrical cells.

Powder	$C_{\text{electrolyte}}$ [mol/L]	R_{ion} [Ω]	Q [$F s^{\alpha-1}$]	α [-]
s48	0.01	113.00 ± 0.98	0.00055 ± 0.00001	0.94 ± 0.02
	0.10	16.18 ± 0.93	0.00052 ± 0.00002	0.95 ± 0.02
s93	0.01	69.54 ± 0.99	0.00053 ± 0.00001	0.95 ± 0.02
	0.10	11.14 ± 0.99	0.00067 ± 0.00002	0.94 ± 0.01

D.3 Electrochemical impedance data for S48- and S93- cells

The impedance data for the EIS- measurements performed on the S48- and S93- cell after the charge acceptance test were fitted with RelaxIS. The obtained values for the parameters corresponding to Figure 4.14 are presented in Table D.4. The circuit used for this experiment are shown in Figure 4.7.

Table D.4: The parameter for the circuit shown in Figure 4.7 with corresponding fitted values and standard deviations. RelaxIS was used to evaluate the experimental data. The data is fitted to the experimental values of the S48- and S93- cell.

Powders	Parameters	Impedance
S48	R0	$4.52 \pm 0.05 \Omega$
	R1	$7.39 \pm 0.12 \Omega$
	Q0	$0.0120 \pm 0.0050 F s^{\alpha-1}$
	α_Q	0.405 ± 0.008
	Z_w	$381.04 \pm 25.10 \Omega s^{-1/2}$
	τ_W	$1966.6 \pm 187 \text{ s}$
	α_W	0.744 ± 0.005
S93	R0	$4.48 \pm 0.02 \Omega$
	R1	$5.90 \pm 0.09 \Omega$
	Q0	$0.0132 \pm 0.0008 F s^{\alpha-1}$
	α_Q	0.471 ± 0.009
	Z_w	$734.34 \pm 82.50 \Omega s^{-1/2}$
	τ_W	$2907.1 \pm 378.0 \text{ s}$
	α_W	0.809 ± 0.004

D.4 Electrochemical impedance data for the double- and single-layer electrode cells

The fitted parameters from the impedance measurements before and after the charge acceptance test of the double - and single layered electrodes are presented in Table [D.5](#) and [D.6](#) respectively.

Table D.5: The parameter for the circuit shown in Figure [3.6](#) with corresponding fitted values and standard deviations. RelaxIS was used to evaluate the experimental data. The data is fitted to the experimental values of the double layer electrode from the impedance results before and after the charge acceptance test.

Double layered	Parameters	Impedance
Before	R0	$5.13 \pm 0.04 \Omega$
	R1	$6.56 \pm 0.10 \Omega$
	Q0	$0.0071 \pm 0.0005 F s^{\alpha-1}$
	α_Q	0.57 ± 0.01
	Z_w	$168.06 \pm 3.48 \Omega s^{-1/2}$
	τ_W	$630.0 \pm 16.5 \text{ s}$
	α_W	0.726 ± 0.004
After	R0	$4.91 \pm 0.04 \Omega$
	R1	$6.80 \pm 0.17 \Omega$
	Q0	$0.0129 \pm 0.0060 F s^{\alpha-1}$
	α_Q	0.48 ± 0.02
	Z_w	$493.52 \pm 25.80 \Omega s^{-1/2}$
	τ_W	$1840.7 \pm 99.9 \text{ s}$
	α_W	0.808 ± 0.006

Table D.6: The parameter for the circuit shown in Figure 3.6 with corresponding fitted values and standard deviations. RelaxIS was used to evaluate the experimental data. The data is fitted to the experimental values of the single layer electrode for the impedance results taken before and after three charge acceptance test.

Single layered	Parameters	Impedance
Before	R0	$4.32 \pm 0.03 \Omega$
	R1	$5.93 \pm 0.11 \Omega$
	Q0	$0.0131 \pm 0.00105 F s^{\alpha-1}$
	α_Q	0.45 ± 0.011
	Z_w	$622.75 \pm 55.40 \Omega s^{-1/2}$
	τ_W	$2649.0 \pm 290.0 \text{ s}$
	α_W	0.814 ± 0.005
After	R0	$4.06 \pm 0.02 \Omega$
	R1	$5.79 \pm 0.08 \Omega$
	Q0	$0.0148 \pm 0.0008 F s^{\alpha-1}$
	α_Q	0.439 ± 0.008
	Z_w	$368.59 \pm 7.62 \Omega s^{-1/2}$
	τ_W	$1684.0 \pm 45.0 \text{ s}$
	α_W	0.801 ± 0.004

